Universitat de Girona

VISUALIZATION AND PROCESSING OF DIFFUSION TENSOR MRI

FERRAN PRADOS CARRASCO

Dipòsit legal: GI-459-2012
http://hdl.handle.net/10803/78048

ADVERTIMENT: L'accés als continguts d'aquesta tesi doctoral i la seva utilització ha de respectar els drets de la persona autora. Pot ser utilitzada per a consulta o estudi personal, així com en activitats o materials d'investigació i docència en els termes establerts a l'art. 32 del Text Refós de la Llei de Propietat Intel·lectual (RDL 1/1996). Per altres utilitzacions es requereix l'autorització prèvia i expressa de la persona autora. En qualsevol cas, en la utilització dels seus continguts caldrà indicar de forma clara el nom i cognoms de la persona autora i el títol de la tesi doctoral. No s'autoritza la seva reproducció o altres formes d'explotació efectuades amb finalitats de lucre ni la seva comunicació pública des d'un lloc aliè al servei TDX. Tampoc s'autoritza la presentació del seu contingut en una finestra o marc aliè a TDX (framing). Aquesta reserva de drets afecta tant als continguts de la tesi com als seus resums i índexs.

UNIVERSITAT DE GIRONA

PHD THESIS

Visualization and Processing of Diffusion Tensor MRI

Author:
Ferran PRADOS CARRASCO

2012

Programa de Doctorat en Tecnologia

Advisors:
Dra. Imma BOADA I OLIVERAS
Dr. Miquel FEIXAS I FEIXAS

Memòria presentada per optar al títol de doctor per la Universitat de Girona

Agraïments

Aquesta tesis ha estat el producte de molts anys de feina, i dels comentaris i aportacions de molta gent que m'envolta. En primer lloc, vull agrair als meus directors, Imma Boada i Miquel Feixas, l'excel·lent i incomparable recolzament que m'han donat al llarg de la tesis. En segon lloc, vull donar les gràcies a l'Alberto Prats per la seva dedicació infinita, la seva ajuda i els seus comentaris. Sempre m'ha atès molt bé i m'ha ensenyat moltes coses d'anatomia imprescindibles per portar a bon port aquesta tesis.

També cal esmentar la col·laboració dels companys de despatx, de cafè i de batalla: Anton, Marta, Yago, Mario, Ester, Marc, Olga, Roger..., tots han ajudat, i molt, en la realització d'aquesta tesi. També agrair a molta d'altra gent del Departament d'Informàtica i Matemàtica Aplicada com en Josep Antoni Martín, en Josep Daunis, en Josep Soler, en Jordi Poch i en Mateu Sbert, que en tot moment m'han facilitat la feina i m'han donat suport.

Dono les gràcies a en Joan San per ajudar-me amb les seves excel·lents il·lustracions anatòmiques.

Agrair al doctor Salvador Pedraza, i a tot el seu equip, les dades proporcionades, les interessantíssimes reunions de treball al Parc Tecnològic i la possibilitat de formar part d'un equip interdisciplinar tant engrescador com el seu. Vull fer una menció especial, al doctor Josep Puig per tot el feedback rebut, i a en Gerard Blasco, per la seva predisposició a ajudar-me i proporcionar-me tot tipus de dades per tal de poder fer els càlculs.

Moltes gràcies, a l'Albert Ribas i la Carme Echazarreta, pel seu recolzament moral i per les bones estones passades xerrant sobre la tesis i de moltes altres coses.

Vull agrair a la meva família tot el que m'ha donat i ajudat, no només durant la tesis, sinó també al llarg de la meva vida. Agrair als meus pares el seu constant recolzament i la seva confiança cega en les meves possibilitats. Vull donar les gràcies al meu germà pels seus útils consells i les seves idees brillants de programació, mentre corríem per l'Empordà i no tenia ni oxigen per respirar.

Finalment, de forma molt especial, moltíssimes gràcies a la Mariona, per estar al meu costat, per la paciència, per suportar els bons, i sobretot, els no tant bons moments que hi ha hagut al llarg de la tesis.

Moltes gràcies a tots!!!

Grant Support

This thesis has been funded in part with grant numbers MEC TIN2007-68066-C04-01, MEC TIN2007-67982-C02, TIN2010-21089-C03-01, 2009 SGR 643, FIS PI060745 of I+D+I 2006-2009 and FIS PS09/00596 of I+D+I 2009-2012.

Resum

La imatge amb tensor de difusió (DTI) és una nova modalitat de ressonància magnètica (RM) capaç de generar mapes del desplaçament a nivell microscòpic de l'aigua a dins del teixits del cervell com a part del procés físic de la difusió. Aquesta tècnica ha esdevingut una important eina en la investigació de les estructures i funcions cerebrals perquè ens permet tenir dades in vivo de l'orientació de les fibres de matèria blanca. Per aplicar el DTI en la pràctica clínica cal extreure i representar la informació de forma entenedora aplicant tècniques i processos de visualització especialitzats. La informació capturada per la màquina de RM pot ser reduïda a un tensor simètric positiu de segon ordre, que pot ser descomposat en valors i vectors propis. Per una banda tenim, les tècniques de visualització unidimensionals (1D) que redueixen la informació del tensor a un valor escalar que es representa en una imatge en escala de grisos o de colors. Actualment aquesta estratègia és la més utilitzada en la pràctica clínica, ja que les imatges en escala de grisos o de colors són molt fàcils d'interpretar. Per un altra costat tenim, les tècniques de visualització tridimensionals (3D) que redueixen la informació del tensor a un camp vectorial, tenint en compte com la principal direcció de difusió la direcció donada pel vector propi principal. Llavors, es poden utilitzar tècniques de tractografia per tal de trobar patrons de continuïtat dins del camp vectorial, a partir de fer el seguiment pas a pas del camí seguit per un conjunt de partícules que es deixen en el camp vectorial. D'aquesta forma és com s'obtenen els mapes de fibres de matèria blanca.

Donada la importància de les tècniques de visualització 1D i 3D en un context mèdic, el nostre propòsit és estudiar com es poden millorar aquestes tècniques. En primer lloc, analitzarem i introduirem un nou índex d'anisotropia per millorar la interpretació de les dades de DTI. En segon lloc, proposarem una nova tècnica de tractografia, basada en teoria de la informació, per obtenir mapes de fibres de matèria blanca. En tercer lloc, proposarem un nou mètode per automatitzar i optimitzar el procés de determinació de llavors necessari per les tècniques de tractografia per tal que generin grups de fibres que millorin la interpretació dels mapes de fibres de matèria blanca. Finalment, presentarem el DTIWeb que és el programari desenvolupat en el marc d'aquesta tesis per tal d'integrar totes les tècniques proposades. Volem remarcar que el nostre treball ha estat fet amb una estreta col·laboració amb un equip de metges, ja que el principal objectiu d'aquesta tesis és l'aplicació de les nostres contribucions en un entorn mèdic real.

Abstract

Diffusion Tensor Imaging (DTI) is a new magnetic resonance (MR) imaging modality capable of producing quantitative maps of microscopic natural displacements of water molecules that occur in brain tissues as part of the physical diffusion process. This technique has become a powerful tool in the investigation of brain structure and function because it allows for in vivo measurements of white matter fiber orientation. The application of DTI in clinical practice requires specialized processing and visualization techniques to extract and represent acquired information in a comprehensible manner. The information captured by MR devices can be reduced to a second order symmetric positive tensor that can be decomposed in eigenvalues and eigenvectors. On the one hand, one dimensional (1D) visualization techniques reduce the information of the tensor to scalar values that can be represented as a grey or a color scale image. Currently, this strategy is the most used in clinical practice since grey and color coded images are very easy to interpret. On the other hand, three dimensional (3D) visualization techniques reduce the information of the tensor to a vector field by considering the main diffusivity direction given by the principal eigenvector. Then, tracking techniques are used to infer patterns of continuity in the vector field by following in a step-wise mode the path of a set of particles dropped into the field. In this way, white matter fiber maps can be obtained.

Due to the importance of 1D and 3D visualizations techniques in the medical context, our purpose is to study how these techniques can be improved. First, we will explore and introduce new anisotropy indices to interpret DTI data more accurately. Second, we will propose a new tracking technique based on information theory to obtain white matter fiber maps. Third, we will propose a new method to automate and optimize the seeding process required in fiber tracking techniques in order to create clusters of fibers that enhance the interpretation of white matter maps. Finally, we will present DTIWeb, which is a software platform developed in the scope of the thesis to integrate all the proposed techniques. We want to remark that our work has been done in close collaboration with a medical team, since a main objective of this thesis is the application of our contributions in a real medical context.

Contents

List of Tables

List of Figures

CHAPTER 1

Introduction

1.1 Motivation

Medical imaging has become a key discipline within medicine. Technological advances, in both computers and scanners, have allowed us to raise challenges until now unimaginable, and to provide new aspects that could never previously be studied in living humans. In this context, Diffusion Tensor Imaging (DTI) [17, 16] has emerged as a widely used technique in the investigation of brain structure and function, since it allows for in vivo measurements of white matter fiber orientation. This technique is a new magnetic resonance (MR) image modality capable of producing quantitative maps of microscopic natural displacements of water molecules that occur in tissues as part of the physical diffusion process. Applied to brain tissues, it provides the information required for generating white matter connectivity maps. Since the advent of DTI, its processing, analysis, and visualization have become main focuses of research in medical imaging and especially in brain studies.

The amount of information obtained with DTI exacerbates the task of effectively communicating information for use in diagnosis. The main challenge is in the development of strategies to extract and visualize information in a comprehensive manner to be used in medical context. Currently, the most popular approach characterizes DTI information representing the local diffuse behavior of water in a voxel by a second order symmetric positive tensor. By diagonalizing this tensor we can obtain eigenvectors and eigenvalues, from which different graphical representations can be obtained. Among them, the most applied techniques are based on one-(1D) and three-(3D) dimensional representations. 1D visualization techniques use eigenvalues and eigenvectors to reduce tensor information to a scalar index that can be represented in a grey or color coded image. Such images are very easy to compute and interpret. 3D visualization techniques generate white matter fiber maps by reproducing the path of imaginary particles dropped into a vectorial field. This vector field is created by considering, for each tensor, the main eigenvector which represent the principal diffusivity direction. This strategy is known as fiber tracking or tractography. Despite the large number of tracking techniques that have been proposed, there are still many aspects that need further development. On the one hand, most of the techniques require user interaction which is a limiting factor in a real medical context since the technique becomes user dependent. On the other hand, the interpretation of generated maps is difficult since fibers are represented individually and not grouped into anatomical structures. In this case, user interaction is again required to tackle the problem.

The motivation behind this work is to go one step further proposing new techniques

that enhance DTI data interpretation. With this aim, we will apply information theory tools to improve DTI data visualization and validation. The information theory [146] is used with success in fields such as physics, computer science and neurology [43]. In particular, it has been proved that information theory provides powerful tools for medical imaging [13]. In this thesis, Shannon entropy and mutual information will be used to capture different interpretation aspects of DTI data. Our work will be done in close collaboration with a medical team to ensure that our proposals can be applied in medical context.

1.2 Objectives

The main goal of this thesis is the development of new visualization and processing techniques for DTI interpretation using information theory tools. To reach this objective we aim to:

1. **Explore and introduce new anisotropy indices to interpret DTI data more accurately**

   In the last decade, several visualization approaches have been proposed to interpret DTI data. The simplest one reduces DTI data to a 1D scalar index and visualizes it as a grey or color coded image. Currently, this approach is the most applied in clinical practice since the obtained images can be easily interpreted and used as a first step towards the identification of normal and pathological brain tissue.

   In this thesis we will study the different indices that have been proposed and we will present a new set of anisotropy measures obtained from the DTI that can better represent some tensor information.

2. **Study tractography techniques and propose new strategies for the streamline-based approach**

   Despite the popularity of 1D visualization techniques, they are only capable of representing part of the tensor information. To overcome this limitation, new techniques able to create white matter connectivity maps have been proposed. These techniques are known as fiber tracking or tractography strategies. Basically, by diagonalizing tensor in every voxel we can decompose DTI data in eigenvalues and eigenvectors. The main diffusion direction, which corresponds to the eigenvector associated with the largest eigenvalue, is taken into account to define a vector field. Then, fibers are obtained by following the paths of particles dropped in this field. The point where the particle is dropped is the seed point. The strategy used to approximate these paths is the main difference between tracking methods.

   In this thesis we will study tracking techniques and we will analyze how entropy can be applied to obtain a new tracking method that will perform all the pro-

cess automatically without user interaction. Automaticity is a feature of special interest in medical context since it enhances reproducibility.

3. **Automate and optimize the seeding process required by fiber tracking techniques**

   The majority of tracking techniques require as an initialization step the definition of seed points where the tracking process will start. To carry out this step, two basic alternatives can be considered: the brute-force approach that places seeds all over the volume, and the region-based approach that places seeds in the regions-of interest (ROIs) determined by the user. The brute-force approach is computationally more expensive than the ROI-based seeding but it guarantees that all tracks are detected. However, the large amount of generated fibers may turn into cluttered images that make the interpretation and extraction of useful information difficult.

   In this thesis, we will propose a new method to automate VOI detection for seeding. This new method will detect without user interaction the main brain structures and will optimize the seeding process required by tractography too.

4. **Propose new clustering techniques for fiber map interpretation**

   The DTI information combined with fiber-tracking techniques allows us to generate connectivity maps that represent the spatial organization of human white matter [123]. Fiber-tracking maps are difficult to interpret, due to the numbers of drawn fibers. The organization of fibers into anatomically meaningful structures instead of individual fibers is a good strategy to enhance the interpretation of the maps.

   In this thesis we will study how information theory tools can be used to define new clustering techniques capable of automatically generating new comprehensible visualizations.

5. **Evaluate most of proposed techniques in a clinical environment**

   An important part of our research will be the evaluation of proposed techniques in a clinical environment. This process will be done in collaboration with the medical doctors in our research group. We will focus our interest on acute stroke patients, and we will evaluate how the proposed techniques could be used in the diagnosis of this pathology. To carry out this process we will integrate all the developed techniques in a common framework denoted DTIWeb. Such a framework will provide all required functionalities for diagnosis from DTI data.

1.3 Thesis Outline

Besides this introductory chapter, this document is organized into the following six chapters.

- Chapter 2. **Background**

  In this chapter, the background on DTI required for the comprehension of the main issues that are going to be analyzed in the scope of the thesis will be introduced. First, the DTI imaging techniques will be briefly reviewed and, then, computation and visualization techniques will be surveyed. To end the chapter, the main information theory tools, that will be used in the thesis, will be described.

- Chapter 3. **Anisotropy measures**

  In this chapter, we describe how our first objective is reached. A new anisotropy measure derived from compositional data distance will be presented. We show how this measure detects white matter more accurately than classical ones and makes its interpretation easier.

- Chapter 4. **Fiber tracking**

  The principles and the state of the art of fiber tracking techniques will be analyzed. A new tracking method based on stochastic and information-theoretic methods will be proposed. In this chapter, our second objective, is reached.

- Chapter 5. **Automatic VOI detection for DTI seeding**

  In this chapter, the third and fourth objectives are reached. An automatic VOI detection approach accompanied with an optimized seeding process that allow us to generate fiber bundles with the minimal user interaction, will be proposed.

- Chapter 6. **Software: DTIWeb**

  The processing and visualization framework developed in the context of this thesis to integrate all evaluated and developed techniques, will be described. In this chapter, we will present the software tool used to reach our last objective.

- Chapter 7. **Conclusions**

  Finally, conclusions of the thesis and future work will be presented. In addition, the publications related with this thesis will be summarized.

Chapter 2

Background

Recently, theoretical and experimental bases of DTI have advanced significantly and the importance of this MRI modality has also grown considerably. DTI describes local water diffusion within tissues from measurements of molecular displacement in several directions with a MR device. Currently, the most common DTI application is in the study of brain white matter anatomy and different neurological pathologies in which an accurate anatomic knowledge of the white matter is needed. Despite the advantages of this technique, there are still many factors that make its application difficult to use in daily clinical practice. The purpose of this chapter is to introduce the background on DTI and the information theory tools required for the comprehension of the main issues that are going to be analyzed in this thesis.

2.1 Introduction

Our brain is composed of approximately 100 billion nerve cells, called neurons. Each neuron communicates with other neurons that form networks among the cells. The specialized networks in the white matter are called fiber tracts. These tracts define a very complex architecture that allows for the communication to and from the grey matter and to and from other areas of the body. Over the years, many different studies have been carried out to describe the anatomy of these brain connections. These are based on fiber dissection and histology of post-mortem brains or invasive studies of primates, amongst others [160, 148, 106, 140, 61]. Classical medical imaging techniques, such as magnetic resonance imaging (MRI) or functional-MRI, have also played a decisive role in these studies, although these techniques are not capable of reproducing tract information and only can provide tissue information.

In the last decade, with the advent of DTI [16, 17], a new era in the study of brain anatomy has started. DTI is an MRI technique capable of capturing the displacements of particles that are subject to Brownian motion within brain tissues. These displacements give us information about the structural organization and orientation of white matter fibers and, through the technique of tractography, the trajectories of cerebral white matter tracts can be obtained.

The anatomical information provided by DTI is oversimplified compared to the underlying neuroanatomy. However, this technique is an important tool to view anatomical structures since it allows in vivo identification of white matter regions, and, should provide new insights into white matter integrity, fiber connectivity, surgical planning, and patient prognosis.

This chapter has been structured as follows. In Section 2.2, the theoretical bases of DTI imaging are reviewed. Section 2.3 presents the different visualization techniques related with DTI data. Section 2.4 describes in a summarized manner the main open problems related to DTI processing and visualization. Section 2.5 introduces information-theoric tools that will be used in the scope of the thesis. Finally, Section 2.6 presents a brief summary.

2.2 Diffusion Tensor Imaging (DTI)

DTI is an MRI technique that can be used to characterize the orientational properties of the diffusion process of water molecules. Molecular diffusion refers to the random translational motion of molecules (Brownian motion) that results from the thermal energy carried by these molecules [100]. The displacement of the molecules varies according to the features of the analyzed environment. Basically, two diffusion movements can be found, isotropic and anisotropic (see Figure 2.1). Isotropic movement corresponds to environments without a concentration gradient, where the probability of displacement of molecules is equal in all directions, and the mean molecular displacement and the flux are zero. The random mobility of these molecules is statistically well described by a Brownian motion. Anisotropic movement corresponds to a

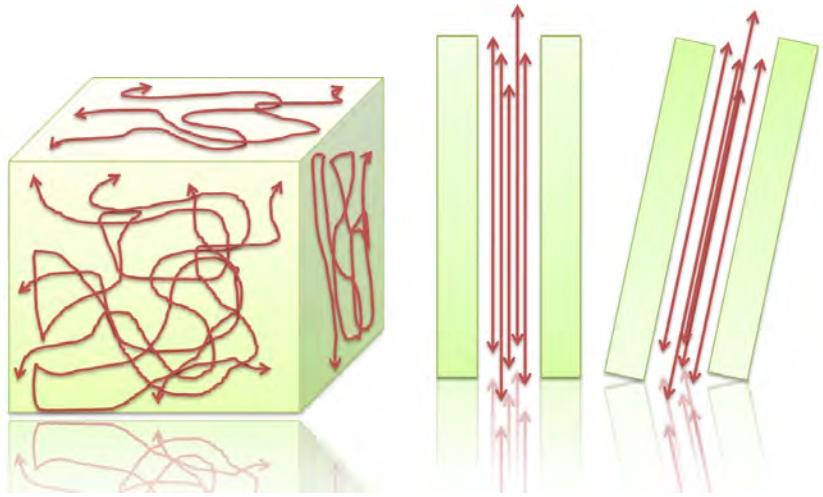

Figure 2.1: Diffusion movements of a molecule in an isotropic environtment (left) and anisotropic one (right).

medium with highly oriented barriers where the tortuosity is different for each direction in the space leading to an anisotropic diffusion. Water molecules located in fiber tracts are more likely to be anisotropic, since they are restricted in their movement as they move more in the dimension parallel to the fiber tract rather than in the two dimensions orthogonal to it, whereas water molecules dispersed in the rest of the brain have less restricted movement and therefore show more isotropy.

The diffusion is a three-dimensional process and the anisotropy is the characteristic of a medium in which physical properties have different values when measured along axes oriented in different directions. To capture diffusion information two main parameters are considered: diffusion anisotropy, which represents the amount of directionality, and orientation of the axis, along which water molecules move preferentially. The diffusion coefficient measured by MRI is also called *apparent diffusion coefficient* (ADC). The diffusion anisotropy might result from the presence of obstacles that limit molecular movement in some directions. ADC depends on the interactions of the diffusing molecules with the cellular structures over a given diffusion time and is not a measure of the *intrinsic* diffusion coefficient.

2.2.1 Acquisition Process

DTI captures information of diffusion in several directions and reduces it to a tensor that describes the local water diffusion at voxel level. To measure diffusion, the Stejskal-Tanner imaging sequence is used [153]. This sequence uses two strong gradient pulses, symmetrically positioned around a 180° refocusing pulse, allowing for controlled diffusion weighting (see Figure 2.2). The first gradient pulse will invert this phase shift, thus canceling the phase shift for static spins. Spins, having completed a change of location due to Brownian motion during the time period (Δ in Figure 2.2),

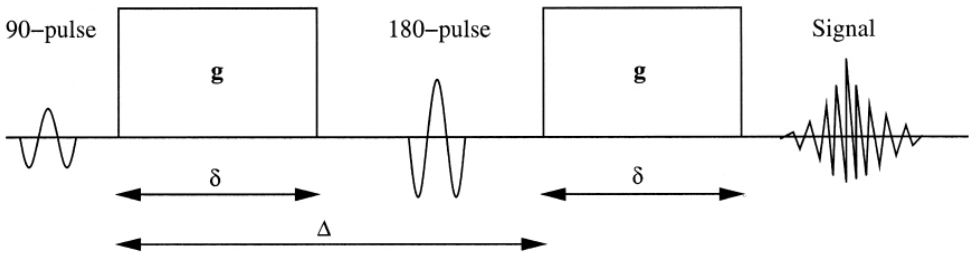

Figure 2.2: The Stejskal-Tanner imaging sequence.

will experience different phase shifts by the two gradient pulses, which means they are not completely refocused and consequently will result in a signal loss.

The dependence of the observed echo signal intensity S on diffusion weighting is given by

$$S = S_0 e^{-bD}, \tag{2.1}$$

where the constant b is the diffusion-weighting factor, S_0 is the signal obtained without diffusion sensitizing gradient (with $b = 0$), and D is the water diffusion constant, also known as the apparent diffusion coefficient (or ADC value, previously introduced), which can be calculated from Equation 2.1 by performing a logarithmic transformation:

$$D = ADC = \frac{\ln(\frac{S_k}{S_0})}{b}. \tag{2.2}$$

For rectangular gradients, the diffusion-weighting factor b is defined by

$$b = \gamma^2 \delta^2 G^2 (\Delta - \frac{\delta}{3}), \tag{2.3}$$

where γ is the gyromagnetic ratio, δ and G the duration and the amplitude of the diffusion sensitizing gradient pulse along a given direction, and Δ is the time interval between the diffusion gradient pulses.

To calculate the diffusion tensor for the case of anisotropic diffusion, Equation 2.1 has to be re-written in a more general form:

$$S = S_0 e^{-bg^t Dg} = S_0 e - b \sum_{i,j=x,y,z} (g_i g_j) D_{ij}, \tag{2.4}$$

where g represents the normalized diffusion sensitizing gradient vector, i.e., $g_k = (g_x, g_y, g_z)^t = \frac{G}{|G|}$, and $\bar{D}$ is a 3x3 diffusion tensor:

$$\bar{D} = \begin{pmatrix} D_{xx} & D_{yx} & D_{zx} \\ D_{xy} & D_{yy} & D_{zy} \\ D_{xz} & D_{yz} & D_{zz} \end{pmatrix}$$

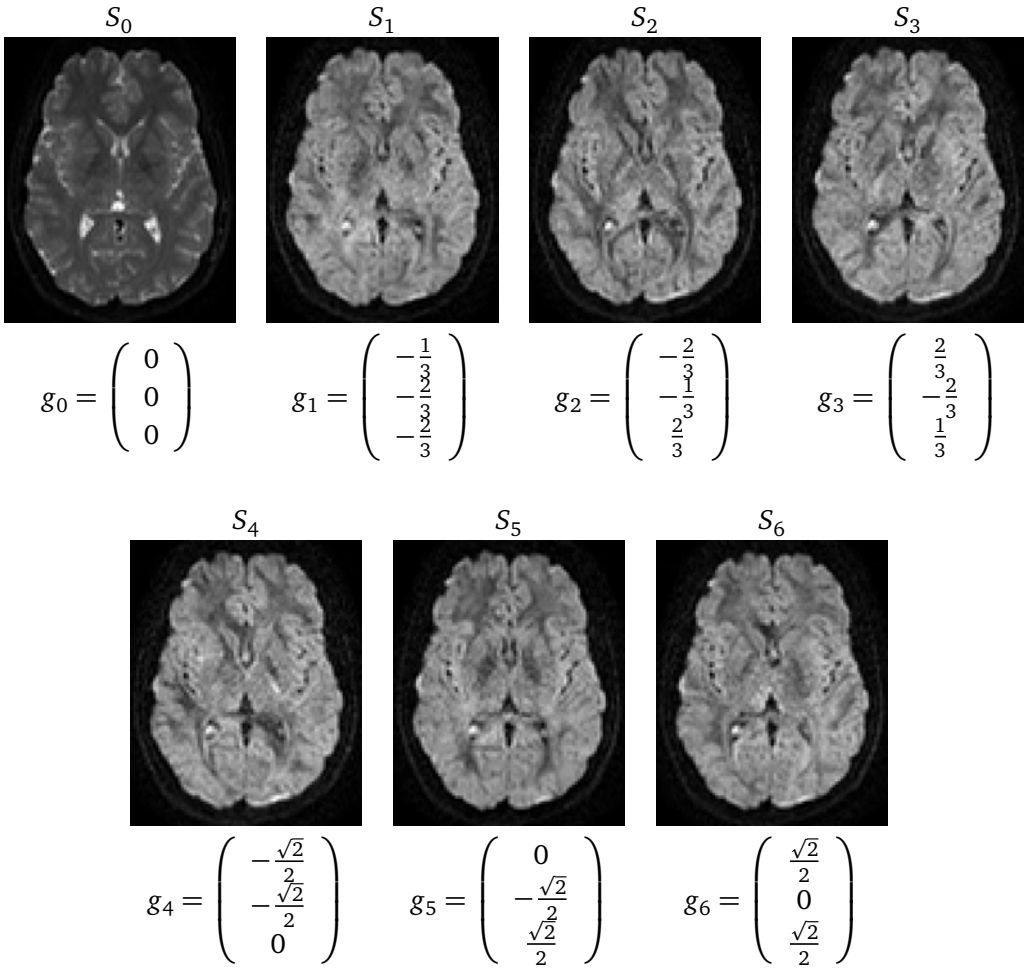

Figure 2.3: Sequence of DTI images $S_0, S_1, ..., S_6$ and its corresponding gradients g_k ($k = 0,...,6$).

that has six degrees of freedom (the number of independent coefficients in a matrix representation). To estimate the tensor, at least six measurements (taken from different non-collinear gradient directions) are needed in addition to the baseline image data S_0. Thus, for each acquisition plane in the data set, seven images need to be collected with different diffusion weighting and gradient directions. Figure 2.3 shows an example of such data with the corresponding gradient directions, where $S_0, S_1, ...S_6$ represent the signal intensities in the presence of gradients g_k ($k = 0,...,6$). S_0 is the signal intensity in the absence of a diffusion-sensitizing field gradient ($|g_0| = 0$), giving the baseline to which the remaining measurements can be related.

Performing the natural logarithm on both sides of the Equation 2.4, re-arranging the terms, and introducing the following two vectors [16]

$$\bar{D} = [D_{xx} \quad D_{yy} \quad D_{zz} \quad D_{xy} \quad D_{yz} \quad D_{yx}]^t \tag{2.5}$$

and

$$\bar{g}_k = [g_x^2 \quad g_y^2 \quad g_z^2 \quad 2g_x g_y \quad 2g_y g_z \quad 2g_y g_x]^t, \tag{2.6}$$

we have

$$\sum_{i,j=x,y,z} D_{ij} = \bar{g}_k^t \cdot \bar{D} = \ln \frac{(S_k/S_0)}{b} = ADC. \tag{2.7}$$

By considering the different gradients g_k ($k = 1,...,K$) and the corresponding acquired signals S_k, we obtain a system of equations from which the tensor can be calculated:

$$\bar{g}_k^t \cdot \bar{D} = \frac{1}{b}(\ln(S_0) - \ln(S_k)) \qquad k = 1...K. \tag{2.8}$$

This system can be rewritten compactly in a matrix form:

$$A \cdot \bar{D} = B, \tag{2.9}$$

where A is a Kx6 matrix

$$A = \begin{pmatrix} \bar{g}_1^t \\ \bar{g}_2^t \\ \vdots \\ \bar{g}_k^t \end{pmatrix} \tag{2.10}$$

$$A = \begin{pmatrix} g_{1x}^2 & g_{1y}^2 & g_{1z}^2 & 2g_{1x}g_{1y} & 2g_{1y}g_{1z} & 2g_{1y}g_{1x} \\ g_{2x}^2 & g_{2y}^2 & g_{2z}^2 & 2g_{2x}g_{2y} & 2g_{2y}g_{2z} & 2g_{2y}g_{2x} \\ \vdots & \vdots & \vdots & \vdots & \vdots & \vdots \\ g_{kx}^2 & g_{ky}^2 & g_{kz}^2 & 2g_{kx}g_{ky} & 2g_{ky}g_{kz} & 2g_{ky}g_{kx} \end{pmatrix} \tag{2.11}$$

and B is a K-dimensional ADC vector

$$B = \begin{pmatrix} ADC_1 & ADC_2 & \cdots & ADC_K \end{pmatrix}^t. \tag{2.12}$$

The matrix A only depends on the diffusion gradient directions, while the vector B is composed of ADC maps derived from each of the diffusion directions. The solution $\bar{D}$ of the equation system is obtained by multiplying the pseudo-inverse of the matrix A, denoted as $A^\dagger$, and vector B:

$$\bar{D} = A^\dagger B = (A^T A)^{-1} A^T B. \tag{2.13}$$

Finally, we obtain the diffusion tensor $\bar{D}$, which is described in each voxel by a positive second-order diagonally symmetric tensor [19]:

$$\bar{D} = \begin{pmatrix} D_{xx} & D_{yx} & D_{zx} \\ D_{xy} & D_{yy} & D_{zy} \\ D_{xz} & D_{yz} & D_{zz} \end{pmatrix}$$

The diagonal elements of $\bar{D}$, (D_{xx}, D_{yy} and D_{zz}), represent the ADC along the x, y and z axes. The off-diagonal elements represent the correlation for the diffusion in perpendicular directions.

2.2.1.1 Diffusion Tensor Eigenvalues and Eigenvectors

By diagonalizing $\bar{D}$ we can determine the main diffusion directions in every voxel. Since second order tensors can be represented by a matrix, they can also be decomposed into eigenvalues and eigenvectors. An eigenvector of the tensor $\bar{D}$ and its corresponding eigenvalue λ have the property that the inner product of the original tensor and the eigenvector results in a vector that is a scalar multiple of the original eigenvector:

$$\bar{D}x = \lambda_i x \qquad x \neq 0. \tag{2.14}$$

The solutions λ_i of Equation 2.14 are the eigenvalues of $\bar{D}$. The vectors $\overrightarrow{e_i}$ associated with each eigenvalue are the eigenvectors of $\bar{D}$. Since the null vector is omitted, Equation 2.14 can be re-written as $(\bar{D} - \lambda_i I)x = 0$, where I represents the identity matrix. This implies that the matrix $\bar{D} - \lambda I$ is singular and its determinant is zero, which corresponds to the eigenvalues being the solutions to the secular equation:

$$|\bar{D} - \lambda_i I| = 0. \tag{2.15}$$

For each eigenvalue λ_i, the corresponding eigenvector $\overrightarrow{e_i}$ can be found by solving

$$(\bar{D} - \lambda_i I)\overrightarrow{e_i} = 0. \tag{2.16}$$

The eigenvector-eigenvalue pairs together represent the information available in the original tensor. The tensor can be written as a weighted sum of the outer products

$$\sum_{i=1}^{3}(\lambda_i \bar{D} = \overrightarrow{e_i}\,\overrightarrow{e_i}^T). \tag{2.17}$$

In general the eigenvalues may be real or complex. However, for a real symmetric tensor, like $\bar{D}$, the eigenvalues are always real and the eigenvectors will be orthogonal to each other.

The diffusion tensor and its eigenvalues may be used to express the degree of diffusion anisotropy present in the tissue of interest. The eigenvector corresponding to the largest eigenvalue will point to the direction of the largest diffusion coefficient and the vector with the smallest eigenvalue points to the smallest diffusion coefficient direction. Eigenvalues and eigenvectors are the base of different DTI visualization strategies (see Section 2.3).

To end this section, in Figure 2.4 we summarize the main steps that lead from the DTI acquisition process to a visual representation. First, the patient is introduced in the MRI device and, according to the defined protocol, images for each defined gradient

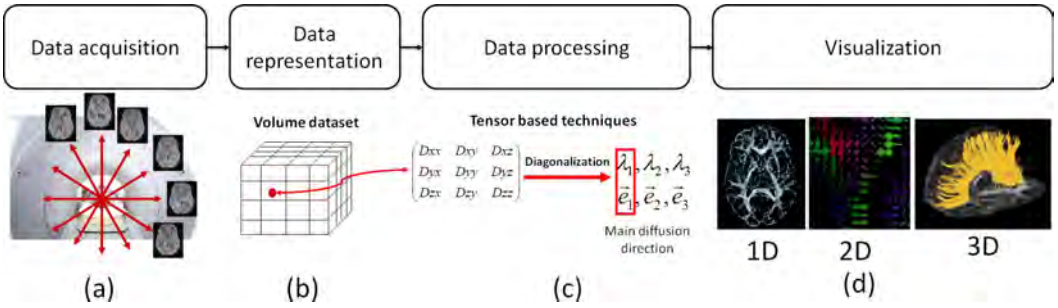

Figure 2.4: Schema of all the steps needed from the acquisition of the DTI data to its visualization. (a) Data acquisition process, (b) representations of the images in a voxel model, (c) data processing to obtain the diffusion tensor, and (d) DTI data visualization.

are generated. These images are stored in a DICOM[1] file composed of a header file with patient and device information, and, raw data with all the images. To process these images, they are generally represented in a voxel model. For each voxel the diffusion tensor, from which eigenvalues and eigenvectors are obtained, can be calculated. To interpret and represent the DTI information, processing and visualization techniques can be applied (see Section 2.3).

2.2.2 Processing DTI Data

DTI data represents information at voxel level. To interpret this data and obtain the white matter fiber distribution, several strategies can be applied [12]. These can be grouped into two main groups (see Figure 2.5). The first one is formed by *tensor-based* approaches which reduce the information acquired by the MRI device to a diffusion tensor as described in the previous section. Eigenvectors and eigenvalues are the main components to be taken into account for computations. The second group is formed by approaches that are based on the *orientation distribution function* (ODF). This covers a variety of methods that reconstruct different functions of the sphere and use them as estimates of the ODF.

We review below the most representative methods of each group.

2.2.2.1 Tensor-Based Processing Techniques

The most representative tensor-based techniques are:

- **Single tensor approach**

  The single tensor approach considers for each voxel, all the diffusion directions needed to calculate the corresponding ADC's [16]. These ADC's are used to

[1] DICOM (Digital Imaging and Communications in Medicine) is a standard for handling, storing, printing, and transmitting information in medical imaging. It includes a file format definition and a network communications protocol.

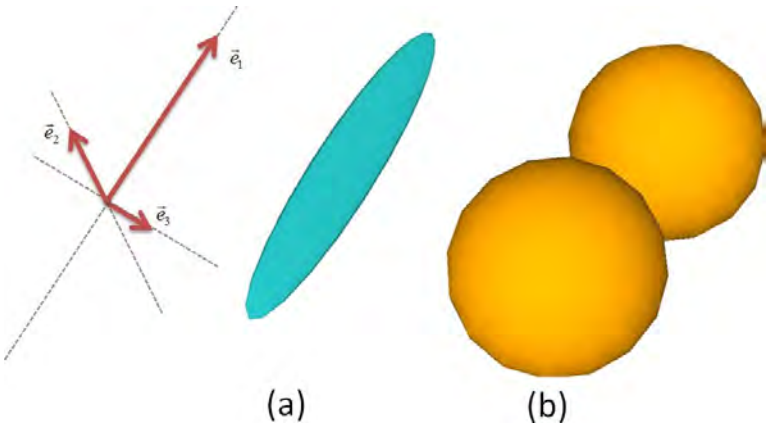

Figure 2.5: Diagram of diffusion tensors. (a) The diffusion tensor is shown as an ellipsoid (an isosurface) with its principal axes along the eigenvectors (e_1,e_2,e_3). (b) The diffusion tensor is shown as an orientation distribution function (ODF).

fit a 3D ellipsoid or a single tensor model into the voxel (see Figure 2.5(a)). The single tensor model reflects the shape of a Gaussian distribution p, since p has approximately ellipsoidal contours, and the principal direction gives a good estimate of the regions where there is only one fiber population, because fibers are aligned along a single axis.

The single tensor approach is the most popular one. A main feature of this technique is that it has a lowest computational cost.

Its main limitation is that it only provides a good estimate of the mean fiber direction, and does not reflect the full complexity of the fibers configuration, which can lead to fiber tract reconstructions vulnerable to severe artifacts.

- **Multi-tensor approach**

  The multi-tensor model [159, 129] is a generalization of the single tensor approach, which replaces the Gaussian model considered in the single tensor with a mixture of n Gaussian densities. The model assumes that the voxel contains n distinct groups or 'populations' of fibers and that diffusing molecules are not exchanged between them, i. e., they stay within a single population. The approach models each population by a separate single tensor. For the multi-tensor analysis, the data of the directional $ADCs$ are fitted to a 2-tensor model.

  The main advantage of the multi-tensor model is its capability to reveal fiber population mixtures that could not be visualized in the original principal eigenvector map [159].

  As a limitation, we have to mention that the multi-tensor model can become unstable when only one population is present and then it produces spurious results.

2.2.2.2 Orientation Distribution Function Processing Techniques

Basically, the ODF quantifies the fraction of fiber portions contained in a voxel, while *tensor-based* approaches only consider a finite number of dominant directions. An ODF may be considered a deformed sphere whose radius in a given direction is proportional to the sum of values of the diffusion probability density function in that direction (see Figure 2.5(b)). Mathematically, the ODF is a probability distribution on the sphere, as each point on the sphere corresponds to a unique orientation. The peaks of the ODF provide estimates of the dominant fiber orientations. The diffusion ODF contains the full angular information of the diffusion probability distribution function (PDF) and is defined as

$$\psi(\theta,\phi) = \int_0^\infty P(r,\theta,\phi)dr, \tag{2.18}$$

where θ and ϕ obey physics convention ($\theta \in [0,\pi]$,$\phi \in [0,2\pi]$).
The most representative ODF techniques are:

- **Diffusion spectrum imaging (*DSI*)**

  DSI [169] measures the microscopic spin displacement function entirely. The DSI is a full 3D Fourier inversion with high radial and high angular measurements of the diffusion PDF.

  The main advantage of DSI is that it can resolve complex intravoxel distributions of fiber orientation including white fiber intersections irresolvable by the tensor model. For example, at intersections of white matter fascicles the DSI exhibits multiple discrete peaks with each peak directed towards a component fiber population.

  The major limitation of DSI is given by the acquisition requirements [168, 12] which is incompatible with clinical applications. To cover the required 3D grid of points in q-space [15] typically requires more measurements than standard DTI acquisition schemes. This fact restricts whole-brain studies. DSI requires very high magnetic gradients to explore this q-space according to [168].

- **Q-Ball imaging (*QBI*)**

  QBI [158] is based on a spherical tomographic inversion called the Funk-Radon transform. QBI is a high angular resolution diffusion imaging (HARDI) technique which has been proven very successful in resolving multiple intravoxel fiber orientations in MR images.

  The main advantages of this technique are its simplicity and its ability to resolve intravoxel fiber orientations. Both have made it popular for fiber tracking and characterizing white matter architecture.

  Although results seem correct in important brain areas, accuracy is not guaranteed in all the regions, and a further validation is required. Another limitation

is that hardware requirements are high. QBI requires approximately 60 samples on the sampling sphere and is less demanding than that of DSI.

- **Spherical deconvolution (*SD*)**

  The key idea of SD [157] is to assume that all white matter fiber bundles in the brain share identical diffusion characteristics. The diffusion-weighted signal attenuation measured over the surface of a sphere can then be expressed as the convolution over the sphere of a response function (the diffusion-weighted attenuation profile for a typical fiber bundle) with the fiber ODF. The fiber ODF within the voxel can therefore be obtained using spherical deconvolution.

  The main advantage is that SD estimates directly the ODF within a voxel from HARDI data without making prior assumptions regarding the number of fiber populations present.

  The main disadvantage is that a major limitation of SD is its susceptibility to noise, which often results in spurious peaks in the recovered fiber ODF. Several regularization techniques have been developed to avoid these peaks [157, 81].

- **Diffusion orientation transform (*DOT*)**

  DOT [126, 127] describes how the diffusivity profiles ADC can be transformed into probability profiles PDF. From this PDF diffusion, the ODF can be obtained by integrating the radial component of the PDF. The key idea is to note that the Fourier transform can be done using the Rayleigh expansion of a plane wave in spherical coordinates.

  The main advantage of DOT is that it is robust and improves the reliability of tractography schemes making the correct identification of neural connections possible.

  DOT makes no assumption about the signal attenuation and has some acquisition requirement that make its daily uses in clinical practice difficult. As in the case of QBI, DOT requires approximately 60 samples on the sampling sphere.

- **Persistent angular structure MRI (*PAS*)**

  The PAS method reconstructs the radially persistent angular structure [74], $\hat{p}$, of the diffusion PDF. Formally, the PAS is the function $\hat{p}$ of the sphere that, when embedded in three-dimensional space on a sphere of radius r, has the Fourier transform that best fits the normalized measurements. PAS is a projection of $\hat{p}$ onto the sphere designed to have a similar structure to the ODF, assuming independence of the angular and radial structure of the diffusion PDF.

  The method is accurate and produces $ODFs$ that look sharper than the QBI estimation of the diffusion ODF.

  Like the DOT, the PAS is a property of $\hat{p}$ rather than the true ODF and the precise relationship is unclear. Non-linear optimization and numerical integration make the PAS algorithm much slower than others. The reconstruction is extremely

heavy computationally and can take several hours/days to reconstruct a full brain dataset of *PAS* functions.

To end this section, in Table 2.1 we summarize the main features of the related strategies [81, 12]. From left to right, in each column we present:

- *Acquisition requirements*, that evaluates the complexity of acquisition process based on the number of different gradient directions needed, and consequently the time required to obtain the input raw DTI data. Acquisition times have been obtained considering a thickness of 3 *mms* and with a 3.0 Tesla MRI device [62]. Methods are classified as *high*, if more than 200 measurements are needed (25-60 minutes), *medium*, if between 200 and 60 required measurements are needed (10-20 minutes), and, finally, *low*, if less than 60 measurements are needed (3-6 minutes).

- *Computation time*, that describes the difference of time required to obtain processed DTI data of a full brain. Methods are classified as: *high*, if hours to days are required, *medium*, if minutes to hours are required, and finally, *low*, if seconds to minutes are required.

- *Accuracy*, that evaluates the good-performance of the processed DTI data. Methods are classified as: *high*, if almost all fiber distribution are well-described, *medium*, if a great number of fiber distribution are detected correctly, and, finally, *low*, if only main fiber distributions are obtained.

- *Interaction*, that measures the level of user interaction needed by the method. Methods are classified as: *high*, if a great number of values and parameters can be selected, *medium*, if some parameters can be changed, and, finally, *low*, if none or few parameters can be tuned.

Method	Acquisition requirement	Computation time	Accuracy	Interaction
Single Tensor [16]	low/medium	low	low/medium	low
Multi-Tensor [159, 129]	low/medium	medium	medium	low
DSI [169, 168]	very high	medium	high	medium
QBI [158]	medium/high	low	medium/low	medium
SD [157]	medium	medium	medium	low
DOT [126, 127]	medium/high	medium	medium	medium
PAS [74]	medium	high	high	low

Table 2.1: Main features of DTI processing techniques.

In this thesis we are going to consider single tensor techniques, taking the diffusion tensor defined at each voxel as the key data to deal with.

2.3 Visualization

Visualization techniques are fundamental for DTI interpretation. They generate images representing DTI processed data. Focusing in tensor-based processing techniques, most of the visualization strategies that have been proposed are based on reducing the dimensionality of the data by extracting relevant information from the diffusion tensor. Following the classification proposed by Vilanova et al. [164], this data can be reduced to 1D, 2D or 3D and hence 1D, 2D and 3D visualization strategies can be considered. In this section, the main approaches that have been proposed for each of these categories are presented.

2.3.1 1D Visualization Techniques

1D visualization techniques generate 2D images from 1D scalar values or indices obtained from tensor within voxels. These scalar values are visualized using a grey or a color scale 2D images. Currently, such an approach is the most used in clinical practice since grey and color coded images are simple and easy to interpret.

The different indices that have been proposed [17, 14, 19] are obtained from diffusion tensor eigenvalues or eigenvectors. The challenge has been the definition of a scalar index representing a meaningful physical quantity, maintaining invariance with respect to rotation and translation, and reducing the effect of noise. Below we present some of the most popular indices that have been proposed:

- *Trace*, that can be seen as the orientational diffusivity and summarizes the total diffusivity [17]:

$$\text{trace} = \lambda_1 + \lambda_2 + \lambda_3. \tag{2.19}$$

- *Mean Diffusivity* ($\langle\lambda\rangle$), that characterizes the overall mean-squared displacement of molecules and the overall presence of obstacles to diffusion [19]:

$$\langle\lambda\rangle = \frac{\text{trace}}{3}. \tag{2.20}$$

- *Fractional Anisotropy* (FA), that measures how far the tensor is from a sphere [19]:

$$FA = \frac{\sqrt{3}}{\sqrt{2}} \frac{\sqrt{(\lambda_1 - \langle\lambda\rangle)^2 + (\lambda_2 - \langle\lambda\rangle)^2 + (\lambda_3 - \langle\lambda\rangle)^2}}{\sqrt{(\lambda_1)^2 + (\lambda_2)^2 + (\lambda_3)^2}}. \tag{2.21}$$

- *Relative Anisotropy* (RA), that measures the ratio of the magnitudes of the anisotropic and isotropic parts of the diffusion tensor [19]:

$$RA = \frac{\sqrt{6}}{6} \frac{\sqrt{(\lambda_1 - \langle\lambda\rangle)^2 + (\lambda_2 - \langle\lambda\rangle)^2 + (\lambda_3 - \langle\lambda\rangle)^2}}{\langle\lambda\rangle}. \tag{2.22}$$

- *Volume Ratio* (VR), that measures the ratio between the ellipsoid volume and the sphere volume, calculated from mean diffusivity [14]:

$$VR = \frac{\lambda_1\lambda_2\lambda_3}{\langle\lambda\rangle^3}. \tag{2.23}$$

In Figure 2.6 visual representations of the indices are shown. RGB images provide more information than grey scale ones, since they use color to represent the directionality of the fibers. In this way, red regions denote left-right fibers, blue regions denote head-feet regions, and green regions, denote anterior-posterior fibers.

A more detailed description of these techniques is given in Chapter 3, where a new set of anisotropy scalar indices will be proposed.

2.3.2 2D Visualization Techniques

The main drawback of 1D visualization techniques is the fact that only one part of DTI data is represented in the image and hence important information is lost. To overcome this limitation, 2D visualization techniques are proposed. These techniques use a graphical representation of eigenvalues (λ_i) and eigenvectors ($\overrightarrow{e_i}$) to express the degree of diffusion anisotropy present in the tissue of interest. This information can be viewed as an ellipsoid [17, 14] (see Figure 2.7), with the length of principal axes described by the tensor eigenvalues and the directions given by the tensor eigenvectors and the length to eigenvalues (see Figure 2.7). Depending on λ values, three basic configurations can be considered [173]:

- *Linear* (or prolate), when the diffusion is only along one direction (i.e., $\lambda_1 >> \lambda_2 \cong \lambda_3$).
- *Planar* (or oblate), when the diffusion is restricted to the plane defined by the two equal eigenvalues (i.e., $\lambda_1 \cong \lambda_2 >> \lambda_3$).
- *Spherical*, when the diffusion is isotropic (i.e., $\lambda_1 \cong \lambda_2 \cong \lambda_3$).

Tensor shapes are described by a combination of linear, planar, and spherical measures, and anisotropic measures are interpreted by considering how much the diffusion ellipsoid deviates from the isotropic case represented as a sphere (Figure 2.8).

Obviously not all configurations can be reduced to one of these three basical configurations. However, there is a continuum of classifications within these extremal cases. To quantify this continuum, Westin [174] introduced three anisotropy coefficients, corresponding to linear diffusion (Cl), planar diffusion (Cp), and spherical diffusion (Cs) cases. These coefficients are obtained as follows:

$$Cl = \frac{\lambda_1 - \lambda_2}{\lambda_1 + \lambda_2 + \lambda_3}, \tag{2.24}$$

$$Cp = \frac{2(\lambda_2 - \lambda_3)}{\lambda_1 + \lambda_2 + \lambda_3}, \text{ and} \tag{2.25}$$

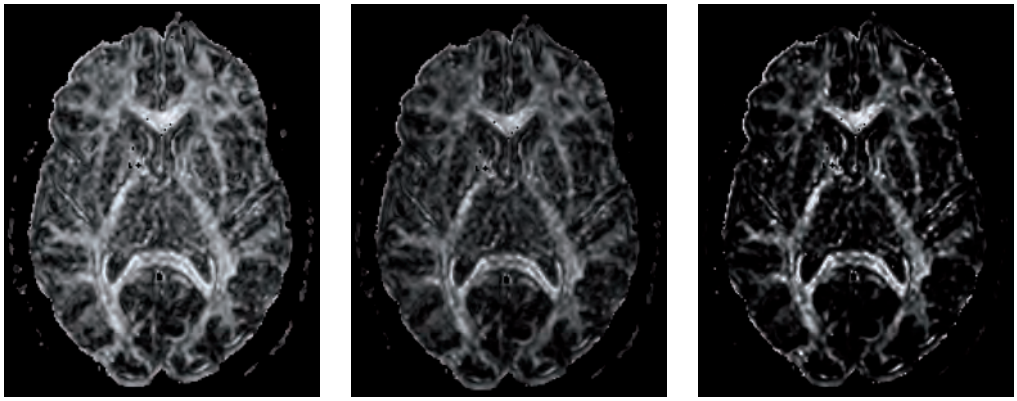

FA *RA* *VR*

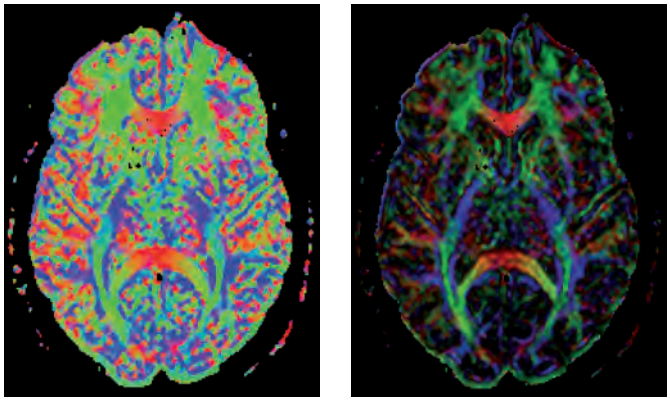

Main Direction *FA weighting Main Direction*

Figure 2.6: Visualization of 1D anisotropy indices. Grey images are obtained by assigning a grey codification to the anisotropy measure. RGB images are obtained by assigning red to regions that denote left-right fibers, blue to regions that denote head-feet regions, and green to regions that denote anterior-posterior fibers.

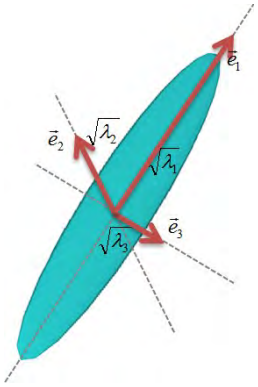

Figure 2.7: Diffusion ellipsoid. The major axes are given by the diffusion tensor eigenvectors.

Figure 2.8: From left to right, graphical representation of linear, planar and spherical diffusion.

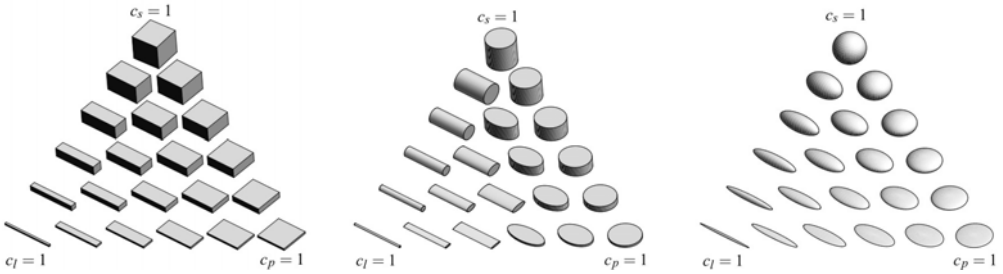

Figure 2.9: Tensor shapes with cuboids, cylinders, and ellipsoids.

$$Cs = \frac{3\lambda_3}{\lambda_1 + \lambda_2 + \lambda_3}. \tag{2.26}$$

The three indices fall in the range [0,1], and by design

$$Cl + Cp + Cs = 1. \tag{2.27}$$

The three metrics Cl, Cp, and Cs parameterize a barycentric space in which the three extremal shape (linear, planar and spherical) are the corners of a triangle, as shown in Figure 2.9. Although ellipsoids are the most common glyphs applied in 2D visualization techniques, there are other glyphs that can be applied as cylinders and cuboids (see Figure 2.9). In Figure 2.10, visualizations of DTI data using the cuboid and ellipsoid glyphing techniques are shown. In this case, glyphs are colored following the RGB 1D map, where RGB values are assigned to the main eigenvector, red regions denote left-right fibers, blue regions denote head-feet regions, and green regions denote anterior-posterior fibers.

The advantage, beside its simplicity is that this approach can be very useful for displaying detailed information in a small local area. The exploration of large areas or volumes is difficult due to glyph overlaps that can generate ambiguities in the interpretation.

More advanced techniques, such as superquadric tensor glyphs [88] or glyph packing [89] overcome these limitations. Superquadric tensor glyphs have the necessary symmetry properties of ellipsoids and, if it is appropriate, also imitating cuboids and cylinders to better convey shape and orientation. Glyph packing uses a particle system with anisotropic potential energy profiles to arrange glyphs into a dense pattern that displays some of the visual continuity of texture-based visualizations, while maintaining the ability to discern the full tensor information at each glyph.

2.3.3 3D Visualization Techniques

1D and 2D visualization techniques only represent a part of the information obtained from DTI. Moreover, they are not capable of reproducing fiber tracts or generate a comprehensive view of the whole brain model. To overcome this limitation, 3D visualization techniques have been proposed. These do not consider the information distributed

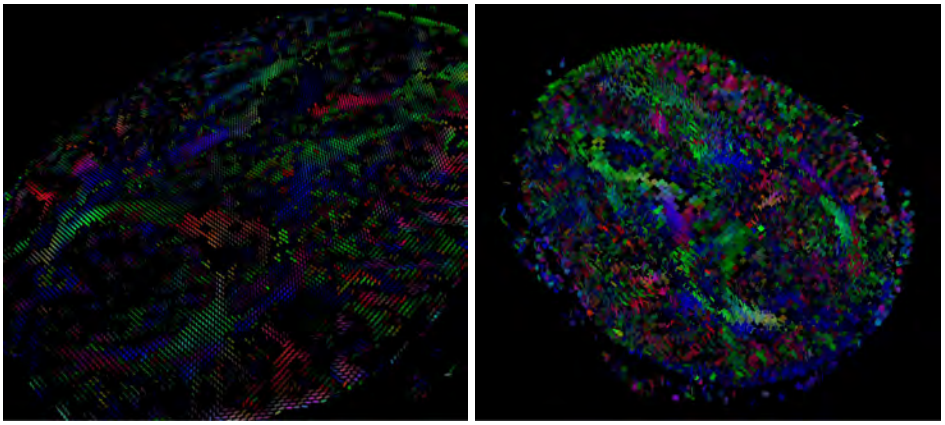

Figure 2.10: DTI 2D visualizations considering cuboids and ellipsoids as glyphs. RGB colors are assigned according to main eigenvector direction.

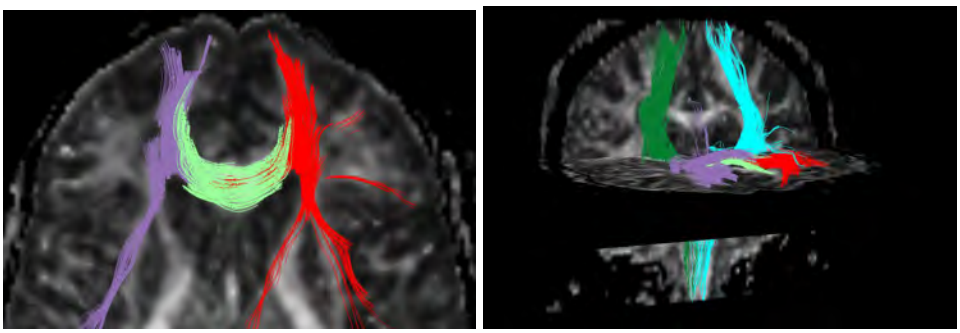

Figure 2.11: Two fiber tracking examples.

onto a single plane, but the information of the 3D model. The basic approaches reduce the tensor data created from the DTI model to a vector field where the vector direction is given by the maximum eigenvector obtained from the tensor (see Section 2.2.1.1). Then, tracking techniques can be applied to generate paths representing fiber tracts and reproduce in this way white matter fiber maps (see Figure 2.11).

Currently, fiber tracking techniques and the development of strategies to improve the interpretation of white matter fiber maps are two important focuses of research and are also analyzed in this thesis.

2.3.3.1 Fiber Tracking Techniques

The most popular fiber tracking technique is the streamline approach [18, 118]. Streamline algorithms assume that the direction of a fiber is collinear with the maximum diffusivity direction given by the main eigenvector of tensor **D**. To create the white matter connectivity map, a set of tracking points or seeds are defined. Then, for each seed, a pathway that follows the maximum diffusivity direction is traced until the boundary

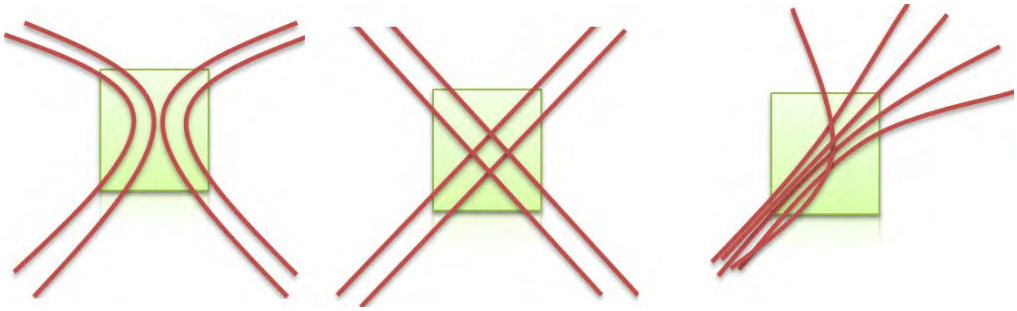

Figure 2.12: Example of different partial volume effects, from left to right: kissing fibers, crossing fibers, and branching fibers.

of the data set is reached or the value of certain measures at the current curve point lies outside a previously specified admissible range of values. Hyperstreamlines are extensions of streamlines that employ all eigenvalues and eigenvectors to represent the fibers [184].

These techniques can be grouped into different categories: deterministic, that follows the major diffusion tensor eigenvector [39, 170, 96, 110], non deterministic, that randomly perturbs the main fiber direction at each location [97, 25, 64, 138], probabilistic, that calculates a spatial probability distribution of connectivity from the seed point [90, 129, 22, 20], and finally, global optimization algorithms, that generate the most optimal path between two brain regions by minimizing a cost function that usually describes the smoothness of the path and the goodness of fit of the path configuration to the underlying diffusion signal [76, 63, 143, 177].

Despite the popularity of fiber tracking techniques, these present several limitations that require further investigation and developments. Next, some of them are described:

- A first limitation of streamline methods arises when the tensor does not have a strong directional component because of image noise [96], partial volume effects [7, 118, 33], or crossing, branching or kissing fiber configurations (see Figure 2.12). In these cases, the direction that the fiber has to follow is not clear. To overcome this limitation, fiber tracking algorithms based on high angular resolution acquisitions [169, 159, 129, 74, 62], regularization [25], tensor deflection [99, 170], and stochasticity [97, 25, 64] have been proposed.

- The seeding process can also be another limiting factor of the approach [36, 35]. In the majority of fiber-tracking algorithms, the user determines where the seeds have to be placed based on anatomical criteria. However, in the case of unhealthy people, part of the anatomical information can be unclear making location of seeds difficult and leading to erroneous trackings or creating maps that represent only a part of the information. To solve this problem, the seeds can be placed over the whole volume. This solution is computationally expensive and generates cluttered images that make the extraction of useful information difficult. Another

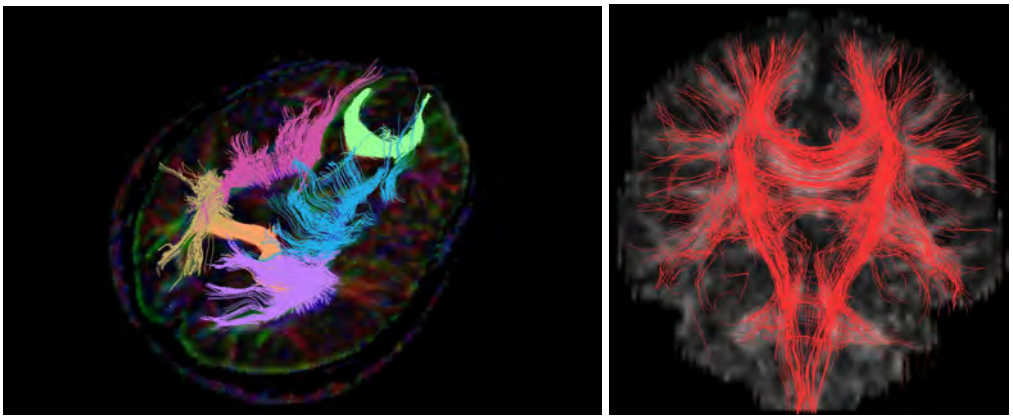

Figure 2.13: Fibers of a human brain created by a fiber tracking algorithm. On the left, fibers of well-known areas grouped by colors, and, on the right, whole brain fiber tracking.

strategy is to place seeds in pre-defined regions of interest. In this case, the reproducibility of the reconstructions is limited due to the high degree of user interaction.

- The interpretation of generated white matter maps is also a difficult task. It is not clear how to correlate obtained data with 3D white matter atlas. In practice, this means that there are no standard methods to determine how fiber information has to be given to experts.

  To enhance fiber maps interpretation, different strategies that group fibers into anatomical bundles have been proposed (see Figure 2.13). At a broad level, these methods can be divided into the three following categories:

  - Interactive segmentation (also known as *virtual dissection* [32]), that groups fiber paths driven by regions of interest defined by the user based on his knowledge [21]. Based on this technique fiber tract atlas [117], several studies in humans [131, 121], and animals [37] have been performed.

    The manual placement of ROIs is a simple but incomplete, time consuming and subjective segmentation technique [85], owing to the complex shapes of most tracts. Complete segmentation by hand is extremely difficult and its reproducibility is limited as has been demonstrated by Clayden et al. [36, 35].

  - Automatic clustering methods, that group fibers, usually obtained from a whole brain fiber tracking, according to a similarity criterion and a clustering algorithm [147, 51, 27, 26, 186, 187]. Some proximity measures are used to establish this relationship between fibers [47, 185, 27, 26, 42]. The proximities are compiled in a proximity matrix, in which rows and columns

correspond to fibers. The proximity matrix is the input to a clustering algorithm [72, 73].

These methods generate different groups of fibers. It is unclear which clustering methods and parameter settings give the best results. In [113] we can find a good evaluation and review of some of the most significant automatic fiber clustering methods for DTI.

– Automatic atlas-based segmentation incorporates brain prior knowledge, obtained from atlas or parcellation maps, to white-matter fiber tracking. Several approaches have been proposed [109, 122, 123, 188, 189, 102].

For this segmentation, we need to build up a white-matter atlas before, and then perform non-linear registration. Other technique is based on termination of the fibers. In this case, we can use a grey matter anatomical labeling to guide the clustering process of white-matter fibers.

2.4 DTI Challenges

DTI processing is a very active area of research involving many scientific fields. Continuous progress is made in order to acquire data with more resolution, to reduce image acquisition time [8, 190], or to reduce noise and distortion effects [105, 119]. Different methods to better reconstruct and interpret DTI data are proposed [12]. DTI medical applications are also enlarged and better diagnosis and treatments can be made thanks to DTI information. However, despite these advances, there are still many different aspects that need further development. In this section we want to review the ones that can influence our results.

2.4.1 Noise

One of the main limitations of DTI is caused by noise and artifacts, which degrade the quality of MR images causing poor estimation of dominant diffusion directions in DTI.

There are different sources of noise. Amongst them, the thermal noise, that arises from the random fluctuation of the currents in the body and the detection system [40, 134]. The thermal noise is an independent source from the MRI signal that also affects DTI measurements. Another noise effect is the eddy current produced by the large and rapidly switched magnetic field gradients during a pulse sequence [77]. Eddy currents have two undesirable effects [84]: first, the field gradient at the sample differs from the prescribed field gradient, and second, a slowly decaying field during readout of the image causes geometrical distortion of the diffusion weighted images.

Recently, a huge number of articles on noise artifacts and denoising methods have been published [40, 77, 9, 66, 96, 67, 56, 33, 84].

2.4.2 Partial Volume Effect

The partial volume effect is the loss of contrast between two adjacent tissues in an image caused by insufficient resolution so that more than one tissue occupies the same

voxel. Since the organization of tissues in the brain is heterogeneous and complex, partial volume effects may significantly influence the accuracy of DTI measurements.

In the voxels, where diffusion is high in more than one direction (i.e., where planar anisotropy is high), the partial volume effect arises. In these areas we are not able to determine correctly the direction of the contained fibers because different fiber patterns can be given. In Figure 2.12, three possible ambiguous cases are illustrated. These voxels have the same tensor **D** but contain different fiber distributions. To solve this problem, several strategies have been proposed [170, 159, 118, 23, 33].

2.4.3 Visualization

The architecture of the brain is composed of millions and millions of fibers. Therefore, their independent visualization is not possible due to the high amount of information available in each sample point. Individual structures are virtually indistinguishable and it is very difficult to extract any useful information. To tackle this problem, researchers look for techniques that not only render data but also provide medical doctors with comprehensive images. Different clustering methods have been proposed to organize the fibers into clusters corresponding to different anatomic areas. These methods are still in a phase of development since the automatic definition of clusters is not trivial [147, 185, 186, 26, 187, 112].

2.4.4 Validation

The last topic we want to mention is related to the validation of DTI processing results. Different to other image modalities, there is not a gold standard to validate with. Validation requires an evaluation carried out by experts, who base their opinions on the knowledge acquired from the atlas generated by dissection processes. The definition of a gold standard to automate this validation process is essential but it is still lacking. Several research groups are working on the definition of such a brain atlas [165, 117, 103, 189].

2.5 Information Theory Tools

In this section, we present some basic concepts of information theory required for the comprehension of the thesis. Very good references are the books by Cover and Thomas [43] and Yeung [182].

2.5.1 Entropy

In 1948, Claude Shannon published "A mathematical theory of communication" [146] which marked the beginning of information theory. In this paper, he defined measures such as entropy and mutual information[2], and introduced the fundamental laws of data compression and transmission.

[2] In Shannon's paper, the mutual information is called rate of transmission.

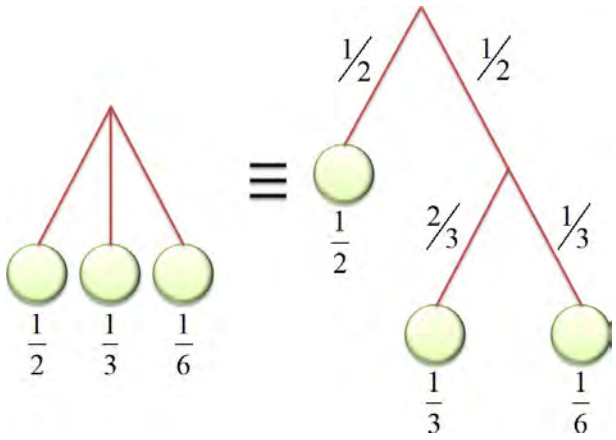

Figure 2.14: Grouping property of the entropy.

Shannon asked himself for a measure to quantify the information produced by an information source. "Suppose we have a *set of possible* events whose *probabilities of occurrence* are p_1, p_2, ..., p_n. These probabilities are known but that is all we know concerning which event will occur. Can we find a measure of how much "choice" is involved in the selection of the event or of how uncertain we are of the outcome?

If there is such a measure, say $H(p_1, p_2, \ldots, p_n)$, it is reasonable to require of it the following properties:

1. H would be continuous in the p_i.

2. If all the p_i are equal, $p_i = \frac{1}{n}$, then H should be a monotonic increasing function of n. With equally likely events there is more choice, or uncertainty, when there are more possible events.

3. If a choice is broken down into two successive choices, the original H should be the weighted sum of the individual values of H. The meaning of this is illustrated in Figure 2.14.

   On the left, we have three possibilities $p_1 = \frac{1}{2}$, $p_2 = \frac{1}{3}$, $p_3 = \frac{1}{6}$. On the right, we first choose between two possibilities each with probability $\frac{1}{2}$, and if the second occurs, we make another choice with probabilities $\frac{2}{3}$, $\frac{1}{3}$. The final results have the same probabilities as before. We require, in this special case, that $H(\frac{1}{2}, \frac{1}{3}, \frac{1}{6}) = H(\frac{1}{2}, \frac{1}{2}) + \frac{1}{2}H(\frac{2}{3}, \frac{1}{3})$. The coefficient $\frac{1}{2}$ is because this second choice only occurs half the time."

After these requirements, he introduced the following *theorem*: "The only H satisfying the three above assumptions is of the form:

$$H = -K \sum_{x \in \mathcal{X}} p(x) \log p(x), \tag{2.28}$$

where K is a positive constant". When $K = 1$ and the logarithm is $\log_2$, information is measured in bits.

Shannon called this quantity *entropy*. The Shannon entropy is the classical measure of *information*, where information is simply *the outcome of a selection among a finite number of possibilities*. Entropy also measures *uncertainty* or *ignorance*.

Thus, the *Shannon entropy* $H(X)$ of a discrete random variable X with values in the set $\mathcal{X} = \{x_1, x_2, \ldots, x_n\}$ is defined as

$$H(X) = -\sum_{x \in \mathcal{X}} p(x) \log p(x), \tag{2.29}$$

where $p(x) = Pr[X = x]$, the logarithms are taken in base 2 (entropy is expressed in bits), and we use the convention that $0 \log 0 = 0$, which is justified by continuity. We can use interchangeably the notation $H(X)$ or $H(p)$ for the entropy, where p is the probability distribution $\{p_1, p_2, \ldots, p_n\}$. As $-\log p(x)$ represents the *information* associated with the result x, the entropy gives us the *average information* or *uncertainty* of a random variable. Information and uncertainty are opposite. Uncertainty is considered before the event, information after. So, information reduces uncertainty. Note that the entropy depends only on the probabilities.

Some other relevant properties [146] of the entropy are

1. $0 \leq H(X) \leq \log n$
   - $H(X) = 0$ if and only if all the probabilities except one are zero, this one having the unit value, i.e., when we are certain of the outcome.
   - $H(X) = \log n$ when all the probabilities are equal. This is the most uncertain situation.
2. If we equalize the probabilities, entropy increases.

When $n = 2$, the *binary* entropy (see Figure 2.15) is given by

$$H(X) = -p \log p - (1 - p) \log(1 - p), \tag{2.30}$$

where the variable X is defined by

$$X = \begin{cases} 1 & \text{with probability } p \\ 0 & \text{with probability } 1 - p. \end{cases}$$

If we consider another random variable Y with probability distribution $p(y)$ corresponding to values in the set $\mathcal{Y} = \{y_1, y_2, \ldots, y_m\}$, the *joint entropy* of X and Y is defined as

$$H(X, Y) = -\sum_{x \in \mathcal{X}} \sum_{y \in \mathcal{Y}} p(x, y) \log p(x, y), \tag{2.31}$$

where $p(x, y) = Pr[X = x, Y = y]$ is the joint probability.

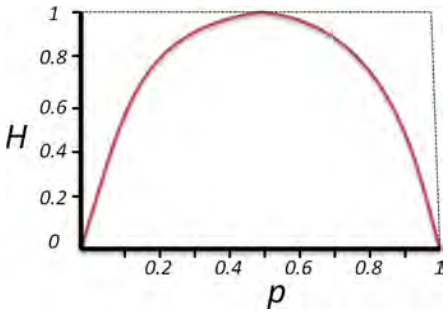

Figure 2.15: Binary entropy.

Also, the *conditional entropy* is defined as

$$H(X|Y) = -\sum_{y\in\mathcal{Y}}\sum_{x\in\mathcal{X}} p(x,y)\log p(x|y), \tag{2.32}$$

where $p(x|y) = Pr[X = x|Y = y]$ is the conditional probability.

The Bayes theorem expresses the relation between the different probabilities:

$$p(x,y) = p(x)p(y|x) = p(y)p(x|y). \tag{2.33}$$

If X and Y are *independent*, then $p(x,y) = p(x)p(y)$.

The conditional entropy can be thought of in terms of a *channel* whose input is the random variable X and whose output is the random variable Y. $H(X|Y)$ corresponds to the uncertainty in the channel input from the receiver's point of view, and vice versa for $H(Y|X)$. Note that in general $H(X|Y) \neq H(Y|X)$.

The following properties are also met:

1. $H(X,Y) \leq H(X) + H(Y)$
2. $H(X,Y) = H(X) + H(Y|X) = H(Y) + H(X|Y)$
3. $H(X) \geq H(X|Y) \geq 0$

2.5.2 Mutual Information

The *mutual information* between two random variables X and Y is defined as

$$\begin{aligned} I(X,Y) &= H(X) - H(X|Y) \\ &= H(Y) - H(Y|X) \\ &= -\sum_{x\in\mathcal{X}} p(x)\log p(x) + \sum_{y\in\mathcal{Y}}\sum_{x\in\mathcal{X}} p(x,y)\log p(x|y) \\ &= \sum_{x\in\mathcal{X}}\sum_{y\in\mathcal{Y}} p(x,y)\log\frac{p(x,y)}{p(x)p(y)}. \end{aligned} \tag{2.34}$$

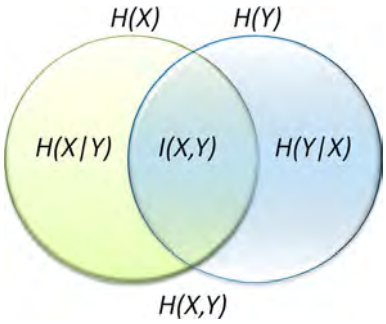

Figure 2.16: Venn diagram of a discrete channel.

Mutual information represents the amount of information that one random variable, the output of the channel, gives (or contains) about a second random variable, the input of the channel, and vice versa, i.e., how much the knowledge of X decreases the uncertainty of Y and vice versa. Therefore, $I(X,Y)$ is a measure of the shared information between X and Y.

Mutual information $I(X,Y)$ has the following properties:

1. $I(X,Y) \geq 0$ with equality if, and only if, X and Y are independent.
2. $I(X,Y) = I(Y,X)$
3. $I(X,Y) = H(X) + H(Y) - H(X,Y)$
4. $I(X,Y) \leq H(X)$

The relationship between all the above measures can be expressed by the Venn diagram, as shown in Figure 2.16.

The *relative entropy* or *Kullback-Leibler distance* between two probability distributions $p(x)$ and $q(x)$, that are defined over the set $\mathcal{X}$, is defined as

$$D_{KL}(p\|q) = \sum_{x\in\mathcal{X}} p(x)\log\frac{p(x)}{q(x)}, \tag{2.35}$$

where, from continuity, we use the convention that $0\log 0 = 0$, $a\log\frac{a}{0} = \infty$ if $a > 0$, and $0\log\frac{0}{0} = 0$.

The relative entropy is "a measure of the inefficiency of assuming that the distribution is q when the true distribution is p" [43].

The relative entropy satisfies the *information inequality* $D_{KL}(p\|q) \geq 0$, with equality only if $p = q$. The relative entropy is also called *discrimination* and it is not strictly a distance, since it is not symmetric and does not satisfy the triangle inequality. Moreover, we have to emphasize that the mutual information can be expressed as

$$I(X,Y) = D_{KL}(\{p(x,y)\}\|\{p(x)p(y)\}). \tag{2.36}$$

2.5.3 Important Inequalities

Some of the above properties can be deduced from the inequalities presented in this section [43]. In addition, these will also play an important role in obtaining fundamental results in this thesis.

2.5.3.1 Jensen's inequality

A function $f(x)$ is *convex* over an interval (a,b) (the graph of the function lies below any chord) if for every $x_1, x_2 \in (a,b)$ and $0 \leq \lambda \leq 1$,

$$f(\lambda x_1 + (1-\lambda)x_2) \leq \lambda f(x_1) + (1-\lambda) f(x_2). \tag{2.37}$$

A function is strictly convex if equality holds only if $\lambda = 0$ or $\lambda = 1$. A function $f(x)$ is *concave* (the graph of the function lies above any chord) if $-f(x)$ is convex.

For instance, $x \log x$ for $x \geq 0$ is a strictly convex function, and $\log x$ for $x \geq 0$ is a strictly concave function [43].

Jensen's inequality: If f is convex on the range of a random variable X, then

$$f(E[X]) \leq E[f(X)], \tag{2.38}$$

where E denotes expectation. Moreover, if $f(x)$ is strictly convex, the equality implies that $X = E[X]$ with probability 1, i.e., X is a deterministic random variable with $Pr[X = x_0] = 1$ for some x_0.

One of the most important consequences of Jensen's inequality is the information inequality $D_{KL}(p\|q) \geq 0$. Other previous properties can also be derived from this inequality.

Observe that if $f(x) = x^2$ (convex function), then $E[X^2] - (E[X])^2 \geq 0$. So, the variance is invariably positive.

If f is substituted by the Shannon entropy, which is a concave function, we obtain the *Jensen-Shannon inequality* [28]:

$$JS(\pi_1, \pi_2, \ldots, \pi_n; p_1, p_2, \ldots, p_n) \equiv H\left(\sum_{i=1}^{n} \pi_i p_i\right) - \sum_{i=1}^{n} \pi_i H(p_i) \geq 0, \tag{2.39}$$

where $JS(\pi_1, \pi_2, \ldots, \pi_n; p_1, p_2, \ldots, p_n)$ is the *Jensen-Shannon divergence* of probability distributions $p_1, p_2, \ldots, p_n$ with prior probabilities or weights $\pi_1, \pi_2, \ldots, \pi_n$, fulfilling $\sum_{i=1}^{n} \pi_i = 1$. The JS-divergence measures how 'far' are the probabilities p_i from their likely joint source $\sum_{i=1}^{n} \pi_i p_i$ and equals zero if and only if all the p_i are equal. It is important to note that the JS-divergence is identical to $I(X,Y)$ when $\pi_i = p(x_i)$ and $p_i = p(Y|x_i)$ for each $x_i \in \mathcal{X}$, where $p(X) = \{p(x_i)\}$ is the input distribution, $p(Y|x_i) = \{p(y_1|x_i), p(y_2|x_i), \ldots, p(y_m|x_i)\}$, $n = |\mathcal{X}|$, and $m = |\mathcal{Y}|$ [28, 151].

2.5.3.2 The log-sum inequality

Log-sum inequality: If $a_1, a_2, \ldots, a_n$ and $b_1, b_2, \ldots, b_n$ are non-negative numbers, then

$$\sum_{i=1}^{n} a_i \log \frac{a_i}{b_i} \geq \left(\sum_{i=1}^{n} a_i\right) \log \frac{\sum_{i=1}^{n} a_i}{\sum_{i=1}^{n} b_i}, \tag{2.40}$$

with equality if and only if $\frac{a_i}{b_i} = constant$.

Note that the conditions in this inequality are much weaker than for Jensen's inequality.

From this inequality, certain results can be derived:

1. $D_{KL}(p\|q)$ is convex in the pair (p,q).
2. $H(X)$ is a concave function of p.
3. If X and Y have the joint pdf $p(x,y) = p(x)p(y|x)$, then $I(X,Y)$ is a concave function of $p(x)$ for fixed $p(y|x)$ and a convex function of $p(y|x)$ for fixed $p(x)$.

2.5.3.3 Data processing inequality

Data processing inequality: If $X \to Y \to Z$ is a Markov chain, then

$$I(X,Y) \geq I(X,Z). \tag{2.41}$$

This result demonstrates that no processing of Y, deterministic or random, can increase the information that Y contains about X.

2.5.4 Information Bottleneck Method

The information bottleneck method, introduced by Tishby et al. [156], extracts a compact representation of the variable X, denoted by $\widehat{X}$, with minimal loss of MI with respect to another variable Y (i.e., $\widehat{X}$ preserves as much information as possible about the relevant variable Y). Soft [156] and hard [150] partitions of X can be adopted. In the first case, every cluster $x \in \mathscr{X}$ can be assigned to every cluster $\hat{x} \in \widehat{\mathscr{X}}$ with some conditional probability $p(\hat{x}|x)$ (soft clustering). In the second case, every cluster $x \in \mathscr{X}$ is assigned to only one cluster $\hat{x} \in \widehat{\mathscr{X}}$ (hard clustering).

In this subsection, we focus our attention on the *agglomerative information bottleneck method* [150]. Given a cluster $\hat{x}$ defined by $\hat{x} = \{x_1, \ldots, x_l\}$, where $x_k \in \mathscr{X}$, and given probability distributions $p(\hat{x})$ and $p(y|\hat{x})$ defined by

$$p(\hat{x}) = \sum_{k=1}^{l} p(x_k), \tag{2.42}$$

$$p(y|\hat{x}) = \frac{1}{p(\hat{x})} \sum_{k=1}^{l} p(x_k, y) \quad \forall y \in \mathscr{Y}, \tag{2.43}$$

the following properties are fulfilled:

- The decrease in the mutual information $I(X,Y)$ due to the merge of $x_1, \ldots, x_l$ is given by

$$\delta I_{\hat{x}} = p(\hat{x}) JS(\pi_1, \ldots, \pi_l; p_1, \ldots, p_l) \geq 0, \tag{2.44}$$

  where $\pi_k = \frac{p(x_k)}{p(\hat{x})}$ and $p_k = p(Y|x_k)$. An optimal clustering algorithm has to minimize $\delta I_{\hat{x}}$.

- An optimal merge of l components can be obtained by $l-1$ consecutive optimal merges of pairs of components.

Dhillon et al. [45] presented a co-clustering algorithm applied to text-document clustering that simultaneously clusters X and Y into disjoint or hard clusters. An optimal co-clustering algorithm has to minimize the difference $I(X,Y) - I(\widehat{X},\widehat{Y})$.

2.6 Summary

In this chapter, we have introduced the fundamental basis of DTI and information theory. DTI data describe local water diffusion, calculated for each voxel, from measurements of molecular displacement in several directions with a MR device. The main diffusion directions in every voxel can be determined and, then, a three-dimensional vector field map representing fiber orientation is obtained. By extracting and manipulating this information from each voxel, we can use a set of 1D, 2D or 3D visualization techniques over the DTI data obtained. Despite the large number of algorithms dealing with the visualization of DTI data, a lot of research can be done to improve the performance, accuracy, and robustness of these techniques. In this chapter, we have also reviewed the main information theory concepts since we aim to apply information-theory tools for developing new approaches in DTI.

CHAPTER 3

Anisotropy measures

Anisotropy measures reduce the information of the tensor to a single scalar value. In this chapter, our purpose is to evaluate diffusion anisotropy from diffusion tensor imaging using new measures derived from Hellinger divergences and from compositional data distances. The evaluation was done using the 3 Phase-plot. The measures were compared with regard to their sensitivity to detect white and grey matter changes on human brain. The proposed compositional Kullback-Leibler Anisotropy and the classical Fractional Anisotropy showed a similar behavior, although Kullback-Leibler Anisotropy detects the transitions between white and grey matter more accurately, and shows a better discrimination in areas with great confluence of fibers.

3.1 Introduction

DTI characterizes the water diffusion in tissue on a voxel by voxel basis representing the local diffuse behavior of water in a voxel by a second order symmetric positive tensor **D**. Since the advent of DTI, its processing, analysis and visualization have become main focuses of research in medical imaging. The challenge is on the development of strategies to extract and visualize information from the tensor data in a comprehensive manner, i.e., using local and global information simultaneously. The amount of information contained in datasets exacerbates the task of effectively communicating information to use in diagnosis.

To tackle this problem, some authors [19, 128, 39, 174] proposed to reduce the information of the tensor to a single scalar value representing an anisotropy measure 1D. In this way, classical visualization techniques could be applied and DTI graphical representations could be obtained. Since the complete description of diffusion tensor cannot be fully characterized by a simple scalar quantity, the obtained visualizations represent only a small part of the tensor information. However, these images are easily interpreted and used as a first step towards the identification of normal and pathological brain tissue.

In this chapter, we will focus on measures that reduce the 6D information of the tensor to a 1D scalar value. Our goal is to propose new measures and compare them with the classical ones. We will consider measures from two different families, on the one hand, the Matusita and the Logarithmic anisotropies, that can be derived from the family of Hellinger divergences, and, on the other hand, the Aitchison and Compositional Kullback-Leibler anisotropies, which can be deduced from a compositional approach [3, 107]. To evaluate and compare the measures, we will use the ternary diagram, also referred to as a reference triangle or a barycentric coordinate space [2]. In the context of DTI data, this graphical representation was first proposed by Alexander et al. [6]. In this chapter, we extend their work with a detailed description of the foundations behind it. As a result, we obtain a framework that can be used to evaluate any 1D measure extracted from a tensor. Finally, we give a detailed description of the study that has been carried out to evaluate the different measures on several volumes of interest located in white matter (WM), grey matter (GM), and cerebrospinal fluid (CSF) of five normal volunteers. The obtained results will show the good-performance of the Kullback-Leibler measure with respect to classical measures.

This chapter has been structured as follows. Section 3.2 presents different anisotropy measures and the ternary diagram. Section 3.3 proposes new anisotropy measures. Section 3.4 describes our validation methodology. Section 3.5 and Section 3.6 show the results obtained and discussion, respectively. Finally, Section 3.7 presents the conclusions.

3.2 Background and Related Work

In this section, we introduce the most basic anisotropy measures and the concept of the 3 Phase-plot (3P-plot).

3.2.1 Diffusion Anisotropy Measures

As we have presented in the previous chapter, the diffusion tensor **D** can be described by a 3×3 symmetric matrix, where D_{ij} is the diffusion coefficient measured in the ijth direction:

$$\mathbf{D} = \begin{pmatrix} D_{xx} & D_{xy} & D_{xz} \\ D_{yx} & D_{yy} & D_{yz} \\ D_{zx} & D_{zy} & D_{zz} \end{pmatrix}$$

Diagonalization of **D** provides three eigenvalues $\lambda_1 \geq \lambda_2 \geq \lambda_3 \geq 0$ and three eigenvectors $\mathbf{e}_1, \mathbf{e}_2$ and $\mathbf{e}_3$ that define the directions of main, medium and minimum diffusivity, respectively [16]. Based on λ_1, λ_2 and λ_3, different measures to quantify the diffusion tensor properties have been proposed [134, 39, 174, 162]. In Table 3.1 we summarize the most representative scalar indices: *Trace*, *Mean Diffusivity* ($\langle\lambda\rangle$), *Fractional Anisotropy* (*FA*), *Relative Anisotropy* (*RA*), *Volume Ratio* (*VR*), *linear coefficient* (Cl), *planar coefficient* (Cp), and *spherical coefficient* (Cs). For each index we describe the equation that defines it and also its interpretation.

In medical environments, the most common strategy to interpret these measures are grey and color coded images generated by mapping measure values to intensities. A main limitation of scalar measures is that they represent only part of the tensor information. As we have seen in Section 2.3.2 and Section 2.3.3, more detailed information can be obtained using 2D and 3D visualizations techniques.

3.2.2 From the Barycentric Diagram to the 3 Phase-plot

The shape of a diffusion ellipsoid is inherently related to the eigenvalues and eigenvectors of the diffusion tensor since the three principal radii are proportional to the eigenvalues and the axes of the ellipsoid aligned with the three orthogonal eigenvectors of the diffusion tensor [171]. In this context, we can define the relative *importance* of each ellipsoid axis as

$$p_i = \frac{\lambda_i}{\text{trace}}, i = 1, 2, 3, \tag{3.1}$$

where trace $= \lambda_1 + \lambda_2 + \lambda_3$ represents the diffusion magnitude. The importance can be interpreted as the percentage of diffusion associated to the orthogonal direction, and then the different geometric shapes can be determined by the relative values of $p_1 \geq p_2 \geq p_3 \geq 0$, where $p_1 + p_2 + p_3 = 1$. The *importance vector* $\overrightarrow{p} = (p_1, p_2, p_3)$ belongs to the unit simplex S^3, i.e., the sample space of compositional data $S^3 = \{x = (x_1, x_2, x_3) : x_1 > 0, x_2 > 0, x_3 > 0; \sum x_i = k\}$, where k is a constant, generally 1

Indices	Equation	Interpretation
Trace	$\text{trace} = \lambda_1 + \lambda_2 + \lambda_3$	The *trace* can be seen as the orientational diffusivity or diffusion magnitude [17].
Mean diffusivity ($\langle\lambda\rangle$)	$\langle\lambda\rangle = \frac{\text{trace}}{3}$	It characterizes the overall mean-squared displacement of molecules and the overall presence of obstacles to diffusion [19].
Fractional Anisotropy (FA)	$FA = \sqrt{\frac{3}{2}} \frac{\sqrt{(\lambda_1-\langle\lambda\rangle)^2+(\lambda_2-\langle\lambda\rangle)^2+(\lambda_3-\langle\lambda\rangle)^2}}{\sqrt{(\lambda_1)^2+(\lambda_2)^2+(\lambda_3)^2}}$	FA measures how far the tensor is from a sphere [19].
Relative anisotropy (RA)	$RA = \frac{\sqrt{6}}{6} \frac{\sqrt{(\lambda_1-\langle\lambda\rangle)^2+(\lambda_2-\langle\lambda\rangle)^2+(\lambda_3-\langle\lambda\rangle)^2}}{\langle\lambda\rangle}$	Ratio of the magnitudes of the anisotropic and isotropic parts of the diffusion tensor [19].
Volume Ratio (VR)	$VR = \frac{\lambda_1\lambda_2\lambda_3}{\langle\lambda\rangle^3}$	Ratio of ellipsoid volume to sphere volume with the same eigenvalue mean [14].
Linear Coefficient (Cl)	$Cl = \frac{\lambda_1-\lambda_2}{\lambda_1+\lambda_2+\lambda_3}$	Linear case, anisotropic diffusion. We can observe highly organized white matter regions [173].
Planar Coefficient (Cp)	$Cp = \frac{2(\lambda_2-\lambda_3)}{\lambda_1+\lambda_2+\lambda_3}$	Planar case, planar diffusion. It is generally associated with diffusion sheets or may describe regions of crossing fibers [173].
Spherical Coefficient (Cs)	$Cs = \frac{3\lambda_3}{\lambda_1+\lambda_2+\lambda_3}$	Spherical case, isotropic diffusion. Grey matter and fluids such as CSF [173].

Table 3.1: Scalar indices which reduce the 6D information of a tensor to a scalar value. For each index we present the equation required to obtain it and also its interpretation.

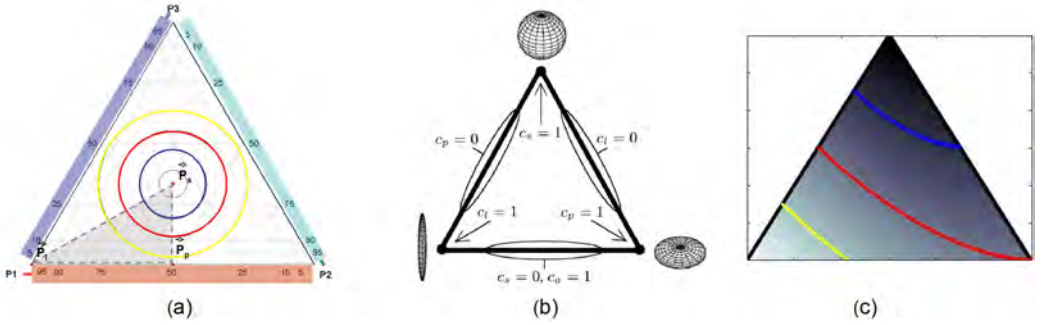

Figure 3.1: (a) The ternary diagram (b) The 3P-plot, and (c) Representation of *RA* in the 3P-plot.

for proportions and 100 for percentages [2]. In other words, compositional data are vectors of positive components whose sum is a constant.

A well-known strategy to graphically interpret data from the simplex is the *ternary diagram*, also referred to as *reference triangle*, *barycentric coordinate space* or *Finetti diagram* [2]. Figure 3.1(a) illustrates a ternary diagram with vertices P_1, P_2, and P_3. This triangle is equilateral, has an altitude of one and for any vector $\overrightarrow{p} = (p_1, p_2, p_3)$ in the triangle the perpendiculars p_1, p_2 and p_3 from $\overrightarrow{p}$ to the opposite sides P_1, P_2, and P_3, satisfies $p_1 + p_2 + p_3 = 1$. The importance vectors: $\overrightarrow{P_l} = (1,0,0)$, $\overrightarrow{P_p} = (1/2, 1/2, 0)$, and $\overrightarrow{P_s} = (1/3, 1/3, 1/3)$ which are respectively associated to the linear, planar, and spherical shapes previously described are also represented in the diagram. Observe that $\overrightarrow{P_l}$ is located in the bottom-left corner P_1, $\overrightarrow{P_p}$ in the middle of the bottom edge, and the spherical shape $\overrightarrow{P_s}$ is the barycenter of the triangle. Moreover, since any importance vector $\overrightarrow{p}$ verifies that $p_1 \geq p_2 \geq p_3$ any geometric shape associated to the diffusion ellipsoid is located in the bottom-left part of the ternary diagram, i.e., the triangle with the vertices $\overrightarrow{P_l}$, $\overrightarrow{P_p}$, $\overrightarrow{P_s}$. Therefore, to interpret tensor data we have to consider only this part of the diagram. In order to enhance the interpretation, the triangle $\overrightarrow{P_l}$, $\overrightarrow{P_p}$, $\overrightarrow{P_s}$ we can use the 3P-plot represented in Figure 3.1(b), where the triangle $\overrightarrow{P_l}$, $\overrightarrow{P_p}$, $\overrightarrow{P_s}$ has been transformed in a full triangle with the vertices corresponding to linear (Cl), planar (Cp), and spherical (Cs) shapes, respectively.

These two representations, the ternary diagram (see Figure 3.1(a)) and the 3P-plot (see Figure 3.1(b)), are related by the expressions:

$$Cl = p_1 - p_2 = \frac{\lambda_1 - \lambda_2}{3\langle\lambda\rangle}, \tag{3.2}$$

$$Cp = 2(p_2 - p_3) = \frac{2(\lambda_2 - \lambda_3)}{3\langle\lambda\rangle}, \text{ and} \tag{3.3}$$

$$Cs = 3p_3 = \frac{\lambda_3}{\langle\lambda\rangle}, \tag{3.4}$$

where $\langle\lambda\rangle = \text{trace}/3$ is the mean diffusion magnitude. In this way, any importance

vector $\overrightarrow{p}$ can be transformed into a vector shape $\overrightarrow{C} = (Cl, Cp, Cs)$. For instance, the spherical isotropic case $\overrightarrow{P_s} = (1/3, 1/3, 1/3)$ converts into the top vertex $(0, 0, 1)$ in the 3P-plot.

The anisotropy measures emphasize different tensor features and hence they can lead to confusion in interpreting results from different studies. The advantage of this framework is that it provides us with an environment that can be used to graphically analyze the behavior of diffusion anisotropy measures interpreting them as the distance from the importance vector $\overrightarrow{p}$ to the spherical isotropic case ($\overrightarrow{P_s} = (1/3, 1/3, 1/3)$).

As an example, consider Figure 3.1(c) which corresponds to the graphical representation of

$$RA = s\left(\frac{\sqrt{(\lambda_1 - \langle\lambda\rangle)^2 + (\lambda_2 - \langle\lambda\rangle)^2 + (\lambda_3 - \langle\lambda\rangle)^2}}{\langle\lambda\rangle}\right), \tag{3.5}$$

where $s(x) = \frac{\sqrt{6}}{6}x$ is a function for scaling the measure from 0 (isotropic) to 1 (anisotropic) cases. Observe that the numerator measures the Euclidean distance between the vector $\overrightarrow{\lambda}$ and the vector $\overrightarrow{\langle\lambda\rangle} = (\langle\lambda\rangle, \langle\lambda\rangle, \langle\lambda\rangle)$ corresponding to the spherical tensor with the same eigenvalue mean. In the denominator, we have the norm of the vector $\overrightarrow{\langle\lambda\rangle}$. Applying Equation 3.1, it turns out that *RA* (Equation 3.5) is equivalent to

$$RA = \frac{\sqrt{6}}{2}\sqrt{(p_1 - 1/3)^2 + (p_2 - 1/3)^2 + (p_3 - 1/3)^2} = \frac{\sqrt{6}}{2}d_e(\overrightarrow{p}, \overrightarrow{P_s}). \tag{3.6}$$

From this expression it can be seen that *RA* simply calculates the Euclidean distance d_e between the percentage diffusion vector and the spherically isotropic case. The isocontours represented in Figure 3.1(c) correspond to the 0.25, 0.5, and 0.75 anisotropy levels, and the brightest areas to the anisotropic voxels, the darkest to the isotropic, and the grey intensities to intermediate anisotropy values.

This interpretation of the anisotropy measures suggests us the possibility to define new measures using different distances over the sphere. Some of these measures are presented below.

3.3 New anisotropy measures

The new set of anisotropy measures proposed in this section are inspired by the compositional origin of the 3P plot. For their evaluation, we will compare them with *FA*, considered the best measure in a similar study carried out by Alexander et al. [6]. Different to them, we propose to look for the best anisotropy measure by considering more accurately the measure when there is greater discrimination from the spherical case.

Since the degree of discrimination can be expressed as a distance, in our study we will consider three different families of distances. All the considered measures are listed in Table 3.2. They have been expressed in terms of λ's and also in terms of p's and, in order to be representable in the 3P-plot, they have been scaled from 0

(isotropic) to 1 (anisotropic) using a specific function $s(x)$. Let us describe the most important features of these measures.

(i) In the first group of measures we consider is *FA* and the Angular Anisotropy (*AA*), represented in the first and second rows of Table 3.2, respectively. *FA* [19] is very similar to *RA*. Both, in their numerator, measure the Euclidean distance between the vector $\overrightarrow{\lambda}$ and the vector $\overrightarrow{\langle\lambda\rangle}$. While the value $\langle\lambda\rangle$ appears in the denominator of *RA*, *FA* includes the norm of the vector $\overrightarrow{\lambda}$. On the other hand, *FA* projects the percentage diffusion vector $\overrightarrow{p}$ –or equivalently $\overrightarrow{\lambda}$– into the unit sphere and calculates the Euclidean distance to its mean vector. On the other hand, *AA* measures the angular separation between the vector $\overrightarrow{\lambda}$ and the vector $\overrightarrow{\langle\lambda\rangle}$ [167]. *AA* also measures the angular separation between the projection of the vectors $\overrightarrow{p}$ and $\overrightarrow{P_s}$. In order to reproduce the study carried out by Alexander in [6], we include in this first group the Component Anisotropic index (CA), obtained from the sum of linear and planar shape measures, i.e., $CA = Cl + Cp$.

(ii) In the second group of measures, we consider two Hellinger distances [141]: Matusita (*MA*) and Logarithmic (*LA*), represented in the third and fourth rows of Table 3.2, respectively. By analogy to *FA*, *MA* calculates the Matusita distance between the vectors $\overrightarrow{\lambda}$ and $\overrightarrow{\langle\lambda\rangle}$, and divides it by the Matusita norm of the vector $\overrightarrow{\lambda}$. It is well known that another possibility of projecting percentage diffusion vectors $\overrightarrow{p}$ into the unit sphere consists simply taking its square root. In this regard, *MA* is also equivalent to project $\overrightarrow{p}$ and $\overrightarrow{P_s}$ and measures its Euclidean distance. The Matusita distance is functionally related to the Chord and the Bhattacharyya distances [141]. All are widely used in several areas such as paleontology or genetics. In information theory, Matusita distance belongs to the family of Hellinger divergences. In this family, the Euclidean and the Logarithmic distances are also included. In this second group of anisotropy measures, we also consider the *LA* measure which is based on the Euclidean distance between the logarithm transformed vectors of $\overrightarrow{\lambda}$ and $\overrightarrow{\langle\lambda\rangle}$. Equivalently, *LA* log-transforms the vectors $\overrightarrow{p}$ and $\overrightarrow{P_s}$ and calculates its Euclidean distance.

(iii) In the third group, we consider two compositional data measures: Aitchison (*AitA*) and compositional Kullback-Leibler (*KLA*), represented in the fifth and sixth rows of Table 3.2. To calculate the *AitA* measure, we take the logarithm of vector $\overrightarrow{\lambda}$, and then we calculate the Euclidean distance between this vector $\overrightarrow{\ln(\lambda)}$ and the mean vector $\langle\overrightarrow{\ln(\lambda)}\rangle$. In other words, *AitA* is based on the Aitchison distance [3].

In terms of importance vectors, the *AitA* measure is equivalent to measuring the Aitchison distance between the compositional vectors $\overrightarrow{p}$ and $\overrightarrow{P_s}$. The Aitchison distance is widely used in compositional data analysis for non-parametrics problems. On the other hand, Martín-Fernàndez et al. [107] proposed a different compositional measure of difference which is related to the Kullback-Leibler di-

vergence. Using this measure, we consider the measure of anisotropy KLA which consists in calculating the divergence between the compositional vectors $\overrightarrow{p}$ and $\overrightarrow{P_s}$ or the divergence between the vectors $\overrightarrow{\lambda}$ and $\overrightarrow{\langle\lambda\rangle}$.

In Figure 3.2, the intensity maps of each of the studied measures are illustrated. Observe the different behaviour of the measures with respect to the tensor shapes. In addition, note that the KLA measure produces isocontours more spreadly distributed on the 3P-plot. This behavior suggests the capability of KLA to reasonably discriminate between the different tensor shapes.

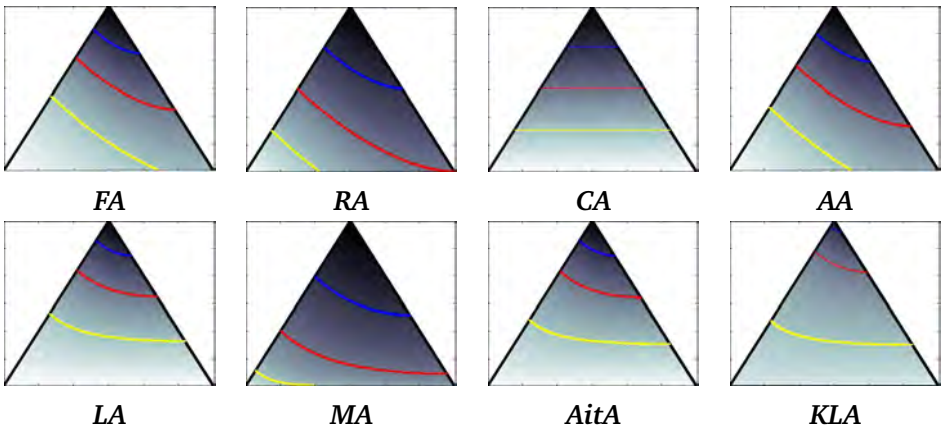

Figure 3.2: Evaluation of anisotropy measures in the 3P-plots. The brightest voxels correspond to the case with anisotropy = 1, the darkest voxels correspond to the isotropic case and the grey intensities correspond to intermediate anisotropy values. It is clear from these intensity maps that each anisotropy measure has significantly different dependencies on the tensor shape. In particular, each anisotropy measure is weighted very differently by the planar anisotropy.

3.4 Methodology

In this section, we introduce the methodology used to compare different anisotropy measures.

3.4.1 Index of Detectability

Broadly speaking, in our context, detectability refers to an ability to correctly identify events that are non chance regardless of how dramatic or subtle. The capability of a measure to discriminate between tissue classes can be expressed in terms of detectability. This detectability can be produced by comparison of the arithmetical means of the anisotropy values for the samples of tissues. In particular, the detectability index proposed in this work is based on the usual standardized difference between two sample means A_1 and A_2:

Measure	Lambda version	Probability version	Scale function
(1) FA	$s\left(\frac{\sqrt{(\lambda_1-\langle\lambda\rangle)^2+(\lambda_2-\langle\lambda\rangle)^2+(\lambda_3-\langle\lambda\rangle)^2}}{\sqrt{\lambda_1^2+\lambda_2^2+\lambda_3^2}}\right)$	$s\left(\frac{\sqrt{(p_1-1/3)^2+(p_2-1/3)^2+(p_3-1/3)^2}}{\sqrt{p_1^2+p_2^2+p_3^2}}\right)$	$\sqrt{\frac{3}{2}}x$
(2) AA	$s\left(\arccos\left(\sum_{i=1}^{3}\frac{\lambda_i}{\sqrt{\sum_{j=1}^{3}\lambda_j^2}}\frac{\langle\lambda\rangle}{\sqrt{\sum_{j=1}^{3}\langle\lambda\rangle^2}}\right)\right)$	$s\left(\arccos\left(\sum_{i=1}^{3}\frac{p_i}{\sqrt{\sum_{j=1}^{3}p_j^2}}\frac{1/3}{\sqrt{\sum_{j=1}^{3}1/3^2}}\right)\right)$	$\frac{x}{\arccos\left(\sqrt{1/3}\right)}$
(3) LA	$s\left(\sqrt{\sum_{i=1}^{3}\left(\ln\left(\lambda_i\right)-\ln\left(\langle\lambda\rangle\right)\right)^2}\right)$	$s\left(\sqrt{\sum_{i=1}^{3}\left(\ln\left(p_i\right)-\ln(1/3)\right)^2}\right)$	$1-\exp\left(-x\right)$
(4) MA	$s\left(\frac{\sqrt{\sum_{i=1}^{3}\left(\sqrt{\lambda_i}-\sqrt{\langle\lambda\rangle}\right)^2}}{\sqrt{\sum_{i=1}^{3}\lambda_i}}\right)$	$s\left(\sqrt{\sum_{i=1}^{3}\left(\sqrt{p_i}-\sqrt{1/3}\right)^2}\right)$	$\frac{x}{\sqrt{2}\sqrt{1-\sqrt{1/3}}}$
(5) AitA	$s\left(\sqrt{\sum_{i=1}^{3}\left(\ln\left(\lambda_i\right)-\frac{1}{3}\sum_{j=1}^{3}\ln\left(\lambda_j\right)\right)^2}\right)$	$s\left(\sqrt{\sum_{i=1}^{3}\left(\ln\left(\frac{p_i}{g(\overrightarrow{p})}\right)-\ln\left(\frac{1/3}{g(\overrightarrow{P_s})}\right)\right)^2}\right)$	$1-\exp\left(-x\right)$
(6) KLA	$s\left(\sqrt{\frac{3}{2}}\sqrt{\ln\left(\left(\frac{1}{3}\sum_{i=1}^{3}\frac{\lambda_i}{\langle\lambda\rangle}\right)\left(\frac{1}{3}\sum_{j=1}^{3}\frac{\langle\lambda\rangle}{\lambda_j}\right)\right)}\right)$	$s\left(\sqrt{\frac{3}{2}}\sqrt{\ln\left(\left(\frac{1}{3}\sum_{i=1}^{3}\frac{p_i}{1/3}\right)\left(\frac{1}{3}\sum_{j=1}^{3}\frac{1/3}{p_j}\right)\right)}\right)$	$tanh\sqrt{(x)}$

Table 3.2: Anisotropy measures. From left to right, index name, lambda version of equation using the eigenvalues, probability version of equation using the importance vector, and scale function applied to be representable in the 3P-plot.

$$d = \frac{< A_1 > - < A_2 >}{\sqrt{\frac{\sigma_1^2}{N_1} + \frac{\sigma_2^2}{N_2}}}, \tag{3.7}$$

where N_1 and N_2 respectively are the sample sizes of each tissue, and σ_1, σ_2 are the variances of the anisotropy values for the two tissue classes. Note that when the two tissue samples have the same size then the index (see Equation 3.7) is equivalent to the index proposed in [6]. In the other cases, d is more general than the approximation proposed in [6] since it takes into account the size of the samples as is usual in statistical analysis

Our objective is to obtain the anisotropy measure with the greatest detectability index, i.e., the measure that better detects white matter changes. With this purpose in mind, we will evaluate the behavior of each measure on different real DTI datasets.

3.4.2 Protocol

Data was acquired as follows. DTI was performed on five volunteers. Consent was obtained from all subjects in accordance with the guidelines of the Hospital Universitari Josep Trueta of Girona institutional review board for human subject studies.

Images were obtained using a Gyroscan Intera NT 1.5T scanner (Philips Medical Systems, Best, the Netherlands) whose hardware consists of 22 mT/m and maximum slew rate of 120 mT/m per millisecond.

DTI data was acquired by using a single-shot echo-planar imaging sequence with parallel-imaging scheme (acceleration factor of 3) using b values of 0 and 1000 sec/mm^2. Coverage of the full cerebrum was obtained by acquiring fifty-five 2.5 mm thick slices without gap.

Imaging matrix was 96×96 zero filled to 192×192, with a field of view of 230×230 mm and resultant voxel dimensions were $1.2\times1.2\times2.5$ mm^3. Other imaging parameters used were $TR = 9500msec$, $TE = 79msec$, $NEX = 5$. The data sets were acquired along fifteen different diffusion directions using a rotated frame of reference known as "Gradient overplus" (Philips Medical Systems) that resulted in greater gradient strength and shorter TE values.

Furthermore, a volumetric $T1$ weighted fast field echo was acquired for anatomic guidance. The scan parameters were field of view 240×240, $TR = 25ms$, $TE = 4.6ms$, *flip angle*=30^o and voxel size was $1\times1\times1$ mm. Total scan time for each volunteer was approximately 25 minutes.

3.4.3 VOI Selection

To obtain tissue specific statistics for all the measures, we have selected representative grey and white matter regions of the brain (see Figure 3.3). The evaluated grey matter regions are cortical grey matter, striatum, and the thalamus. The white matter regions are subcortical white matter corresponding to short association fibers, also known as u-fibers, corpus callosum corresponding to commissural fibers, arcuate fasciculus, and

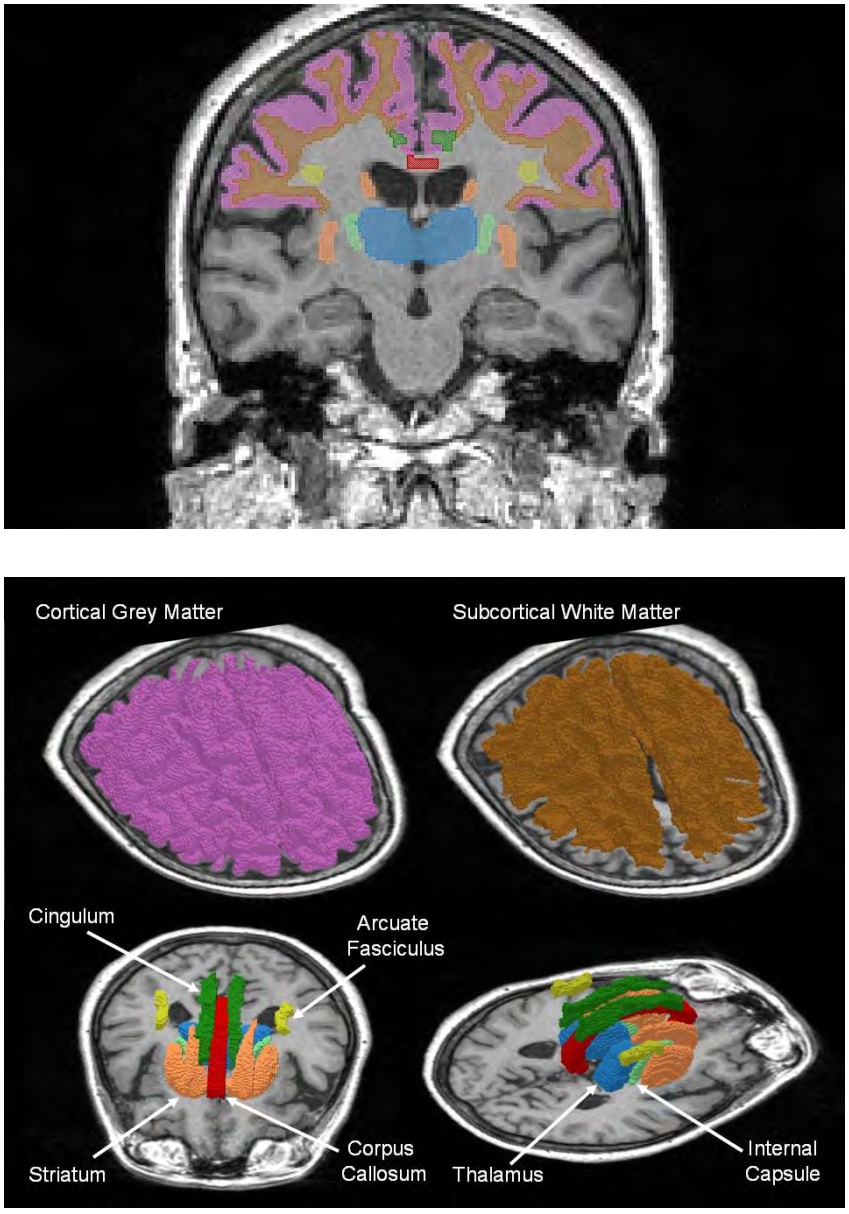

Figure 3.3: Brain regions considered in the evaluation of anisotropy measures: grey matter, subcortical white matter, internal capsule, arcuate fasciculus, corpus callosum, cingulum, striatum, and thalamus.

cingulum corresponding to long association fibers, and internal capsule corresponding to projection fibers. To avoid possible bias in favor of a certain anisotropy measure, we used for the selection of the VOIs a high resolution $T1$ image. To ensure the spatial correspondence, a 12-parameter affine registration between $T1$ and the b_0 images has been performed. The selection of the volume of interest (VOI) has been done using AMIRA 3.1 software[155].

The T1 image has been segmented using SPM5 [11] obtaining three probability maps: grey matter (GM), white matter (WM), and cerebrospinal fluid (CSF).

To select cortical grey matter voxels, a threshold of 0.7 has been applied to the GM image. The obtained mask (GMm) has been superimposed with the $T1$ image and the misclassified voxels have been removed. The VOI only contains the voxels upper to the axial plane superior to the thalamus.

To obtain subcortical white matter VOI, a three-step process has been done: (i) the mask (WMm) from the probability map of white matter with a 0.7 threshold has been obtained, (ii) a three voxels dilatation of GMm has been performed, and (iii) the intersection of WMm and the dilated GMm has been done obtaining the subcortical white matter VOI.

The corpus callosum voxels have been selected from the 10 mid-sagittal slices of the WMm.

The thalamus and the striatum (including putamen, caudate nucleus, and accumbens bilateraly) have been obtained manually using the 3D editor of AMIRA.

The cingulum has been selected from the subcortical white matter VOI considering the underlying cingulate gyrus voxels.

To delimit the arcuate fasciculus voxels (also named superior longitudinal fasciculus), we draw circular regions of interest (ROI), on coronal sections from the anterior pole to the posterior pulvinar of the thalamus. ROIs were specifically located over the $T1$ white matter above circular insular sulcus that do not intersect with the subcortical white matter VOI.

Finally, the internal capsule VOI has been manually delimited on the T1 map using a prelabel of the WM probability map and comparing the *FA* color and the T1 maps to perform corrections.

Furthermore, we have verified the correspondence of all subcortical VOIS (thalamus, striatum, arcuate fasciculus, cingulum, and internal capsule) with the *FA* and the *FA* color maps. Finally, a smooth filter to all the VOIS has been applied (see Figure 3.4). As seen in Figure 3.3, there are no intersections between the VOIs considered in the study.

3.5 Results

Figure 3.2 shows in the 3P-plot the different anisotropy measures considered in our study. In order to compare the shapes of the plots with the images of the measures, we present in Figure 3.6 the T1 map with some of the evaluated VOIs and the images of the anisotropy measures for one of the studied subjects. All the maps are scaled to the

same relative grey scale range (0 to 255).

To analyze the behavior of the measures, all voxels from a given VOI type in all subjects were pooled and then we computed the mean and standard deviation of the anisotropy measures for each of the evaluated VOIs. These results are listed in Table 3.3. For each VOI, the parameter N represents the number of voxels defining the VOI. From the data of Table 3.3, we computed the coefficient of variation (CV), that is, the ratio of the standard deviation to the mean. The obtained results are plotted in Figure 3.7. Table 3.4 collects the detectability indices d (Equation 3.7) for different pairs of tissues. Detectability indicates the capability of a measure to discriminate between tissue classes, so the greater the value the better the measure.

The good performance of the KLA measure leads us to compare it with the FA. In Figure 3.5, we evaluate the capability of these measures to separate tissues by representing both measures simultaneously in the 3P-plot. For each tissue, the mean and standard deviation of its Cl, Cp, and Cs values have been calculated and represented as a point and a contour, respectively. To evaluate the ability of FA and KLA to discriminate white matter voxels, we designed a test where for each of the measures we select the voxels where the measure is greater than the mean of the subcortical white matter, (i.e., $FA > 0.363$ and $KLA > 0.541$). These thresholds represent the boundary between grey matter and white matter. We calculate the difference between KLA and FA masks, and we only consider the voxels contained in the WM mask. Figure 3.8 illustrates the obtained images where the yellow voxels are voxels of WM that have been detected by both KLA and FA, red voxels are the ones that have been detected by KLA and not by FA, and the blue voxels are the ones detected by FA and not by KLA.

3.6 Discussion

As expected, white matter features appear different for each of the anisotropy measures (see Figure 3.6). In a first visual inspection, we can observe that the differences between FA and AA maps are practically indistinguishable, and that LA and $AitA$ are

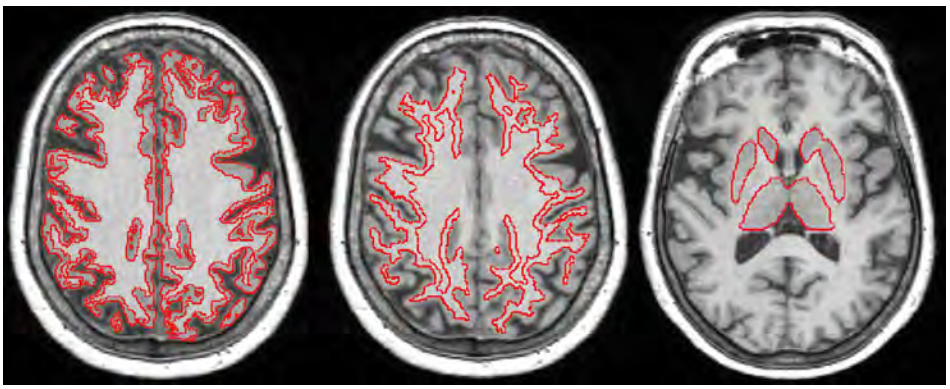

Figure 3.4: Representative axial regions of grey matter, subcortical white matter and striatum and thalamus ROIS considered for the evaluation of anisotropy measures.

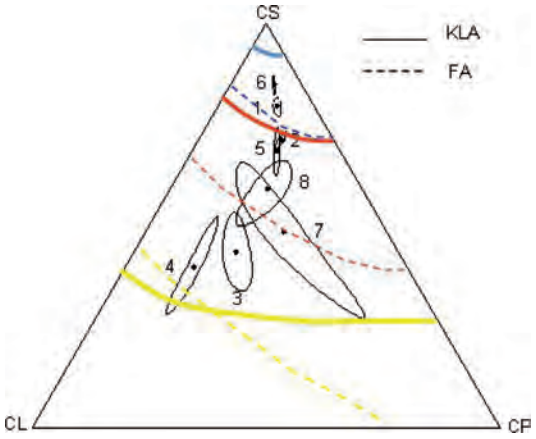

Figure 3.5: KLA and FA isometric contour lines superimposed on a 3P-plot where the distributions of the tissue shape measurements are also represented. The different labels correspond to: (1) Striatum, (2) Thalamus, (3) Internal Capsule, (4) Corpus Callosum, (5) Subcortical White Matter, (6) Grey Matter, (7) Arcuate Fasciculus, and (8) Cingulum.

	FA	RA	CA	AA	LA	MA	$AitA$	KLA
GM($N = 202200$)	**0.194**	**0.116**	**0.189**	**0.168**	**0.193**	**0.066**	**0.180**	**0.401**
Standard deviation	0.110	0.071	0.117	0.098	0.113	0.045	0.101	0.103
CING($N = 3645$)	**0.459**	**0.300**	**0.445**	**0.408**	**0.460**	**0.178**	**0.402**	**0.601**
Standard deviation	0.173	0.135	0.174	0.162	0.177	0.086	0.149	0.109
EST($N = 21929$)	**0.250**	**0.151**	**0.243**	**0.217**	**0.250**	**0.087**	**0.230**	**0.455**
Standard deviation	0.121	0.081	0.120	0.108	0.123	0.049	0.106	0.097
TH($N = 15970$)	**0.330**	**0.202**	**0.323**	**0.287**	**0.332**	**0.123**	**0.301**	**0.523**
Standard deviation	0.115	0.081	0.117	0.105	0.118	0.053	0.102	0.081
SCW($N = 125449$)	**0.363**	**0.227**	**0.354**	**0.318**	**0.365**	**0.133**	**0.327**	**0.541**
Standard deviation	0.149	0.105	0.155	0.136	0.156	0.068	0.135	0.108
AF($N = 3098$)	**0.520**	**0.341**	**0.548**	**0.463**	**0.557**	**0.161**	**0.498**	**0.657**
Standard deviation	0.132	0.104	0.165	0.124	0.162	0.066	0.149	0.089
IC($N = 3549$)	**0.596**	**0.410**	**0.567**	**0.538**	**0.588**	**0.244**	**0.503**	**0.679**
Standard deviation	0.157	0.138	0.181	0.153	0.178	0.101	0.159	0.094
CC($N = 7651$)	**0.673**	**0.490**	**0.601**	**0.617**	**0.641**	**0.282**	**0.528**	**0.707**
Standard deviation	0.165	0.161	0.183	0.166	0.181	0.113	0.155	0.094

Table 3.3: Comparison of estimated means and standard deviations of the anisotropy measures as a function of tissue type from 5 volunteers.

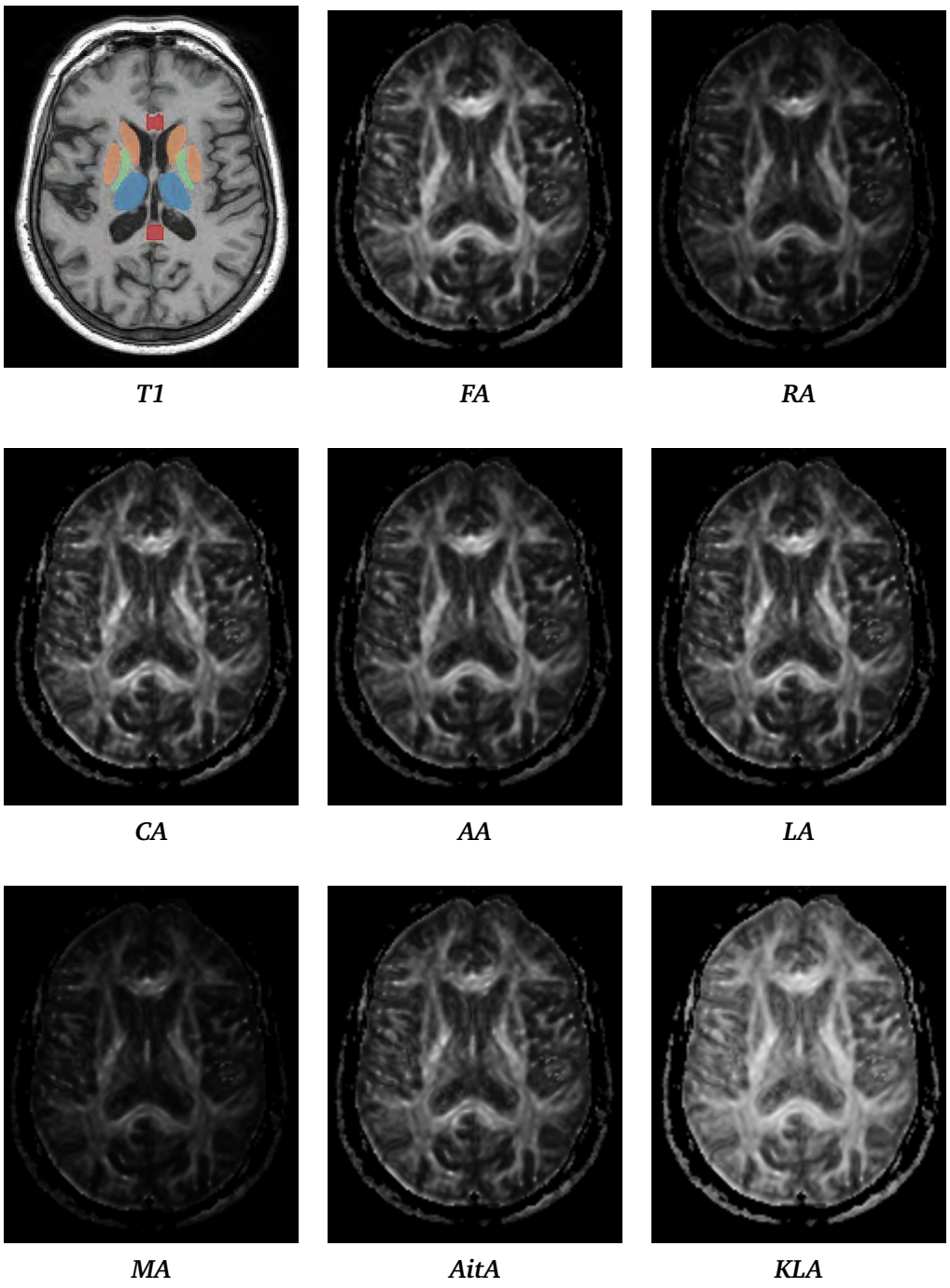

Figure 3.6: Grey scale maps corresponding to the evaluated anisotropy measures: Fractional Anisotropy (*FA*), Relative Anisotropy (*RA*), Component Anisotropic index (*CA*), Angular Anisotropy (*AA*), Logaritmic Anisotropy (*LA*), Matusita Anisotropy (*MA*), Aitchison Anisotropy ($AitA$), and Kullback-Leibler Anisotropy (KLA).

	CGM vs. CC	CGM vs. AF	CGM vs. SCW	CGM vs. IC	CGM vs. STR	CGM vs. CING	TH vs. IC	AF vs. CC	AF vs. IC	AF vs. SCW	CC vs. IC	CC vs. SCW	IC vs. SCW
FA	251.05	137.14	347.43	151.83	65.21	92.25	**95.45**	50.47	21.33	65.29	23.86	**159.80**	**87.12**
CA	195.61	120.59	324.75	123.79	62.95	88.35	76.69	14.80	4.57	64.51	9.27	115.52	69.16
RA	202.95	119.52	329.28	126.51	61.43	82.13	86.63	56.95	23.36	60.05	**26.93**	141.54	78.45
AA	235.20	131.28	342.14	143.35	64.05	89.07	92.78	52.74	22.03	63.63	24.90	154.35	84.39
LA	214.65	124.95	337.75	131.91	65.82	90.59	81.89	23.53	7.49	65.51	14.51	130.43	74.06
MA	166.34	111.64	312.24	104.32	60.50	78.38	68.73	**78.25**	**43.58**	31.75	17.86	113.47	64.43
AitA	194.60	118.74	332.55	121.11	66.90	89.98	72.59	9.28	1.47	63.39	7.56	110.62	65.61
KLA	**279.17**	**159.13**	**367.28**	**174.40**	**77.70**	**109.76**	91.66	26.09	9.86	**71.72**	14.66	149.28	86.11

Table 3.4: Estimated corrected detectabilities between selected tissue groups for each of the shape and anisotropy measures. The anisotropy measure with the greatest separability is highlighted in boldface.

Volunteer	KLA	FA
1	4471	335
2	5432	313
3	6166	396
4	5796	350
5	5780	376
Mean	*5529*	*354*
Standard deviation	*645.92*	*32.81*

Table 3.5: Difference in the number of voxels detected by *KLA* and *FA*.

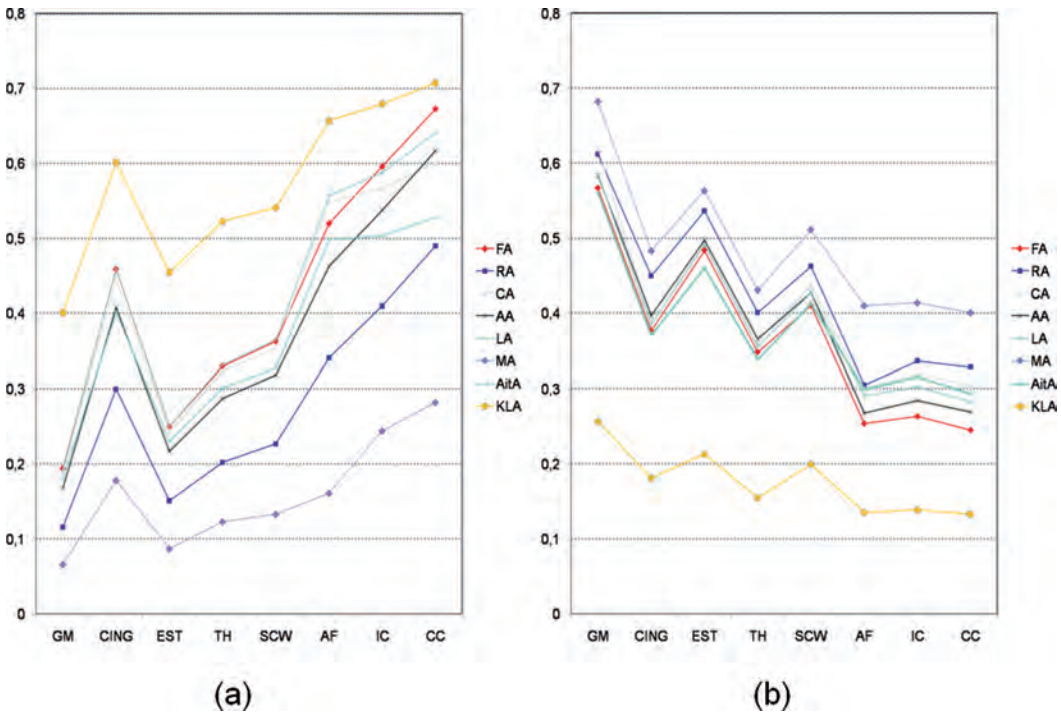

Figure 3.7: For each of the evaluated VOIs, (a) the mean of the anisotropy measures, and (b) the coefficient of variation.

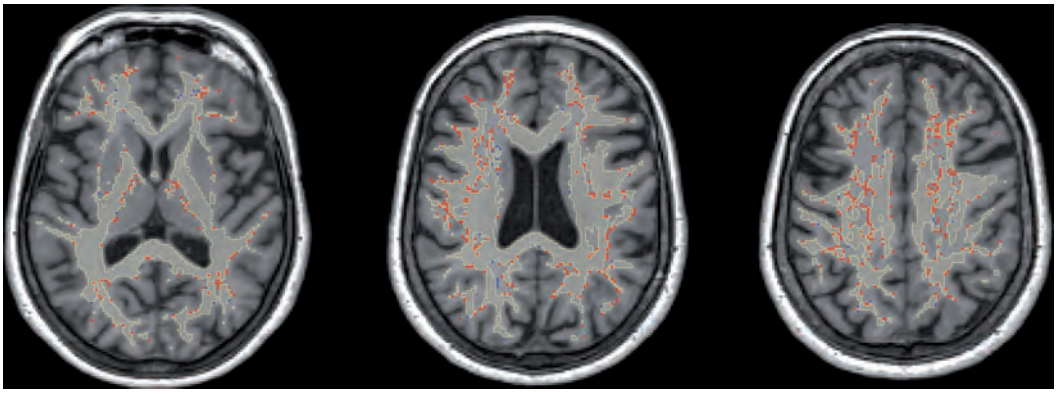

Figure 3.8: Different axial slices of the same patient that illustrate the different WM voxels detected by KLA (red) and by FA (blue).

also very similar, while MA corresponds to the darkest image and KLA to the brightness one. This behavior agrees with the features of their corresponding 3P-plots (see Figure 3.2). For instance, the 3P-plots of FA and AA are practically the same and the same occurs with LA and $AitA$. In this first visual inspection, we note that white and grey matter are discriminated better with FA and KLA measures. In particular, the internal capsule and corpus callosum confluence area are defined more clearly with KLA. These effects are illustrated in a more detailed observation in Figure 3.10, where the FA and KLA maps of the anterior corona radiata and forceps minor, and the maps of the posterior corona radiata are shown. Note that the transition between white and grey matter is represented more clearly with KLA. There is also a better distribution of KLA values that leads to a better distribution of intensity values in the areas with a great confluence of fibers. KLA reaches maximum values in the central regions of the structures while FA decreases in these areas(see Figure 3.9). This better performance is presumably because in these regions (see Figure 3.6) a more 'planar' tensor results. This behavior can be observed in the confluence area between corpus callosum and the anterior corona radiata and also in the posterior corona radiata.

From the data collected in Table 3.3, we can observe that all the anisotropy measures show the same tissue class hierarchy of increasing anisotropy as plotted in Figure 3.7 (a). Observe that KLA takes the higher values, while MA the lower ones, leading to bright and dark images, respectively. From the data of Table 3.3, we compute the CV. The obtained results are plotted in Figure 3.7 (b). Observe that KLA exhibits the lower values, and this indicates a lower dispersion of the measure justifying its capability to reflect better continuity of white matter.

From Table 3.4, we can observe that when comparing GM versus WM tissues (the six first columns of the table) KLA shows the greatest separability in all the cases. On the other hand, when comparing WM versus WM, none of the studied measures stands out from the rest. It can be seen that FA discriminates better between the thalamus

and internal capsule, corpus callosum versus subcortical white matter, and internal capsule versus subcortical white matter. In these three cases, although KLA has a lower detectability, the difference is minimal. In the case of arcuate fascicules versus corpus callosum and internal capsule, MA is the best measure, while RA is the best for separating corpus callosum versus internal capsule. Note that KLA only performs better in the case of arcuate fasciculus versus subcortical white matter. In this case the difference between FA and KLA is very small. From these results, we conclude that FA and KLA have a low performance in structures with a strong tissue organization, such as corpus callosum or arcuate fasciculus, while in the central regions KLA is the measure that performs better.

This behavior can be interpreted from a geometric point of view on a 3P-plot (see Figure 3.5). Note that the distributions of the tissue shape measurements, analogous to Alexander et al. [6], are mostly radial orientations relative to the Cs vertex, revealing that more vertical running isolines facilitate the differentiation of different WM structures, whereas more horizontal running isolines are preferred for separating white and grey matter structures. Therefore, in general, a measure is more sensitive to a change between white and grey matter tissues the more orthogonal to the Cs direction are its isometric contour lines. This coherent behavior appears when we compare the KLA lines against the FA lines in the central regions. Observe that, while the KLA lines reveal departures from isotropy towards either linear or planar anisotropy, FA favors linear anisotropy.

Finally, when evaluating the ability of FA and KLA to discriminate white matter voxels (see Table 3.5), we observe that the mean of voxels detected by KLA is 645.92 while for FA is 32.81. Hence, KLA detects the difference between WM and GM better (see Figure 3.8). This shows that KLA is a good measure for segmenting white matter from grey matter.

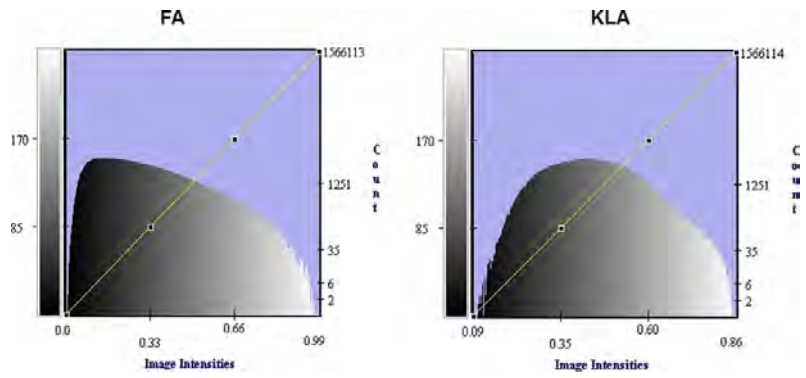

Figure 3.9: Histograms that show the distribution of images intensities of FA and KLA.

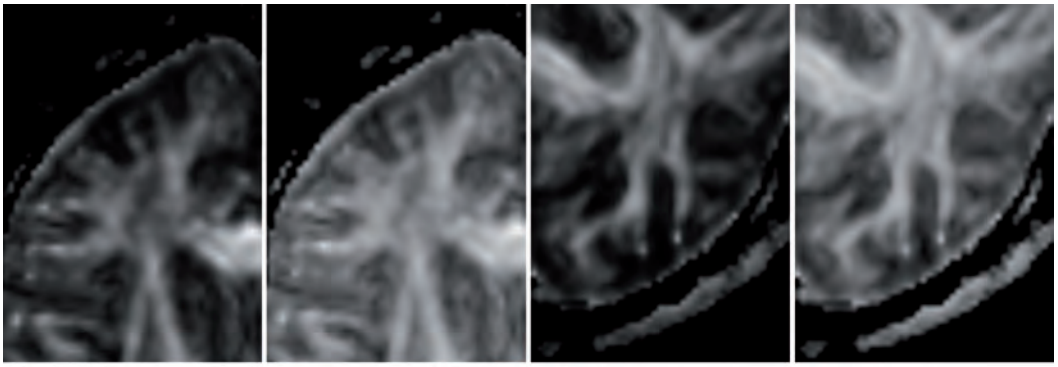

Figure 3.10: *FA* (a) and KLA (b) maps of the anterior corona radiata and forceps minor. *FA* (c) and KLA (d) maps of the posterior corona radiata.

3.7 Conclusions

We have presented a new set of anisotropy measures that can be derived from the DTI data. The evaluation of these measures, with regard to their sensitivity to detect white and grey matter changes on human DTI data, have shown that compositional Kullback-Leibler anisotropy (KLA) and fractional anisotropy (*FA*) have a similar behavior, although KLA detected the transitions between white and grey matter better. The KLA measure also exhibits a lower coefficient of variation with respect to *FA*. This fact reflects a lower dispersion of the measure and hence a better capability to detect white matter continuity. It is also important to note that KLA has a better distribution in areas with greater confluence of fibers. As a future work we will study the possibilities of applying KLA to fiber tracking pipeline and clinical studies.

Chapter 4

Fiber Tracking

Fiber tracking techniques are able to create white matter connectivity maps from DTI data. Fibers are obtained by following the paths of particles dropped in a vector field. The strategy used to approximate these paths is the main difference between the methods analyzed. In this chapter, we analyze the principles and the state of art of the fiber tracking techniques, and we propose a new Monte Carlo-based fiber tracking approach to estimate brain connectivity. One of the main characteristics of our approach is that all parameters of the algorithm are automatically determined at each point using the entropy of the eigenvalues of the diffusion tensor. Experimental results show the good performance of the proposed approach.

4.1 Introduction

The most common technique used to visualize DTI data is the streamline tracking approach, also called *fiber tracking* or *tractography*. This approach considers the directional information encoded in the diffusion tensor to infer patterns of continuity in a tensor field. Since water in white matter diffuses more along 'brain fibers' than perpendicular to it, the fiber tracking technique assumes that the eigenvectors of the diffusion tensor provide a good estimate of the fiber orientation. In this way, the tensor field obtained from DTI data can be reduced to a vector field where only the main eigenvector of each tensor is considered. To create the fiber, the vector field is interpreted as a velocity field, and the tracking technique reconstructs, step by step, the trajectory followed by a particle. The point where the particle is dropped is the seed point, and the criterion that determines when the track finishes is the stopping criterion.

The main drawback of this approach arises when the tensor does not have a strong directional component. In addition, DTI data noise [96] and partial volume effects [7] make the computation of the fiber direction difficult. To overcome all these limitations, more sophisticated fiber tracking techniques such as high angular resolution acquisitions [159], regularization [173], tensor deflection [99], and stochasticity [25] are used.

At the broad level, white matter tractography algorithms can be classified into deterministic and non deterministic. The first only considers the main eigenvector direction to reconstruct the tract and the second introduces some perturbation to modify the vector direction at each location [97, 25, 64, 138]. In this chapter, we focus on non deterministic tracking techniques over single tensor data models. We propose a new tracking technique that uses both a Monte Carlo approach and the entropy of diffusion tensor to obtain the track direction and also the step size. To evaluate the proposed approach we compare it with different tracking techniques using the DTI based human brain atlas from the International Consortium for Brain Mapping (ICBM) database.

This chapter is structured as follows. Section 4.2 surveys background and related work. Section 4.3 proposes a new tracking technique based on the introduction of the entropy of the diffusion tensor to obtain the track direction and the step size. Section 4.4 describes the evaluation framework used to compare the surveyed tracking techniques with the proposed one. Section 4.5 discusses the experimental results. Finally, Section 4.6 presents the conclusions.

4.2 Background and Related Work

In this section we introduce the notation. Then, we describe the main steps of a fiber tracking technique. Finally, we review the main deterministic and non deterministic tracking techniques that have been proposed.

4.2.1 Notation

A fiber path p can be described as a sequence of points $x_n \in V$, where V is a volume in R^3. Tracking algorithms determine how to obtain the sequence of points x_n, being x_0 the starting point of a fiber path. The eigenvectors of tensor $D(x_n)$ are denoted by $e_i(D(x_n))$, where e_1 is the main eigenvector. We will refer to the eigenvalues of tensor $D(x_i)$ as λ_1, λ_2, and λ_3, where $\lambda_1 \geq \lambda_2 \geq \lambda_3$. A normalized vector $\frac{\vec{v}}{\|v\|}$ is denoted by $\overline{v}$. The normalized direction of the starting point is $\vec{v}_0 = \overline{e_1(D(x_0))}$, then $x_{n+1} = x_n + \mu\vec{v}_n$, where $\vec{v}_n$ is the normalized propagation direction and μ is the step size. The incoming vector direction is denoted as $\vec{v}_{n-1}$. The exponent k is used to power the diffusion tensor matrix $D(x_n)^k$.

Non deterministic or stochastic fiber tracking techniques introduce randomness in the deterministic tractography. In these algorithms, ε_n is an independent standard normal random vector, r_n is a random vector uniformly distributed over a unit sphere, and σ is the intensity of artificial noise that is added to generate stochastic tracks.

4.2.2 Main Steps of Fiber Tracking Techniques

Several techniques have been proposed to define fiber trajectories in a diffusion tensor field. Most of them reduce tensor data to a vector field and define a fiber path. These algorithms are based on solving the next equation:

$$p = \int_0^m e_1(D(x_n))dx \tag{4.1}$$

where $p(x_0)$ and $p(x_m)$ are, respectively, the initial and the ending point of the fiber path.

Despite the differences between methods, three main steps are required to solve this equation.

1. **Definition of seeds.** To start the tracking process, we have to define the number and the position of the seeds in the voxels. Basically, two alternatives can be considered. The first strategy places seeds in all the voxels of the model. This guarantees the reconstruction of all the structures, but it is computationally expensive and leads to cluttered images (Figure 4.1). The second strategy defines regions or volumes of interest and only places seeds in the voxels contained in these regions. In this case, the approach is completely dependent of the user's anatomical knowledge and for this reason the reproducibility is reduced.

2. **Selection of an integration strategy.** Fiber trajectories can be generated by integrating Equation 4.1 with the initial conditions given by specified seed positions. Different integration methods can be applied. The difference between them stem from the methodology of calculating the propagation direction $\vec{v}_n$ and the step size μ. The most applied strategies are:

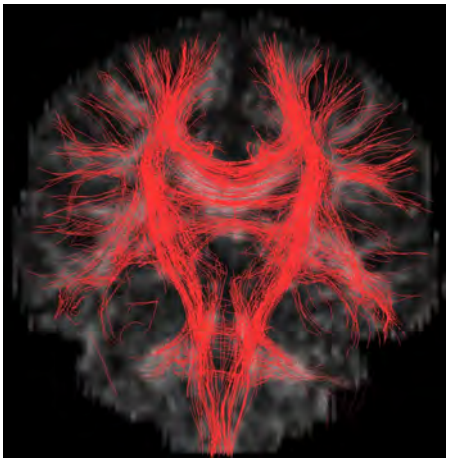

Figure 4.1: Illustration of whole brain fiber tracking. In this example it is difficult to interpret anatomic areas.

- Euler integration method, that calculates the new position x_{n+1} by stepping along a direction $\vec{v}_n$ for a step size μ and from a position x_n. Euler integration method is defined as

$$x_{n+1} = x_n + \mu\vec{v}_n. \tag{4.2}$$

- Runge-Kutta of fourth order ($RK4$) integration method which requires four evaluations of the propagation direction: one at the beginning, two at the midpoint, and one at the end of the step. The positions of the midpoint and the end of the step are approximated by taking several trial steps. The next fiber point x_{n+1} is a weighted combination of the four estimated vectors added to x_n:

$$\vec{k}_1 = \mu\vec{v}_n, \tag{4.3}$$

$$\vec{k}_2 = \mu e_1(D(x_n + \frac{1}{2}\vec{k}_1)), \tag{4.4}$$

$$\vec{k}_3 = \mu e_1(D(x_n + \frac{1}{2}\vec{k}_2)), \tag{4.5}$$

$$\vec{k}_4 = \mu e_1(D(x_n + \vec{k}_3)), \tag{4.6}$$

where $\vec{v}_n$ is the propagation direction calculated using a fiber tracking technique. Then, x_{n+1} is defined as

$$x_{n+1} = x_n + \frac{\vec{k}_1}{6} + \frac{\vec{k}_2}{3} + \frac{\vec{k}_3}{3} + \frac{\vec{k}_4}{6}. \tag{4.7}$$

Detailed descriptions and implementations of $RK4$ method can be found in the literature [137, 29, 110].

- Fiber Assignment by Continuous Tracking (*FACT*) is an approach introduced by Mori et al. [116] and uses as propagation direction the value of $\vec{v}_n$ obtained from the current voxel, and no interpolation is performed. The step size varies from step to step according to the distance between the boundaries of the voxel at the entry and exit points. As a result, the trajectory will be formed by a series of segments of variable length. This integration method has a high computational efficiency. Fiber tract point x_{n+1} is defined as

$$x_{n+1} = x_n + s\vec{v}_n, \tag{4.8}$$

  where x_n is the first point where the fiber intersects the voxel, and x_{n+1} is the intersection point where the fiber path leaves the current voxel and enters the next, and s represents the length of the segment connecting both intersection points.

3. **Definition of stopping criteria.** The stopping criteria determine when the tracking process has to finish. The stopping criteria are user-defined and are based on, amongst others, anisotropy indices (for instance, $FA < 0.2$ [118]) and fiber curvature (for instance, the radius of curvature of the tract is smaller than approximately two voxels [18]).

To represent the tracking more accurately, the algorithm can be combined with the definition of regions or volumes of interest that determine which fibers have to be represented.

4.2.3 Classification of The Fiber Tracking Techniques

The main difference between fiber tracking techniques is on the strategy applied to determine how to obtain the different points that define the tract once seeds are placed and the stop criteria have been defined.

In this section, we review some of the tracking techniques that have been proposed. We have grouped them into two different groups, deterministic and non deterministic techniques.

4.2.3.1 Deterministic Algorithms

Deterministic algorithms were the first fiber tracking algorithms to appear. These algorithms use a linear propagation approach where fiber trajectories are generated in a stepwise fashion deriving the direction of each step from the local diffusion tensor [39, 116, 170, 18]. The most representative approaches of this category are:

- The streamline approach proposed by Contouro et al. [39], which generates fibers following the direction of faster diffusion, i.e., the main eigenvector. The propagation direction is described by

$$\vec{v}_n = e_1(D(x_n)). \tag{4.9}$$

The main drawback of this approach appears in areas of nonlinear diffusion, such as planar regions, since the trace of the fiber cannot be determined due to partial volume effects, such as crossing, kissing, and branching (see Section 2.4.2). Different strategies have been proposed to approximate paths in these configurations [163, 184].

- The tensor deflection approach [170, 99, 96] was proposed in order to improve propagation in regions with low anisotropy, such as crossing fiber regions, where the direction of fastest diffusivity is not well defined [172]. The idea is to use the entire D to deflect the incoming vector direction $\vec{v}_{n-1}$ and to obtain a smoother tract reconstruction result. Thus, the current direction $\vec{v}_n$ is given as

$$\vec{v}_n = D(x_n)\vec{v}_{n-1}. \tag{4.10}$$

- The tensorline propagation method proposed by Weinstein et al. [170] incorporates information about the voxel orientation, as well as the anisotropic classification of the local tensor [172] given by Cl, Cp, and Cs indices (see Section 2.3.2). Tensorline propagation direction is a combination of the previous direction (main eigenvector) and the tensor deflection direction. The $\vec{v}_n$ direction is given as

$$\vec{v}_n = Cl\ e_1(D(x_n)) + (1 - Cl)\left((1 - w_{punct})\vec{v}_{n-1} + w_{punct}\frac{D(x_n)}{\lambda_1}\vec{v}_{n-1}\right), \tag{4.11}$$

where w_{punct} is a user-controlled parameter that takes values from 0 to 1, and affects to what extent the propagation should be encouraged to 'puncture' through planar tensors oriented normal to its path, versus turning into the plane.

4.2.3.2 Non Deterministic Algorithms

Non-deterministic fiber tracking techniques [25, 97, 64, 138] aim at overcoming the shortcomings of deterministic methods by adding some randomness to the deterministic tractography. They simulate a macroscopic random walk of a particle through the set of voxels. This random walk is defined by one-to-one jumps where the step of the jump and its direction is determined by the parameters of the algorithm. These techniques can be applied directly or combined with probability maps. These probability algorithms trace different paths and calculate a spatial probability distribution of connectivity for each seed point [90, 129, 22, 20]. It is considered that the final tracking is the most probable. Some non deterministic algorithms are described below.

- The white matter tractography using a random vector perturbation algorithm (RAVE) proposed by Lazar et al. [97], generates multiple fiber pathways by perturbing the major eigenvector according to the tensor shape. For instance, if

the major eigenvector is oriented along x axis, the new propagation direction is defined by randomly generating y and z offsets. To generate these random offsets, perturbation functions such as standard deviation, which can be weighted by a proportionality factor α, can be used. Given $v_n = (x, y, z)$, the propagation direction is obtained as follows:

$$\vec{v}_{n+1} = \begin{cases} (x, \alpha\sqrt{\frac{y}{x}}, \alpha\sqrt{\frac{z}{x}}), \text{if } x > y \text{ and } x > z \\ (\alpha\sqrt{\frac{x}{y}}, y, \alpha\sqrt{\frac{z}{y}}), \text{if } y > x \text{ and } y > z \\ (\alpha\sqrt{\frac{x}{z}}, \alpha\sqrt{\frac{y}{z}}, z), \text{if } z > x \text{ and } z > y \end{cases} \tag{4.12}$$

- The method, proposed by Björnemo et al. [25], uses sequential importance sampling and resampling to sequentially build up a set of weighted samples representing all possible fiber paths originating from a starting point x_0. Connectivity is derived from these weighted samples. This method introduces the parameters α and σ to vary the influence of the regularization of direction and to control the stochasticity, respectively. The algorithm is given as

$$\overline{D(x_n)} = \frac{D(x_n)}{\lambda_1}, \tag{4.13}$$

$$D_{reg}(x_n) = \overline{D(x_n)} + \alpha\vec{v}_{n-1}\vec{v}_{n-1}^T, \tag{4.14}$$

$$\delta_n = D_{reg}(x_n)r_n - (D_{reg}(x_n)r_n e_1(D_{reg}(x_n)))e_1(D_{reg}(x_n))^T, \text{ and} \tag{4.15}$$

$$\vec{v}_n = e_1(D_{reg}(x_n)) + \overline{\delta_n}\sigma. \tag{4.16}$$

- Hagmann et al. [64] propose a hybrid approach combining Monte-Carlo random walk simulation with information about the white fiber track curvature function. This method considers that in each voxel the probability of a fiber to be propagated in a given direction is proportional to the corresponding diffusion coefficient. It also assumes that axonal trajectories, or more cautious trajectories of axonal bundles, follow regular curves. They make use of all of the available diffusion information in order to explore many potential connections and select an appropriate tract by measuring a posteriori the mean diffusion along the trajectory. The propagation direction is obtained by

$$\vec{v}_n = \frac{\sigma d_n + \vec{v}_{n-1}}{\|\sigma d_n + \vec{v}_{n-1}\|}, \quad (\vec{v}_{n-1} \cdot \vec{v}_n) > 0 \tag{4.17}$$

where

$$d_n = D(x_n)^k r_n, \tag{4.18}$$

and σ can take values from 0 to 1 and is a constant tuning the relative importance of the random diffusion component versus the curve regularizing term.

- Prigarin et al. [138] propose three different tracking algorithms.

  The first one, denoted E extends the streamline approach by the addition of random perturbations directly to the integration method. The following equations are used to obtain $\vec{v}_n$ and x_{n+1}:

$$\vec{v}_n = e_1(D(x_n)), \quad (\vec{v}_{n-1} \cdot \vec{v}_n) > 0, \text{ and} \tag{4.19}$$

$$x_{n+1} = x_n + \mu\vec{v}_{n-1} + \sqrt{\mu}\sigma\varepsilon_n, \tag{4.20}$$

  where ε_n is an independent standard normal random vector, and μ and σ are parameters of the algorithm. The step parameter μ is assumed to be less than 1. For this algorithm, the parameter σ defines the intensity of artificial noise that is added to generate stochastic tracks. If $\sigma = 0$, then the algorithms become deterministic and the tracks are defined in a unique non-random way.

  The second algorithm, denoted T1, in some aspects is similar to the tensor deflection approach proposed by Lazar et al. [99] with the addition of random perturbations. In this case, the computation of fiber tracks is done by applying the following equations:

$$\vec{v}_n = D(x_n)^k\vec{v}_n, \text{ and} \tag{4.21}$$

$$x_{n+1} = x_n + \mu\vec{v}_n + \sqrt{\mu}\sigma\varepsilon_n. \tag{4.22}$$

  When $k > 1$, the influence of the main eigenvector onto the track increases and therefore this direction may be more relevant than the other directions of the tensor.

  The third algorithm, denoted T2, considers not only the principal eigenvectors but the whole tensor. In this case, the computation of fiber tracks is done by applying the following equations:

$$\vec{v}_0 = c_0\frac{e_1(D(x_0))}{\|e_1(D(x_0))\|}, \quad a_0 = 0, \tag{4.23}$$

$$a_{n+1} = \frac{D(x_n)^k\vec{v}_{n-1}}{\|D(x_n)^k\vec{v}_{n-1}\|} - c_1\vec{v}_{n-1}, \text{ and} \tag{4.24}$$

$$\vec{v}_n = \vec{v}_{n-1} + \mu a_{n+1} + \sqrt{\mu}\sigma\varepsilon_{n+1}. \tag{4.25}$$

  For the T2 algorithm, the Euler integration method can be used to calculate x_{n+1}.

  If we compare E, T1, and T2 algorithms, it can be seen that since the E method follows the directions of principal eigenvectors, this can be unstable under noisy fluctuations of the elements of the tensor (especially, when some eigenvalues are close to each other) or they can be simply undefined in case of multiple eigenvalues. T1 and T2 algorithms overcome these limitations taking into account the directions of principal eigenvectors and also other information from the tensor

field. Moreover, the T1 algorithm generates smoother and more stable tracks than the E algorithm. Note that in all the algorithms the values of $\vec{v}_n$ can be interpreted as the velocity of a particle, and for the T2 algorithm the values of a_n can be interpreted as the acceleration of a particle.

To conclude this section, in Table 4.1, we summarize the main features of each of the related methods. From left to right, in each column, we represent: the name of the method, the required parameters, the initialization of the propagation direction, the equation used to calculate the next fiber point, and the equations to calculate the propagation direction.

4.3 Entropy-Based Method

In this section, we propose a new Monte Carlo approach to estimate the fiber tracks. This method is based on the introduction of the entropy of the diffusion tensor to obtain the track direction and the step size. The main characteristic of this method is that it is completely automatic. The degree of randomness introduced in the track direction computation and the step size depends on the Shannon entropy of the eigenvalues of the diffusion tensor.

As we have seen in Section 2.5.1, the *Shannon entropy* $H(X)$ of a discrete random variable X with values in the set $\mathcal{X} = \{x_1, x_2, \ldots, x_n\}$ is defined as

$$H(X) = -\sum_{x \in \mathcal{X}} p(x) \ln p(x), \tag{4.26}$$

where $p(x) = Pr[X = x]$. The logarithms are now taken in base e and entropy is expressed in nats. The Shannon entropy $H(X)$, also denoted by $H(p)$, measures the average uncertainty of random variable X [43]. For more details see Section 2.5.

4.3.1 Algorithm Description

Our algorithm takes into account the diffusion uncertainty within a voxel to calculate the position of the next point of the fiber path. This uncertainty is proportional to Shannon entropy of the eigenvalues of the diffusion tensor. Taking into account this consideration, we establish the basis of our approach as follows:

- First, randomness is added to previous $\vec{v}_{n-1}$ using the Shannon entropy (see Equation 4.26). If uncertainty is large, the track can probably take a bigger deviation and vice versa.
- Second, the resulting vector $\vec{v}_n$ is multiplied by the diffusion tensor and, hence, the tensor deflects the perturbed propagation direction towards the major eigenvector direction while limiting the curvature of the deflection, resulting in smoother tract reconstruction [96].
- Third, the step size μ_n is small if the uncertainty is large, and vice versa.

Method	**Parameters**	$\vec{v}_0$	x_{n+1}	$\vec{v}_n$
Streamline [39]	$<\mu>$	$\overline{e_1(D(x_0))}$	$x_n+\mu\vec{v}_n$	$e_1(D(x_n))$
Deflection [99, 96]	$<\mu>$	$\overline{e_1(D(x_0))}$	$x_n+\mu\vec{v}_n$	$D(x_n)v_{n-1}$
Tensorline [170]	$<\mu, w_{punct}>$	$\overline{e_1(D(x_0))}$	$x_n+\mu\vec{v}_n$	$Cl\ e_1(D(x_n))+(1-Cl)\left((1-w_{punct})\vec{v}_{n-1}+w_{punct}\frac{D(x_n)}{\lambda_1}\vec{v}_{n-1}\right)$
Streamline using RK4 [110]	$<\mu>$	$\overline{e_1(D(x_0))}$	$x_n+\frac{\vec{k}_1}{6}+\frac{\vec{k}_2}{3}+\frac{\vec{k}_3}{3}+\frac{\vec{k}_4}{6}$	$\vec{k}_1=\mu e_1(D(x_n))$, $\vec{k}_2=\mu e_1(D(x_n+\frac{1}{2}\vec{k}_1))$, $\vec{k}_3=\mu e_1(D(x_n+\frac{1}{2}\vec{k}_2))$, $\vec{k}_4=\mu e_1(D(x_n+\vec{k}_3))$
Streamline using FACT [116]		$\overline{e_1(D(x_0))}$	$x_n+s\vec{v}_n$	$e_1(D(x_n))$
Deflection using FACT [98]		$\overline{e_1(D(x_0))}$	$x_n+s\vec{v}_n$	$D(x_n)v_{n-1}$
RAVE [97]	$<\mu,\alpha>$	$\overline{e_1(D(x_0))}$	$x_n+\mu\vec{v}_n$	$(x,\alpha\sqrt{\frac{y}{x}},\alpha\sqrt{\frac{z}{x}})$, $x>y$ and $x>z$ $(\alpha\sqrt{\frac{x}{y}},y,\alpha\sqrt{\frac{z}{y}})$, $y>x$ and $y>z$ $(\alpha\sqrt{\frac{x}{z}},\alpha\sqrt{\frac{y}{z}},z)$, $z>y$ and $z>x$
Björnemo et al. [25]	$<\mu,\alpha,\sigma>$	$\overline{e_1(D(x_0))}$	$x_n+\mu\vec{v}_n$	$e_1(D_{reg}(x_n))+\overline{\delta_n}\sigma$, $\delta_n=D_{reg}(x_n)r_n-(D_{reg}(x_n)r_n e_1(D_{reg}(x_n)))e_1(D_{reg}(x_n))^T$ $D_{reg}(x_n)=\overline{D(x_n)}+\alpha\vec{v}_{n-1}\vec{v}_{n-1}^T$ $\overline{D(x_n)}=\frac{D(x_n)}{\lambda_1}$
Hagmann [64]	$<\mu,\sigma,k>$	$\overline{e_1(D(x_0))}$	$x_n+\mu\vec{v}_n$	$\sigma d_n+\vec{v}_{n-1},(\vec{v}_{n-1}\cdot\vec{v}_n)>0$ $d_n=D(x_n)^k r_n$
Prigarin E [138]	$<\mu,\sigma>$	$\overline{e_1(D(x_0))}$	$x_n+\mu\vec{v}_n+\sqrt{\mu}\sigma\varepsilon_n$	$e_1(D(x_n)),(\vec{v}_{n-1}\cdot\vec{v}_n)>0$
Prigarin T1 [138]	$<\mu,\sigma,k>$	$\overline{e_1(D(x_0))}$	$x_n+\mu\vec{v}_n+\sqrt{\mu}\sigma\varepsilon_n$	$D(x_n)^k\vec{v}_{n-1}$
Prigarin T2 [138]	$<\mu,\sigma,k,c_0,c_1>$	$c_0\overline{e_1(D(x_0))}$; $a_0=0$	$x_n+\mu\vec{v}_n$	$\vec{v}_{n-1}+\mu a_{n+1}+\sqrt{\mu}\sigma\varepsilon_n$, $a_{n+1}=\overline{D(x_{n-1})^k\vec{v}_{n-1}}-c_1\vec{v}_{n-1}$

Table 4.1: From left to right, the columns represent, respectively, the name of the method, the required parameters, the initialization of propagation direction, the equation used to calculate the next fiber point, and the equations to calculate the propagation direction. $D(x)$ is the diffusion matrix at x, e_1 is the main eigenvector, r_n is a random vector uniformly distributed over a unit sphere, μ is the step size, ε_n is an independent standard normal random vector and σ is the intensity of artificial noise.

Considering these three assumptions, the proposed approach is described as follows. From the starting point x_0, the next position $x_n + 1$ is computed as:

$$x_{n+1} = x_n + \mu_n \vec{v}_n, \tag{4.27}$$

where the normalized direction $\vec{v}_n$ is given by

$$\vec{v}_n = D(x_n)(\vec{v}_{n-1} + \delta_n r_n) \tag{4.28}$$

and the initial direction $\vec{v}_0$ is taken as

$$\vec{v}_0 = \overline{e_1(D(x_0))}. \tag{4.29}$$

A random vector $\delta_n r_n$ is computed using

$$\delta_n = c\overline{H(x_n)}, \tag{4.30}$$

where c is a constant and $\overline{H(x_n)}$ is the normalized Shannon entropy of the eigenvalues, which is given by

$$\overline{H(x_n)} = \frac{H(x_n)}{\ln 3}, \tag{4.31}$$

where

$$H(x_n) = -\sum_{i=1}^{3} \rho_i(x_n) \ln \rho_i(x_n) \tag{4.32}$$

is the Shannon entropy of the normalized eigenvalues

$$\rho_i(x_n) = \frac{\lambda_{i_n}}{\lambda_{1_n} + \lambda_{2_n} + \lambda_{3_n}}. \tag{4.33}$$

The maximum value of the Shannon entropy is $\ln 3$ and is obtained when the eigenvalues are equal. In this case, we have the maximum uncertainty in the path direction. On the contrary, the entropy is minimum when two eigenvalues are zero. In this case, there is no uncertainty in the track direction.

Finally, the step size μ_n is given by

$$\mu_n = 1 - \overline{H(x_n)}. \tag{4.34}$$

Observe that the maximum step size will be obtained with the minimum entropy, i.e., the minimum uncertainty in the path direction. Therefore, an increase in uncertainty will lead to a step size decrease.

To properly adjust the parameter c of our method, we place seeds in different well-known anatomical structures of the brain and then we apply the method with c ranging from 0.1 to 0.4. The obtained results were evaluated by an expert anatomist to determine the best one. In all the tests, the selected track corresponds to values ranging from 0.2 to 0.3. In our experiments, we propose to use 0.2 as c value.

In Figure 4.2, the results obtained when a seed is placed in the genus of the corpus callosum, with c values from 0.1 to 0.4, are shown. Obtained tracks are compared

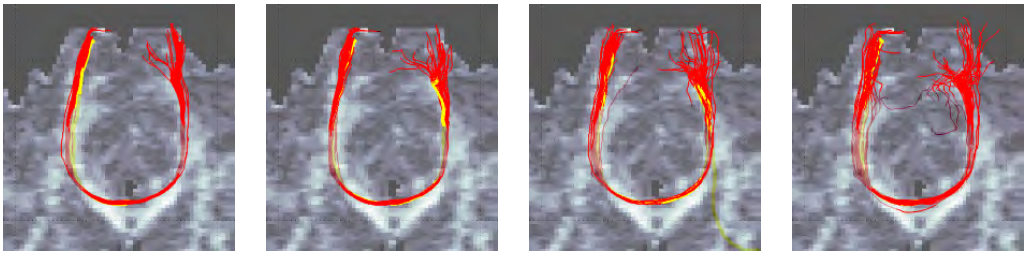

c=0.1 c=0.2 c=0.3 c=0.4

Figure 4.2: Results obtained with the proposed fiber tracking methods taking a seed in the middle of the genus of the corpus callosum and considering different c values. The yellow track has been obtained by a deterministic approach.

with the deterministic track (in yellow). Observe how the dispersion of the fiber paths increases with c.

To evaluate the performance of the proposed approach, and compare it with other reported methods, we considered different validation strategies. In the next section, we summarize some of them.

4.4 Validation of Fiber Tracking Techniques

Fiber tracking can provide valuable and important information for clinical diagnosis. However, it is difficult to guarantee the correctness of the techniques and this makes its application in real environments difficult [33]. With the aim of evaluating fiber tracking techniques, different validation frameworks and techniques have been proposed. These can be grouped into four different groups:

- *Simulated phantoms*, which reproduce common anatomical structures or complex configurations such as crossing, kissing, and branching patterns [5, 98, 59, 44, 30]. In general, simulated phantoms are created by designing the true trajectory, choosing the sample orientation, assuming a diffusion profile, simulating a diffusion-weighted signal, adding noise, and finally reconstructing the simulated track.

- *Physical phantoms*, which are constructed from real synthetic fibers such as rayon, cotton, and nylon [145, 133, 135, 50]. With the physical phantoms, we add an extra layer of realism into the model at the expense of a degree of control over the ground truth.

- *In vivo and in vitro*, are techniques that are based on the comparison of tractography results with models obtained from the classical dissection of post-mortem brain tissue or with histological tracer studies to validate fiber tracking techniques [49, 95, 10, 106].

- *Circumstantial validation*, are frameworks that use the results of functional imaging methods as complementary information that assists in the validation process [60, 82, 130, 152]. The functional brain regions not only serve as a seed site for the fiber tracks, but also test the reliability of the tracks by proposing termination sites.

From all these strategies, we selected *in vivo and in vitro* techniques. In particular, we used the DTI based human brain atlas from the International Consortium for Brain Mapping (ICBM) database. This atlas is based on probabilistic tensor maps obtained from 81 subjects acquired under an initiative of the ICBM. The subjects were healthy right-handed adults ranging from 18 to 59 years of age. A hand-segmented white matter parcellation map was created from this averaged map. This map can be used for automated white matter parcellation. The precision of the affine-based image normalization and automated parcellation was measured for a group of healthy subjects using manually defined anatomical landmarks. For the tests, we have considered the parcellation provided by this second atlas.

4.5 Results

In this section, we present the different tests that have been carried out to evaluate the proposed approach. To carry out the experiments, we have implemented reported methods and we have integrated them in a common visualization platform, see Chapter 6. In Table 4.2 we report the parameters used for each of the tested methods. From left to right in each column, we represent, the name of the method, the step size and other parameters required by the method. To evaluate our approach we considered two different c values, $c = 0.2$ and $c = 0$. This last is the deterministic version of the method. The definition of the seeding points and the stopping criteria depend on the experiment.

All tests have been done on the DTI based human brain atlas. To carry out the experiment, we have selected four VOIs corresponding to the corticospinal tract, the arcuate fasciculus, the body of corpus callosum, and the fornix (see Figures 4.3 and 4.4). These VOIs have been obtained from a hand-segmented white matter parcellation map that was created from the DTI based human brain atlas.

For all the methods, to generate tracts, we have set a start criterion that uses $FA > 0.3$, a stopping criterion $FA < 0.1$, and angle $< 100^o$. In the case of the methods using FACT, the stopping criterion does not consider angle restrictions. Seeds have only been placed inside the VOIs provided with the atlas data. Four significant bundles of fibers, such as the corticospinal tract, the arcuate fasciculus, the body of corpus callosum, and the fornix have been reconstructed. Intersection ROIs have been defined for each evaluated structure as in Catani et al. [32]. We have applied each of the evaluated methods to reconstruct the structures. The obtained results (see Figures 4.6-4.11) have been evaluated by an expert anatomist.

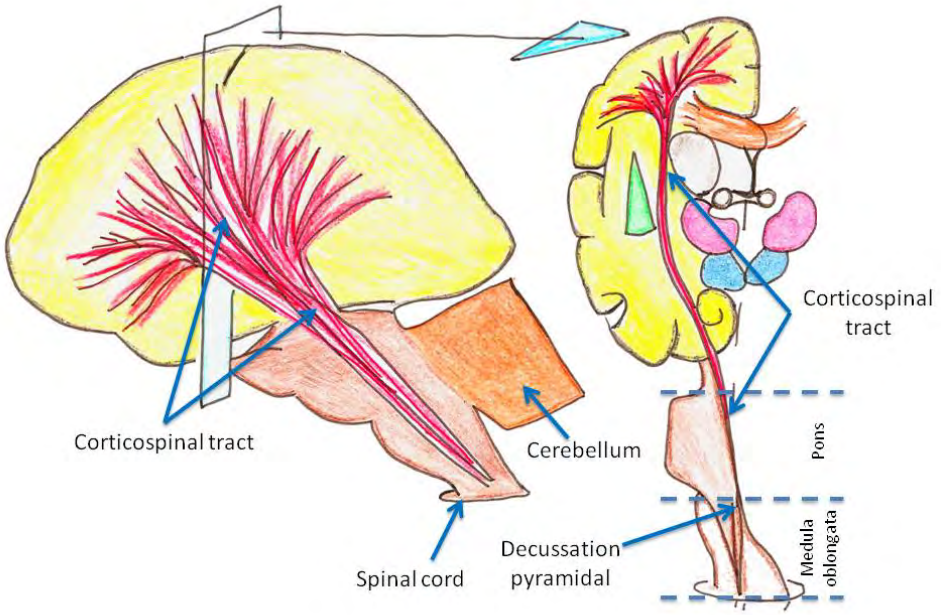

Corticospinal tract

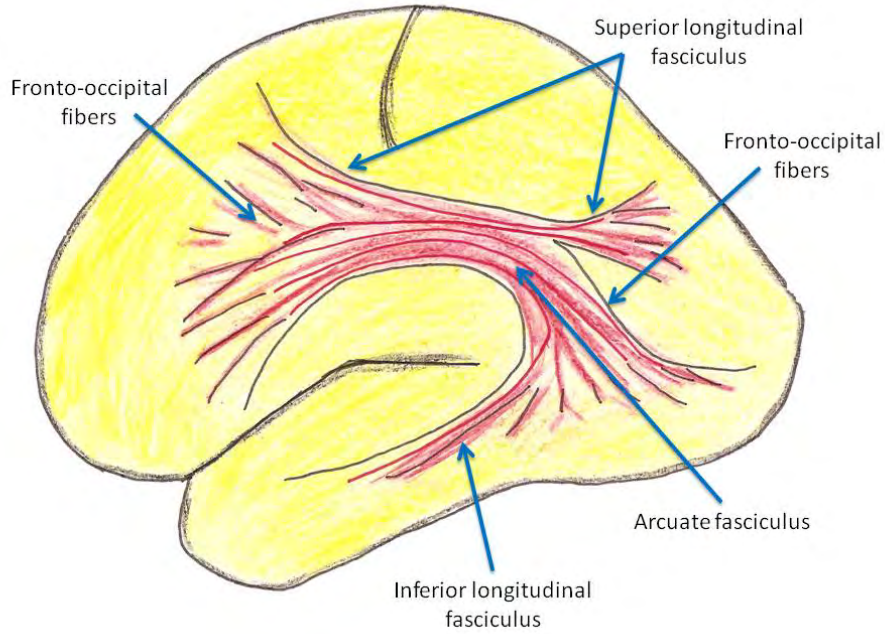

Arcuate fasciculus

Figure 4.3: Schematic representation of the corticospinal tract and the arcuate fasciculus.

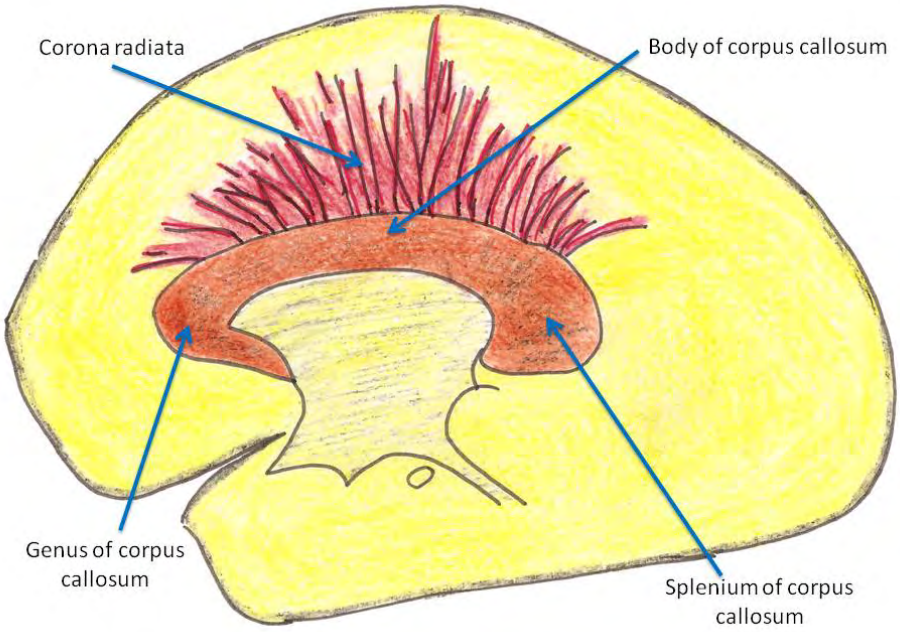

Body of corpus callosum

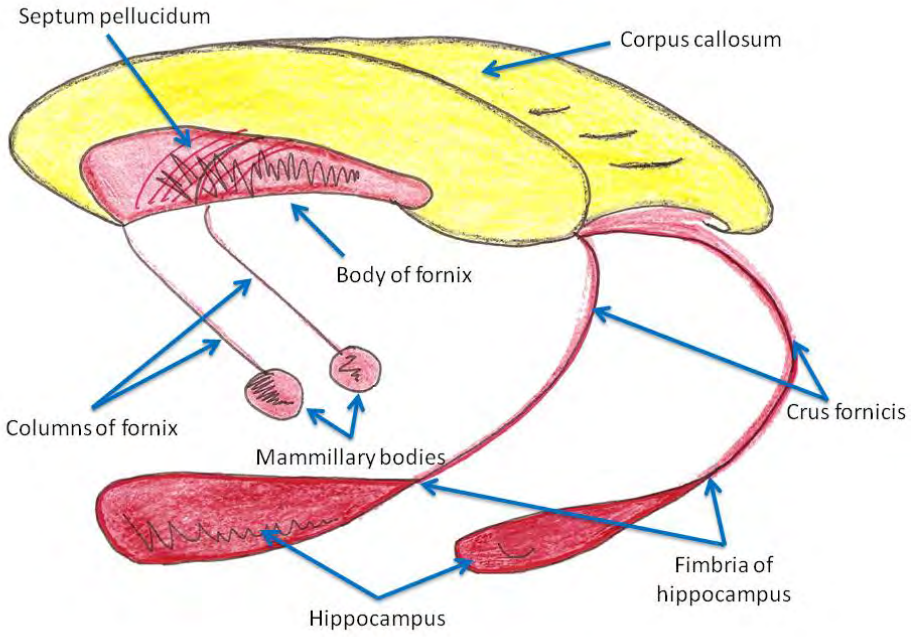

Fornix

Figure 4.4: Schematic representation of the body of corpus callosum and the fornix.

Method	Step size (μ)	Other parameters
Entropy-based ($c = 0.2$)	Adaptive	$c = 0.2$
Entropy-based ($c = 0$)	Adaptive	$c = 0$
Streamline	0.5	
Tensor deflection	0.5	
Tensorline	1.0	$w_{punct} = 0.2$
Prigarin E	0.1	$\sigma = 0.2$
Prigarin T1	0.1	$\sigma = 0.2$, $k = 2$
Prigarin T2	0.1	$\sigma = 0.2$, $k = 2$, $c_0 = 1$, $c_1 = 1$
Hagmann	0.75	$\sigma = 0.1$, $\alpha = 2$
Streamline + RK4	Adaptive [110]	
Streamline + FACT	Adaptive [96]	
Tensor deflection + FACT	Adaptive [96]	

Table 4.2: The evaluated fiber tracking techniques with their corresponding parameters. From left to right in each column, we represent the name of the method, the step size, and other parameters required by the method.

The first evidence, and also difference between methods, is observable at the bottom of the corticospinal tract (see Figures 4.6 and 4.7). In this part, *Streamline with FACT* and *Tensor deflection with FACT* have less numbers of fibers. The same situation can be seen at the top of the corticospinal tract. Other important characteristic can be observed with the non deterministic algorithms. In the coronal view of the corticospinal tract, a greater openness of the endings of the fibers can be seen (see Figure 4.7). Such terminations are desired for such structures, even if it is expected that some fibers cover all corona radiata, and consequently need be 'more open ended'. In the sagittal view of the corticospinal tract, it can be observed that *Prigarin T1*, *Prigarin T2* and *Hagmann* obtain a compact result of the superior part of the corticospinal tract. This effect is due to an increase in the exponent k of the power of the tensor since the smoothing effect in long fibers also contributes to greater compaction. In Figure 4.5, we illustrate the influence of k in the shape of the ellipsoid that represents the tensor matrix. Observe that by increasing k, the shape of the ellipsoid becomes more planar. We test values between 1 and 4.

Arcuate fasciculus is a fiber bundle that is very difficult to reconstruct due to its curvature (see Figure 4.8). The connectivity of this structure has been analyzed by Bernal et al. [24] and their reconstructions are similar to the ones obtained by the *Entropy-based* algorithm with $c = 0.2$ and $c = 0$, and *Streamline with Runge Kutta 4*. For this structure, methods *Entropy-based* ($c = 0$), *Streamline*, *Tensor deflection*, and *Streamline with Runge Kutta 4* obtain optimal reconstructions with a few erratic fibers, all in the frontal part. Observe that the best reconstruction is achieved by *Entropy-based* with $c = 0.2$. *Streamline with FACT* and *Tensor deflection with FACT* show bad results due to each step crossing the entire voxel. This demonstrates that FACT approaches have serious difficulties turning.

In the body of the corpus callosum, as expected, all methods have been able to

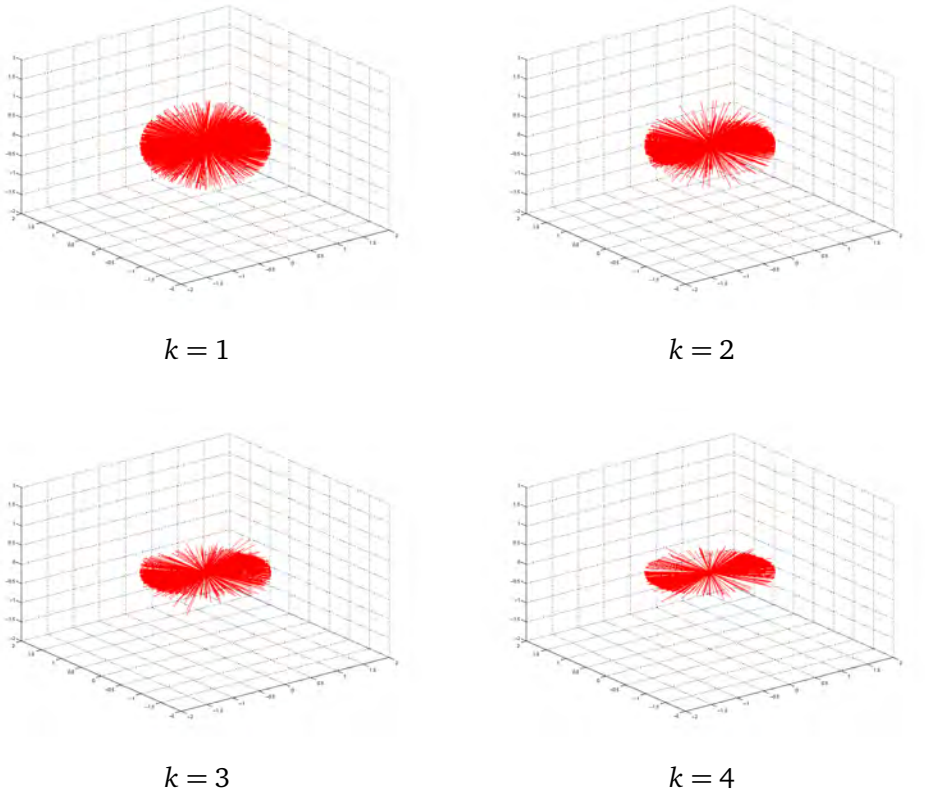

$k = 1$ $k = 2$

$k = 3$ $k = 4$

Figure 4.5: From left to right and top to bottom tensor/ellipsoid deformation increasing the k factor with values of 1, 2, 3 and 4 in each image.

successfully reconstruct the U-shape callosal fiber (see Figures 4.9 and 4.10). The most interesting results are obtained by *Entropy-based* method with $c = 0.2$. This method has been the only technique able to reconstruct the longer projection fibers that cross a high planar region like the corona radiata. This is thanks to the adaptive step size and randomness, both weighted by entropy. The detection of the lateral projections of the corpus callosum is one of the main limitations of the fiber tracking techniques over simple tensor data [165, 69].

In Figure 4.11, the obtained reconstructions of the fornix are shown. In comparison with the structures of fornix described by Concha et al. [38] and Wakana et al. [165], *Entropy-based* ($c = 0.2$) perfectly detects the columns and the body of fornix, and partially the crus of fornix. In fact, the body of fornix has been detected by all the methods, but columns and crus of fornix have obtained different results depending on the techniques. *Streamline with FACT*, *Tensor deflection with FACT*, and *Hagmann* do not detect the columns of fornix. In the reconstruction of the crus of fornix, *Tensorline*, *Prigarin T2*, and *Hagmann* obtain erratic fibers that draw the corpus callosum due to the proximity of the two structures.

In the atlas-based model, the effect of adaptive step is difficult to analyze. A big adaptive step size has problems turning, as we can see in the *Streamline with FACT* and *Tensor deflection with FACT* methods. On the other hand, a lower adaptive step size, as in *Entropy-based* ($c = 0.2$), *Entropy-based* ($c = 0$) and *Streamline with Runge Kutta 4*, gets excellent results in the reconstruction of all structures.

In conclusion, the deflection, the adaptive step size, and the randomness have demonstrated a good performance over the atlas-based DTI data. Deflection, in combination with adaptive step size, have allowed us to reconstruct in a better way the curve of arcuate fasciculus. The adaptive step size mixed with randomness has been a good choice in deciding the paths to follow. *Entropy-based* ($c = 0.2$) is the algorithm that uses all of them. We must also consider the good quality and resolution of the data model, which has allowed us to develop the algorithms in an ideal situation. In this ideal situation, *Entropy-based* ($c = 0.2$) has shown to behave in a very good way to rebuild the selected fiber bundles. Other methods such as *Entropy-based* ($c = 0$), *Tensor deflection*, *Tensorline*, and *Streamline with Runge Kutta 4*, have obtained good results too.

4.6 Conclusions

In this chapter, we have described main fiber tracking techniques, and presented a new stochastic approach for fiber tracking based on the introduction of the Shannon entropy of the eigenvalues of the diffusion tensor to obtain the track direction and the step size. One of the main characteristics of this approach is that all parameters of the algorithm are automatically determined at each point using the entropy of the eigenvalues of the diffusion tensor.

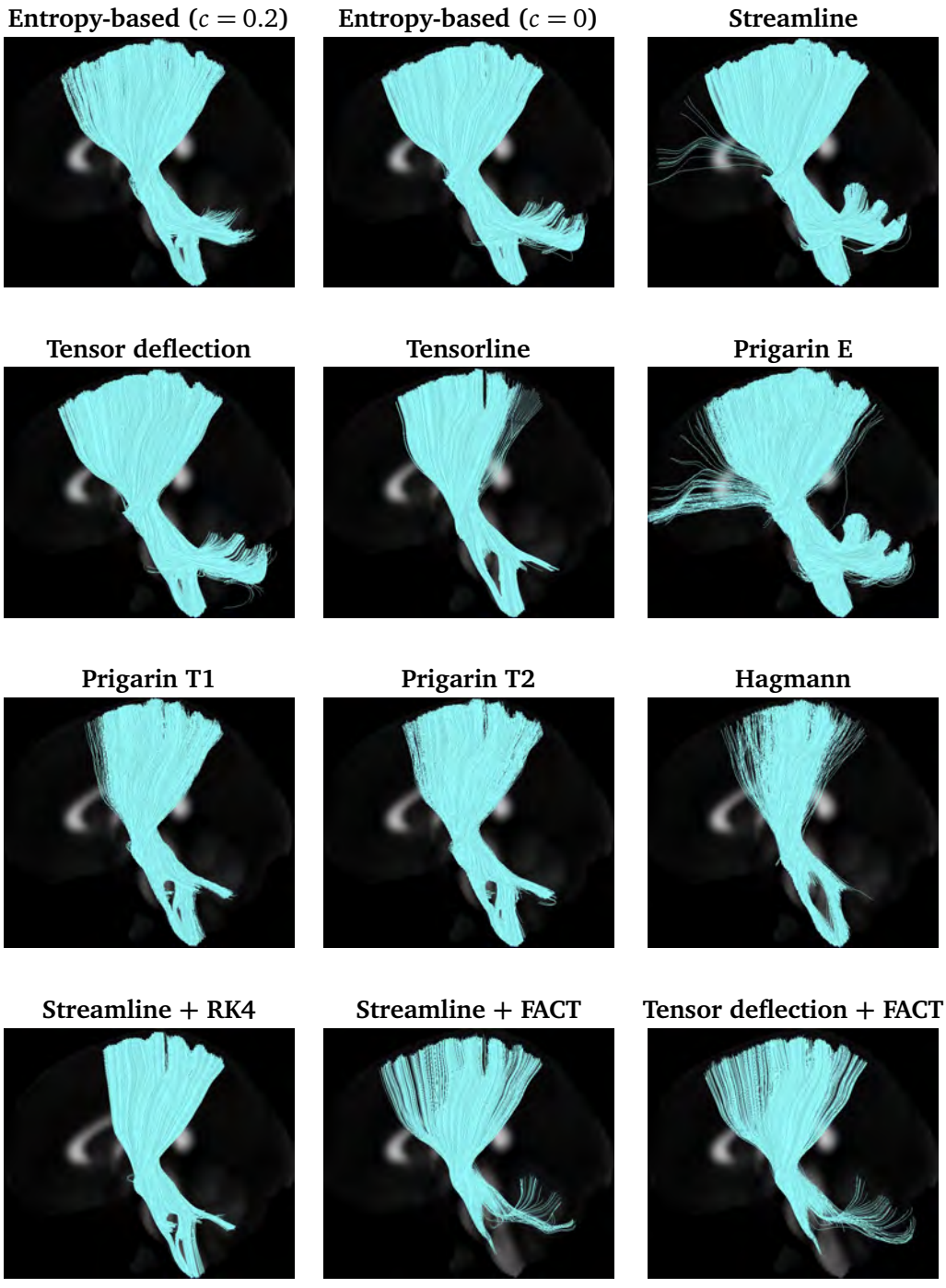

Figure 4.6: Sagittal view of the corticospinal tract from DTI brain atlas data reconstructed with each of the evaluated methods.

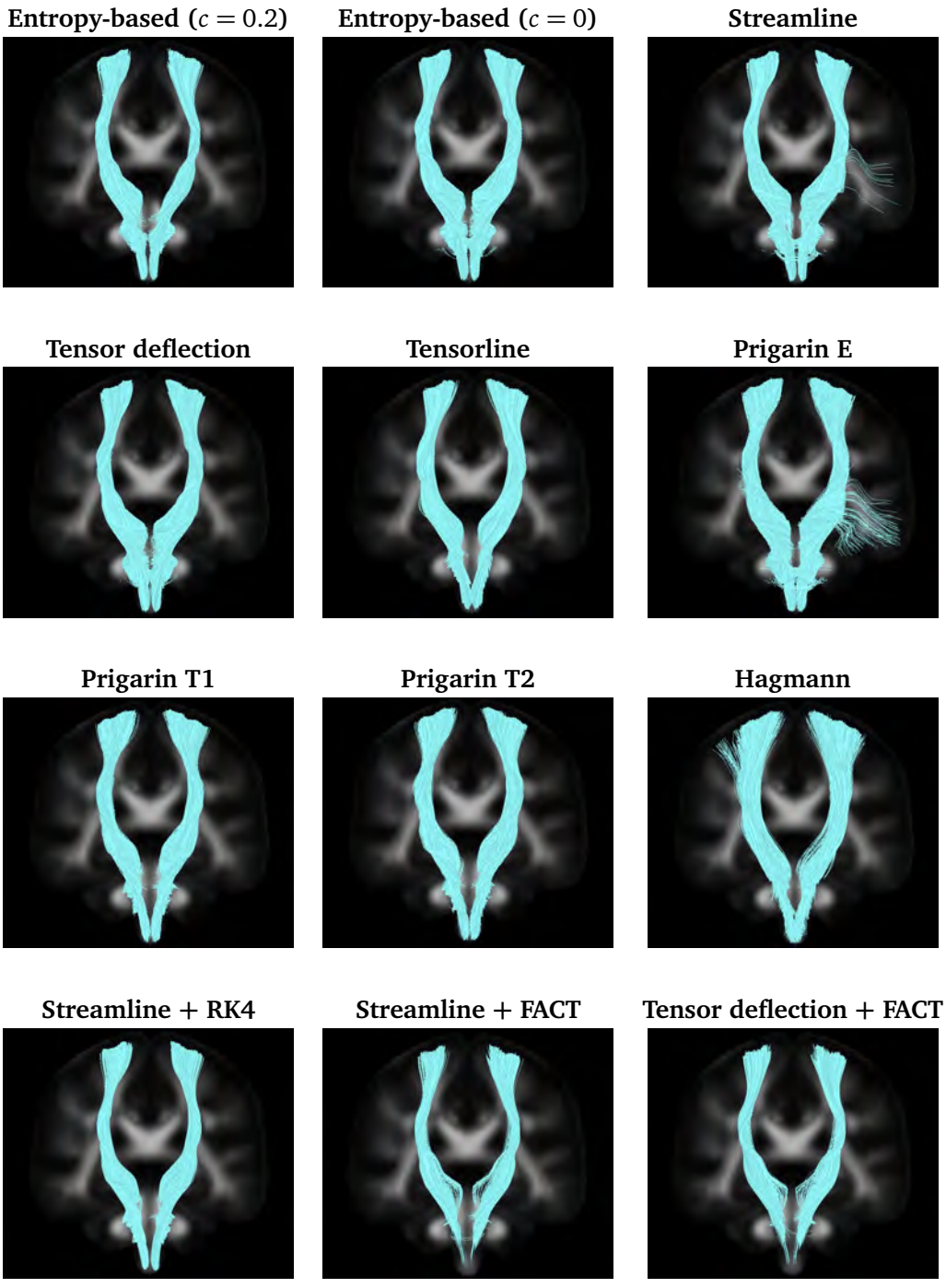

Figure 4.7: Coronal view of the corticospinal tract from DTI brain atlas data reconstructed with each of the evaluated methods.

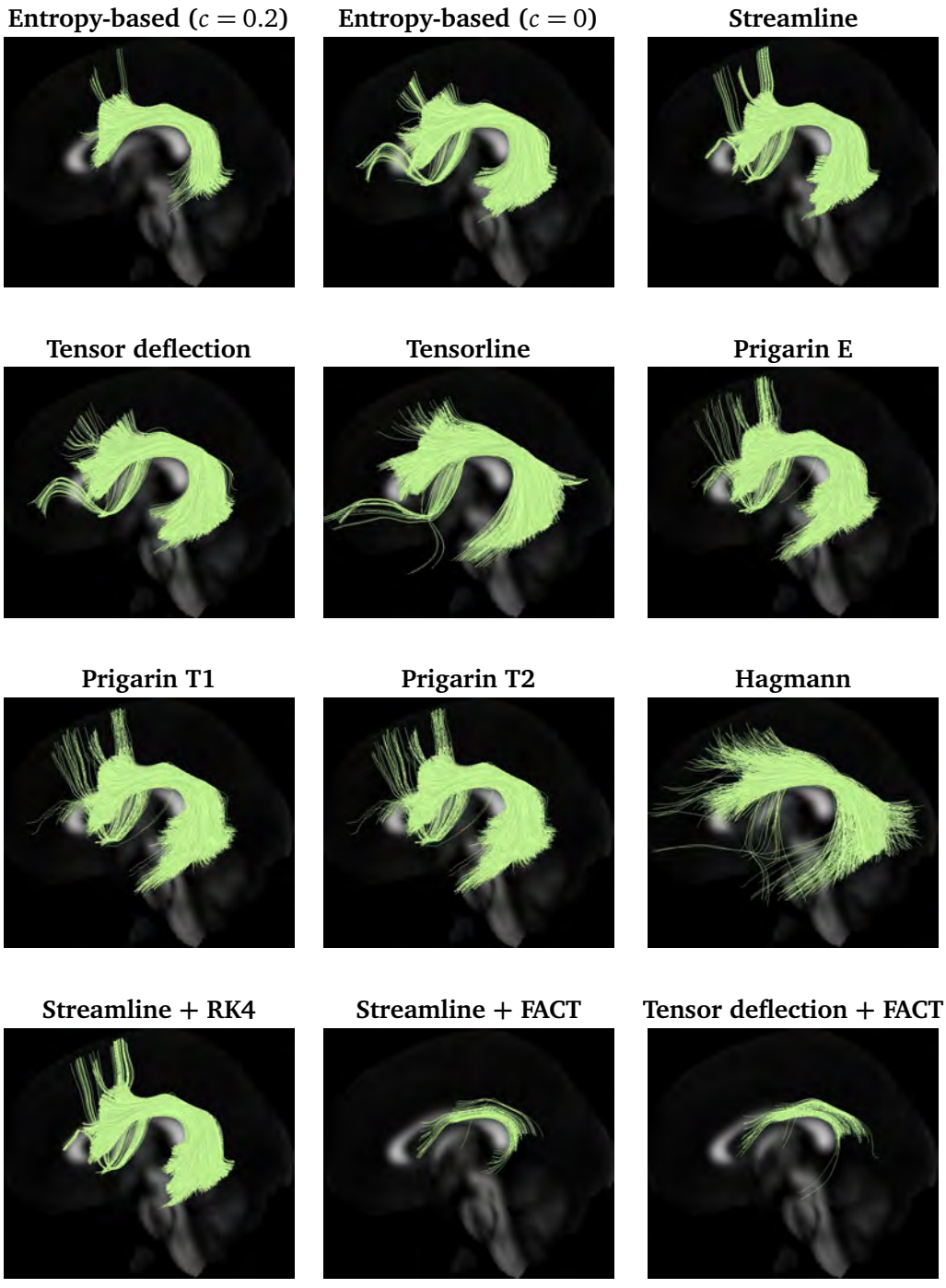

Figure 4.8: Sagittal view of the arcuate fasciculus from DTI brain atlas data reconstructed with each of the evaluated methods.

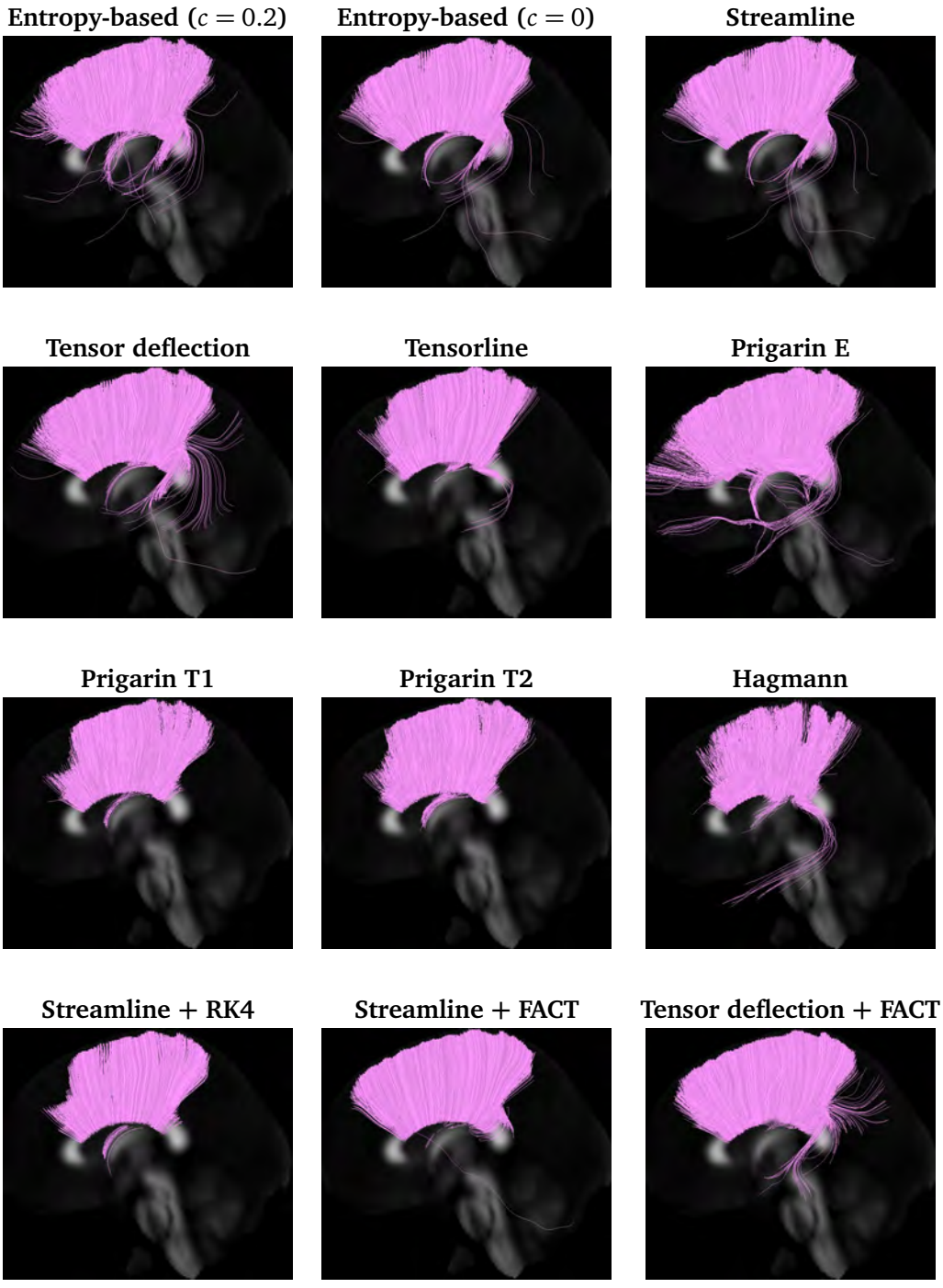

Figure 4.9: Sagittal view of the body of corpus callosum from DTI brain atlas data reconstructed with each of the evaluated methods.

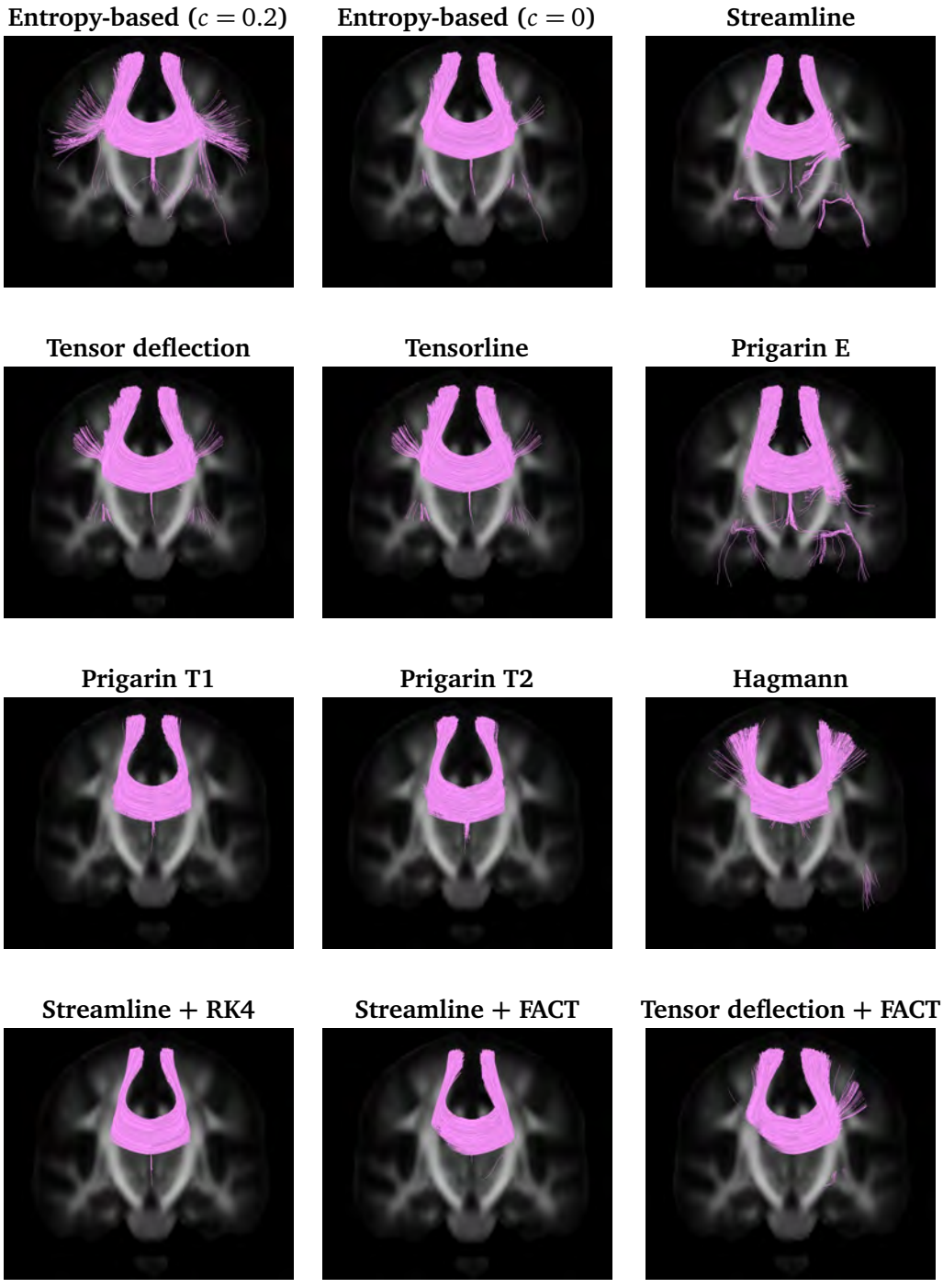

Figure 4.10: Coronal view of the body of corpus callosum from DTI brain atlas data reconstructed with each of the evaluated methods.

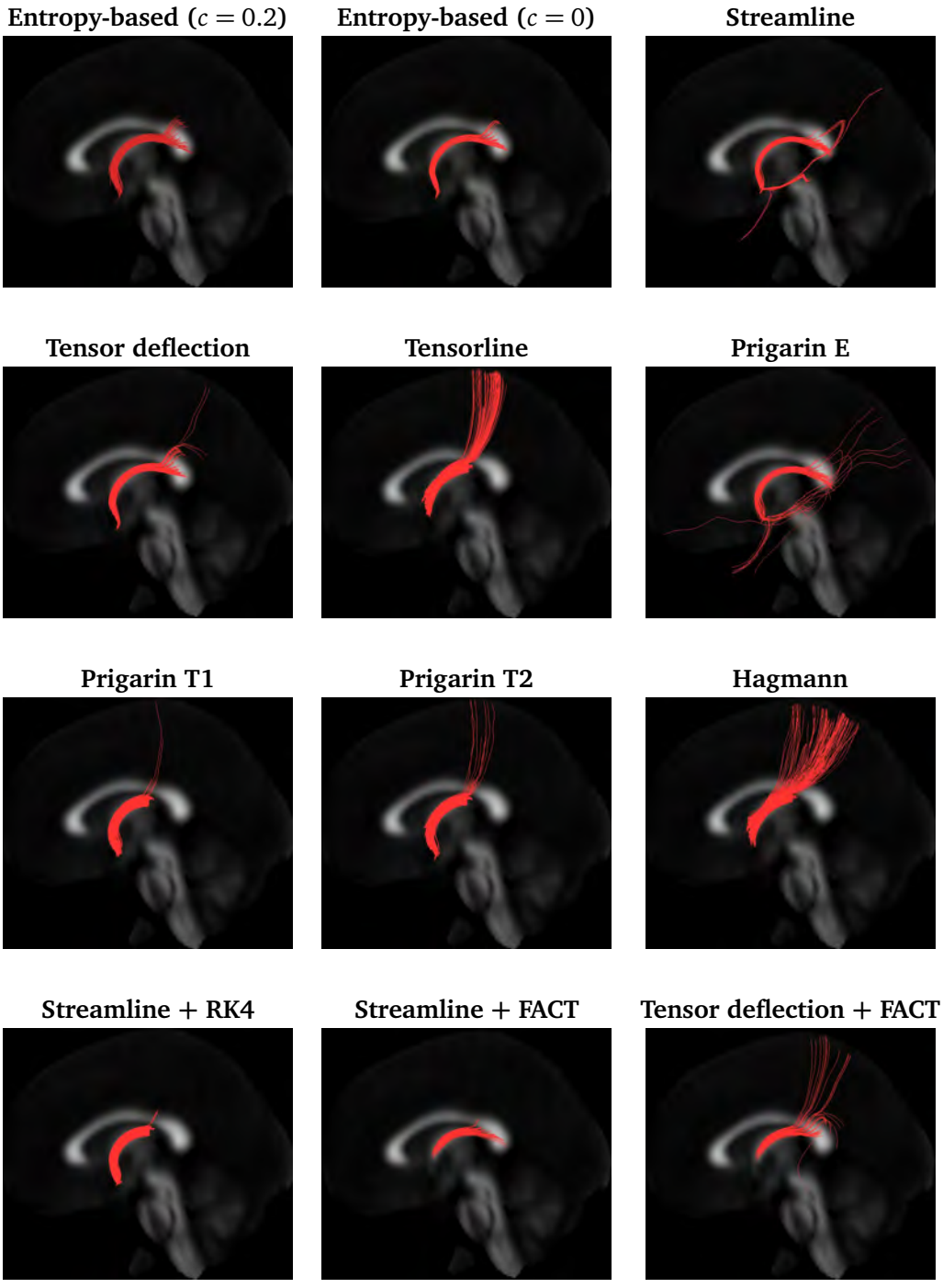

Figure 4.11: Sagittal view of the fornix from DTI brain atlas data reconstructed with each of the evaluated methods.

To evaluate the proposed approach we have selected four anatomical structures from the DTI human brain atlas: corticospinal tract, arcuate fasciculus, body of corpus callosum, and fornix. We have reconstructed them with each of the reported methods. The obtained results have been evaluated by an expert. The obtained results have shown the good performance of the entropy-based approach. Our algorithm reconstructs better than others the selected fiber tracks and detects the lateral projections of corpus callosum, one of the main difficulties of fiber tracking techniques over single tensor data.

CHAPTER 5

Automatic VOI Detection for DTI Seeding

Fiber tracking is the most popular technique for creating white matter connectivity maps from diffusion tensor imaging (DTI). This approach requires a seeding process which is challenging because it is not clear how and where the seeds have to be placed. On the other hand, to enhance the interpretation of fiber maps, segmentation and clustering techniques are applied to organize fibers into anatomical structures. In this chapter, we propose a new approach to obtain automatically and rapidly bundles of fibers grouped into anatomical regions. This method applies an information-theoretic split-and-merge algorithm that considers fractional anisotropy and fiber orientation information to automatically define volumes of interest (VOIs). For each VOI, a number of planes and seeds is automatically placed and, then, fiber bundles corresponding to the VOIs are created. The whole process requires less than a minute and minimal user interaction. The agreement between the automated and manual approaches has been measured for 10 tracts in a DTI-brain atlas and found to be almost perfect (kappa>0.8) and substantial (kappa>0.6). This method has also been evaluated on real DTI-data considering 5 tracts. Agreement was substantial (kappa>0.6) in most of the cases.

5.1 Introduction

The information provided by DTI combined with fiber-tracking techniques allows us to generate connectivity maps that represent the spatial organization of human white matter (see Chapter 4). The most popular fiber tracking representation is the streamline-based approach, which assumes that the direction of fibers is collinear with the maximum diffusivity direction, i.e., the main eigenvector of tensor **D**. All techniques start placing a set of seeds. For each seed, a pathway that follows the maximum diffusivity direction is traced until the boundary of the data set is reached or the value of certain measures at the current curve point lies outside a previously specified admissible range of values.

The seeding strategy, or the placement of seeds, is a key component of the fiber tracking process. To carry out this step two basic alternatives can be considered: the brute-force approach, that places seeds all over the volume, and the region-based approach, that places seeds in the regions-of interest (ROIs) determined by the user. The brute-force approach is computationally more expensive than the ROI-based seeding but it guarantees that all tracks are detected. However, the large amount of generated fibers may turn into cluttered images that make the interpretation and extraction of useful information from the maps difficult. To enhance fiber maps interpretation, different strategies have been proposed. Amongst them, tractography segmentation techniques [123, 124], clustering methods, such as closest point, the mean, and the Hausdorff distances [185, 26, 42, 123, 83, 79], and atlas-based segmentation strategies [104, 178, 109, 122, 123].

In this chapter, we propose a new VOI-based approach that allows us to automatically and almost interactively create bundles of fibers grouped into anatomical regions. Our method uses an information-theoretic split-and-merge algorithm that considers the fractional anisotropy (*FA*) and also the fiber orientation information to automatically define VOIs. For each VOI, the user fixes a seeding rate and, then, fiber tracking is performed. To enhance the interpretation of the created fiber map, a different color is assigned to each of the VOIs and this is also used to color the fiber tracks. The main advantage of this approach is that it requires minimal user interaction and hence the reproducibility is ensured. This method has been validated through comparison with the manual one. For the tests, two different datasets have been considered, the DTI-based human brain atlas ICBM-DTI-81 from the Laboratory of Brain Anatomical MRI from the Johns Hopkins University and DTI-data from different healthy subjects.

This chapter has been structured as follows. Section 5.2 describes some related seeding strategies and the partitioning algorithm used to define the VOIs. Section 5.3 introduces our automated fiber reconstruction approach. Section 5.4 describes the evaluation framework that uses real DTI data and DTI atlas-based data. Section 5.5 and 5.6 show and discuss the obtained results, respectively. Finally, Section 5.7 presents the conclusions.

5.2 Background and Related Work

In this section, we review the main seeding strategies that have been proposed. We also describe the 2D image partitioning algorithm that will be extended in our approach.

5.2.1 Seeding

Over the years, different researchers have attempted to develop effective seed placement algorithms for a better visualization of streamlines [80, 111, 161, 180]. However, most of them were developed for 2D vector fields and, thus, cannot be directly applied to visualize 3D data. The visualization of 3D vector fields is still challenging due to the visual cluttering and computational cost of fiber generation. In the context of DTI, most of the streamline algorithms do not incorporate seeding strategies at all or only make use of the anisotropy measure for seeding purposes. Two seedings strategy groups are used in DTI. First, seeds are placed over the whole volume and, second, seeds are placed in pre-defined regions of interest.

In the first seeding strategy group, Zhang et al. [184] proposed a uniform seeding throughout the entire volume and then used culling algorithms based on a geometric distance between pairs of streamtubes to control the streamline density for a better visualization. The metrics for the culling process include the length of a trajectory, the average linear anisotropy along a trajectory, and the similarity between a trajectory and the group of trajectories already selected. Yonas et al. [154] proposed an adaptive seeding strategy based on tensor dissimilarity metrics that take into account both diffusion magnitudes and directions. They used tensor dissimilarity measures based on the Log-Euclidean framework and the J-divergence metric. Vilanova et al. [164] extended Jobard's seeding algorithm [80] for 3D DTI-data. They determine the seeding and generation of streamlines by a parameter that defines the density of the streamlines, given by the minimal distance between streamlines. A limitation of the method arises when the density is set to a low value since it does not guarantee that the important structures are visible.

In the second seeding strategy group, there are ROI-based approaches that are computationally less expensive than the previous methods. However, they could be more time consuming since they require a skilled operator to delineate the ROIs corresponding to the tracks of interest [118, 131, 121, 37]. Moreover, since approaches are completely user dependent, their reproducibility are limited. Several techniques have been proposed to automate the ROI definition process, such as atlas-based strategies [188, 189, 102]. The idea of these methods is simple because an expert defines 3D ROIs in a representative 3D brain image, denoted atlas. This atlas, with the predefined ROIs, is linearly or non-linearly warped to the subject data. The accuracy of the warping of the atlas to the subject and the feasibility of tract reconstruction are the main limitations of the approach [189].

The method that we present can be considered as an interactive approach, whose difference to other methods is that it reduces the user interaction by defining VOIs automatically. A main part of this method is the split-and-merge algorithm applied

to define the VOIs. This algorithm is based on the information-theoretic 2D image partitioning algorithm [144] described below.

5.2.2 2D Image Partitioning Algorithm

Rigau et al. [144] proposed an information-theoretic partitioning algorithm. In this algorithm, the partitioning of a 2D image is guided by the maximization of mutual information gain and is constructed from an information channel $X \rightarrow Y$ between the random variables X (input) and Y (output), which represent, respectively, the set of regions $\mathscr{X}$ of an image and the set of intensity bins $\mathscr{Y}$. These notions of information theory can be found in Section 2.5 and in Cover and Thomas' book [43].

To describe the method, first, we define the information channel and, then, we review the partitioning algorithm. The channel $X \rightarrow Y$ is defined by a conditional probability matrix $p(Y|X)$ which expresses how the pixels corresponding to each region of the image are distributed into the histogram bins. Note that the capital letters X and Y as arguments of $p()$ are used to denote probability distributions. For instance, while $p(X)$ represents the input distribution of the regions, $p(x)$ denotes the probability of a single region x.

Given an image with N pixels, the three basic elements of the channel $X \rightarrow Y$ are:

- The conditional probability matrix $p(Y|X)$, which represents the transition probabilities from each region of the image to the bins of the histogram, is defined by $p(y|x) = \frac{n(x,y)}{n(x)}$, where $n(x)$ is the number of pixels of region x and $n(x,y)$ is the number of pixels of region x corresponding to bin y. Conditional probabilities fulfil $\sum_{y \in \mathscr{Y}} p(y|x) = 1$, $\forall x \in \mathscr{X}$.

- The input distribution $p(X)$, which represents the probability of selecting each image region, is defined by $p(x) = \frac{n(x)}{N}$ (i.e., the relative area of region x).

- The output distribution $p(Y)$, which represents the normalized frequency of each bin y, is given by $p(y) = \sum_{x \in \mathscr{X}} p(x)p(y|x) = \frac{n(y)}{N}$, where $n(y)$ is the number of pixels corresponding to bin y.

The mutual information (MI) between Y and X is given by

$$I(X,Y) = \sum_{x \in \mathscr{X}} p(x) \sum_{y \in \mathscr{Y}} p(y|x) \frac{p(y|x)}{p(y)} \tag{5.1}$$

and represents the shared information or correlation between X and Y. It is important to note that the maximum MI that can be achieved in the partitioning process is the entropy $H(Y)$ of the histogram, given by

$$H(Y) = -\sum_{y \in \mathscr{Y}} p(y) \log p(y). \tag{5.2}$$

The entropy $H(Y)$ represents the information content of the image.

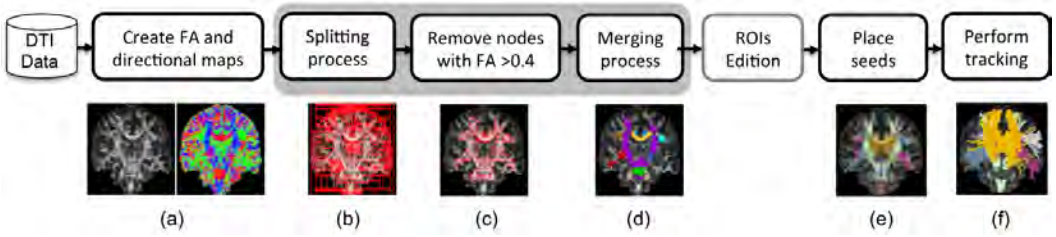

Figure 5.1: Pipeline of the proposed approach. The core of the method is the split-and-merge algorithm. (a) *FA* and RGB maps, (b) VOIs obtained from the splitting process, (c) VOIs with $FA > 0.4$, (d) VOIs obtained from the merging process. (e) seed placement, and (f) obtained tracks.

The partitioning algorithm is a greedy top-down procedure which partitions the image in quasi-homogeneous regions. The partitioning strategy takes the full image as the unique initial partition and progressively subdivides it with vertical or horizontal lines chosen according to the maximum MI gain for each partitioning step. This algorithm produces a binary space partition (BSP) driven by the maximum information gain and stops when a given mutual information ratio $MIR = \frac{I(X,Y)}{H(Y)}$ or a predefined number of regions is achieved.

5.3 Automated Fiber Reconstruction Algorithm

The kernel of our information-theoretic approach for automated white matter fiber tract reconstruction is a split-and-merge strategy applied to decompose the DTI volume in a set of VOIs. Before defining the details of this strategy, we give a global view of the whole approach composed of seven steps (see Figure 5.1). We also show an example of the obtained result for each step. In the first step, from the DTI-data we generate both the *FA* and the *RGB* maps representing the main diffusivity direction e_1 (see Figure 5.1(a)). In the second step, we apply a splitting process (described in detail below) to decompose the volume in regions (see Figure 5.1(b)). These regions are represented as nodes of a hierarchical data structure. In the third step, from this hierarchical structure, we eliminate the terminal nodes with $FA \leq 0.4$, considering that the *FA* of a node is the mean of the *FA* of all the voxels represented in the node (see Figure 5.1(c)). In the fourth step, we apply a merging process (described in detail below) that returns the final VOIs corresponding to the terminal nodes of the hierarchical structure (see Figure 5.1(d)). The fifth step is optional and consists in the edition of the results. The user can apply boolean operations to the VOIs that have been automatically obtained. In the sixth step, the user defines a seeding rate for each VOI and we automatically place the corresponding seeds (see Figure 5.1(e)). In the last step, we perform the fiber tracking using the Lazar [99] technique. We assign a different color to each VOI and this is used to render the generated fibers (see Figure 5.1(f)).

5.3.1 Split-and-Merge Algorithm

The core of our approach is the split-and-merge algorithm used to decompose the DTI model in a set of VOIs. This algorithm is based on the information-theoretic image partitioning algorithm described in Section 5.2.2.

To reach our goal, instead of considering the original DTI data, we take as input of the method two different measures that can be derived from DTI: the *FA* values, represented by a grey scale volume, and the main diffusivity direction e_1, represented by an *RGB* volume, where *R*, *G* and *B* correspond to the X, Y and Z components of e_1. We consider $FA \geq 0.4$ as a cutoff to indicate white matter regions and e_1 as the information required to identify the direction of the fibers contained in one anatomical structure. Since directional information is represented as an *RGB* value, the direction of the voxels is examined by considering the color codification.

The proposed split-and-merge algorithm proceeds in two different phases. The first one is the split phase that extends the 2D partitioning algorithm presented by Rigau et al. [144] (see Section 5.2.2) to a 3D volume data set. The main novelty in our 3D algorithm is that the *FA* and *RGB* values are considered together in order to segment the volume (or define the VOIs). Unlike the original 2D split algorithm, where only one information channel is taken into account, four information channels are now defined, respectively, between the random variable V, which represents the set of obtained VOIs, and the histograms of random variables *FA*, *R* (red), *G* (green) and *B* (blue), which represent the input data. In all cases, the bins of these histograms are normalized in the range [0..255]. To start the split phase, the full volume is taken as the initial partition and it is progressively subdivided using planes in the X, Y or Z directions according to the maximum mutual information (MI) gain for each partitioning step (see Section 5.2.2). This gain is obtained by the sum of the specific MI gains of each channel. The process stops when the mutual information ratio (MIR) provided by the user is reached. The mutual information ratio is now defined as

$$MIR = \frac{I(V,FA) + I(V,R) + I(V,G) + I(V,B)}{H(FA) + H(R) + H(G) + H(B)}, \tag{5.3}$$

where the terms $I(V,.)$ and $H(.)$ express, respectively, the information gain obtained using the different channels and the entropy of random variables *FA*, *R*, *G* and *B*. Finally, the split phase returns a binary space partition of the volume data set coded in a hierarchical data structure.

Before starting the merging, we remove the VOIs (terminal nodes of the created tree) with the mean of *FA* less than 0.4. We consider that these nodes are not good candidates for seeding since we cannot ensure that their fibers are coherently organized [6, 118, 136]. The second phase of the algorithm performs the merging of the VOIs according to the directional information of the fibers contained in them. That is, we successively merge the terminal nodes that have the lowest directional dissimilarity and the same dominant direction (or color). Remember that the directional information of each terminal node is coded as an *RGB* value, obtained from the mean of *RGB* values of all voxels of the node. The dissimilarity between two neighbor terminal nodes

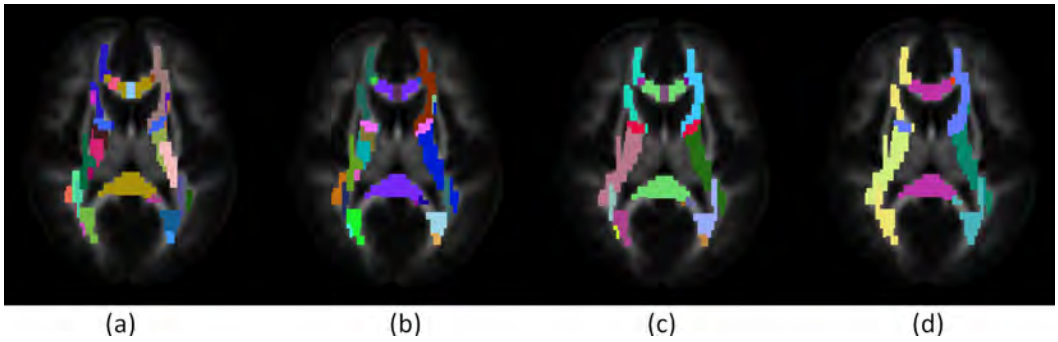

Figure 5.2: VOIs obtained at different levels of the merging process with $MIR = 0.5$. The number of VOIs is (a)125, (b)100, (c)75 and (d)50.

is calculated by the Euclidian distance between their respective *RGB* values. Thus, since we only merge VOIs with the same principal color, the main merging criterion is given by the minimum directional dissimilarity. Observe that, if we do not introduce a specific stopping criterion (i.e., a predefined number of nodes), the merging process will end when adjacent VOIs have a different color.

The obtained nodes are the VOIs where seeds will be placed. It is important to emphasize that the proposed algorithm is completely automatic and only requires the definition of a MIR parameter and, if desired, the final number of VOIs.

To store all computations, the algorithm creates a hierarchical data structure that allows us to obtain and consult intermediate results. These results are given by images that can be obtained interactively. Therefore, the user can consult them before selecting the final option. Figure 5.2 illustrates results of the merging at different levels of the process. All the images have been obtained with $MIR = 0.5$, and from left to right the number of VOIs is 125, 100, 75 and 50, respectively.

At the end of the algorithm, the results can be edited by the user before starting the next phase. In this edition step, voxels can be added or removed from the VOIs and also boolean operators between VOIs can be applied. As we will see in Section 5.5, in most cases, the required edition is minimal.

5.3.2 Seeding

To avoid seeding all the VOIs we propose to automatically define ROIs into the VOIs. These ROIs are created as follows. First, we consider the dominant direction of the VOI, which is obtained from the mean of *RGB* values of all voxels of the VOI. Then, we compute the intersection planes perpendicular to the dominant direction. These intersection planes are considered as ROIs and can be used as seeding planes or as reception planes. The reception planes are used to determine if a fiber has to be considered or not as a member of the anatomical region to be reconstructed. We have imposed the restriction that all reconstructed fibers in a VOI have to intersect two reception planes.

The user determines the number of planes to be placed and the number of seeds

per voxel contained in the ROI. The number of planes is expressed as a percentage (%) with respect to the size of the VOI. Then, we automatically place the planes or ROIs. We start placing the first ROI in the middle of the VOI and the subsequent ones at the same distance from the first one in the opposite directions. In addition, for each VOI we define two reception planes. Although they can be located in different positions of the VOI, we have experimentally observed that the best results are obtained when they correspond to the two largest planes located between the middle of the VOI and its extremes. In the second column of Figures 5.9 and 5.10, we show the VOIs and the reception planes automatically created to reconstruct different anatomical structures.

Finally, seeds are randomly placed in the seeding planes and the fiber tracking algorithm is applied. The obtained fibers are colored according to an arbitrary color assigned to the VOI at the end of the split-and-merge process. In this way, the created fibers can be seen as bundles of fibers corresponding to the created VOIs. Note that during all the process the user interaction is minimal.

5.4 Validation Framework

In this section, we present the basis of our validation framework.

5.4.1 MRI Data

DTI-data sets have been obtained from five volunteers as described in Section 3.4.2. Moreover, the DTI-based human brain atlas has been obtained from the International Consortium for Brain Mapping (ICBM) database (see Section 4.4 for a more detailed description).

5.4.2 Manual Fiber Reconstruction

To create the manual fiber reconstruction for the real DTI data, a medical expert considered eight different anatomical structures: the corticospinal, the corpus callosum, the cingulum, the inferior fronto-occipital fasciculus left and right, the superior longitudinal fasciculus left and right, and the middle cerebellar peduncle.

For each subject, the medical expert defined these structures as follows. First, he defined different ROIs to reconstruct the evaluated structures using the 3D editor of AMIRA [155]. Then, since the corticospinal tract is composed by the fibers that traverse the middle pons and finish at the subcortical white matter [70, 117], the expert drew one square ROI at the base of the middle pons and a VOI covering all the subcortical white matter located above the slice corresponding to the superior part of the corpus callosum, mainly containing the frontal and parietal lobes. To define this last region, the T1 image has been segmented using SPM5 [11], obtaining three probability maps: grey matter (GM), white matter (WM), and cerebrospinal fluid (CSF). To select cortical grey matter voxels, a threshold of 0.7 has been applied to the GM probability map. It has been experimentally proven that this threshold value separates the GM voxels with a high probability. The obtained mask (GMm) has been superimposed with the T1

image and the misclassified voxels have been removed by editing manually. Since the obtained VOI only contains the voxels upper to the axial plane superior to the thalamus, the medical expert has applied a three step process to obtain the subcortical white matter VOI: (i) the mask (WMm) from the probability map of white matter with a 0.7 threshold has been obtained, (ii) a dilatation of three voxels of GMm have been performed, and (iii) the intersection of WMm and the dilated GMm has been carried out obtaining the subcortical white matter VOI.

To define the structure of the corpus callosum [179, 117], the 10 mid-sagittal slices of the WMm have been selected and four rectangular ROIs have been defined around it. Three of these ROIs have been used to obtain the fibers of the genu, the body, and the splenium of the corpus callosum, and the fourth has been defined to avoid the association with corpus callosum of fibers from the corticospinal tract.

The cingulum has been selected from the subcortical white matter VOI by considering the underlying cingulate gyrus voxels and adding two perpendicular squared ROIs at the extremes. The VOIs defined on the high resolution T1 image have been registered with the b0 images using a 12-parameter affine registration.

To define the inferior fronto-occipital fasciculus, two ROIs along the course of the inferior fronto-occipital fasciculus [32, 165] in the coronal plane of the T1 images at the level of the anterior commissure and the pontine crossing fibers have been placed, respectively. The defined VOIs have been registered with the b0 images using a 12-parameter affine registration.

The superior longitudinal fasciculus has been defined as in Bernal et al. [24], placing bilaterally squared ROIs at the triangular-shaped region lateral to each of the corticospinal tracts in a coronal plane along the rostral aspect of the corpus callosum. A sagittal colored based *FA* image has been used to determine the rostral endpoint of the superior longitudinal fasciculus fibers in the white matter pertaining to specific gyri or pars of the frontal lobe.

To obtain the middle cerebellar peduncle, two ROIs have been defined. The first one placed across the pons, for selecting lateral fibers contained in this region, and the second one, on the cerebellum.

After defining all the VOIs, to reconstruct the fiber tracks, three seeds per voxel have been placed all over the brain and, then, the Lazar method [99] has been applied. We have only considered the fibers intersecting the defined VOIs and, for each one, we have created a mask containing all the voxels intersected by the fibers of the corresponding structure.

For the evaluation of the DTI-brain atlas we have selected from the white matter parcellation map, provided together with the DTI-brain atlas, the following structures: the corticospinal tract left and right, the corticospinal tract complete, the corpus callosum, the cingulum, the inferior fronto-occipital fasciculus left and right, the superior longitudinal fasciculus left and right, and finally the middle cerebellar peduncle. To create the tracts, we applied the Lazar method [99] with one seed per voxel in voxels with $FA > 0.4$. The stop criteria in all the cases is $FA < 0.2$ and the angle $< 100^o$. To delineate the fiber bundles more accurately, the medical expert has defined some selection ROIs, in addition to the provided parcellation, following [39, 32, 165].

5.4.3 Evaluation Metrics

To evaluate the accuracy of the proposed approach we compared the automated tracking results with the manually-based tractography results for the set of selected anatomical structures.

The spatial matching between manual and automated results was examined using the kappa analysis [93]. The automated and manual tracking results were first converted to binary images with the same dimension as the DTI data (181x217x181), where the value 1 was assigned to the voxels occupied by the tracts and the value 0 to non-occupied voxels. The two tracking results were then superimposed, and voxels were classified into three categories: (1) voxels that did not contain the tract in either trial (nn); (2) voxels that contained the tract in only one of the two trials (pn, np); and (3) voxels that contained the tracts in both trials (pp). The κ (kappa) value of the manual and automated reconstruction of selected tracts was calculated. According to the Landis and Koch criterion [93], a κ value of $0.11-0.2$ is considered *slight*, $0.21-0.4$ is *fair*, $0.41-0.60$ is *moderate*, $0.61-0.80$ is *substantial*, and $0.81-1.0$ is *almost perfect* agreement.

5.5 Results

The presented approach requires different parameters: MIR, for controlling the splitting phase, *the number of regions*, that the merging phase has to return, and, *seeding rate*, for reconstructing the fiber bundles. To determine the values of these parameters we have designed several tests.

All experiments have been done considering the two testing data sets, the atlas and the five controls DTI-data. The experiments presented in this section have been carried out on a Laptop with a Core 2 Duo-2.5Ghz and 3Gb RAM.

5.5.1 Setting Algorithm Parameters

First, to determine the optimal MIR, we have evaluated the gain of MIR that is obtained for different partitions, i.e., different levels of splitting and also the computation time required to obtain the partitions. The obtained results are plotted in Figure 5.3(a), where axis x corresponds to the total MIR, i.e., the accumulated MIR at the current partition, and axis y represents the gain of MIR obtained with the current partition. We also record the computation time of splitting. This is plotted in Figure 5.3(b) where x represents the MIR and y the computation time in seconds. The red plot represents the average of the results for each of the controls and the blue plot corresponds to the atlas. Observe that in both cases computation time increases much more rapidly than the gain of MIR when $MIR > 0.4$ (see Figure 5.3). Therefore, we consider that a trade-off between MIR and processing time is achieved when $0.4 \leq MIR \leq 0.5$. Computation time is higher for the atlas because it has a higher resolution than the real DTI-data.

Controls	After splitting	With $FA \geq 0.4$	After merging	Time
Control 1	1474	130	28	40
Control 2	2241	293	46	44
Control 3	2441	294	43	46
Control 4	1955	207	37	42
Control 5	2223	225	43	45

Table 5.1: Number of nodes generated at the different steps of the split-and-merge process. Split-and-merge computation time in seconds.

The proposed method, once the splitting phase has finished, removes the nodes with $FA < 0.4$ and then performs the merging of 'similar' nodes. To stop the merging process, we can give the MIR or the number of final VOIs. To analyze the effect of these alternatives we have performed two different experiments. The first experiment considers the five controls DTI-data and performs merging until no more partitions (or VOIs) can be merged since their dominant direction is different. In Table 5.1 we illustrate the evolution of the whole process. From left to right, we have reported for each of the subjects the number of terminal nodes at the end of the splitting step, after removing partitions with $FA < 0.4$ and after the merging step. We have also recorded in the last column the computation time. Note that during the splitting process the algorithm approximately decomposes the volume in 2000 partitions. Almost 70% of regions are discarded since their mean is $FA < 0.4$. The merging phase returns between 30 and 40 VOIs.

The obtained results for the atlas dataset and for one of the controls are shown in Figure 5.4. Note that the main anatomical structures are detected. A similar behavior has been obtained with the other subjects. Observe that although the splitting step uses horizontal and vertical planes to decompose the volume and this will not result in meaningful anatomical regions, when the merging phase is applied, these regions are more correctly delineated.

The second experiment has been carried out on the DTI-brain atlas. In this case we have considered the 10 selected regions of interest, the left and right corticospinal tract, the complete corticospinal tract, the corpus callosum, the cingulum, the left and right inferior fronto-occipital fasciculus, the left and right superior longitudinal fasciculus, and the middle cerebellar peduncle. We have analyzed the number of regions obtained at different levels of the merging process (see Figure 5.2). We have observed that when the number of regions is 90, the selected structures can be identified and only some boolean operations are required (see Figure 5.4(b)).

5.5.2 Determining the Seeding Rate

To determine the seeding rate, we have considered the two testing data sets and for each evaluated structure, a different number of planes and also a different number of seeds for the voxels contained in the planes.

For each structure, we have defined two reception planes corresponding to the two largest planes located between the middle of the VOI and its extremes following

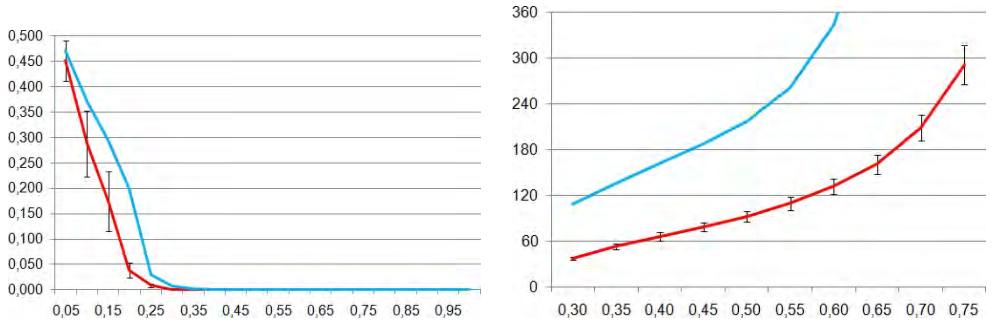

(a) (b)

Figure 5.3: Evolution of MIR values. (a) The plot represents the average for 5 controls of the gain of MIR obtained with each new partition where axis x corresponds to the accumulated mutual information ratio (MIR). (b) Average computation time in seconds for 5 controls according to MIR (axis x).

the dominant direction of the VOI. Then we have defined 10%, 25%, 50%, 75%, and 100% of planes, where the % represents the number of planes with respect to the length (in voxels) of the VOI in the dominant direction, the 100% case is when the number of planes is equal to the length of the VOI. To evaluate the effect of a different number of seeds we have placed from 1 to 6 seeds per voxel. After the seeds have been placed, we have applied Lazar method [99] to reconstruct the bundle of fibers representing the anatomical structure. Then, we have created the masks composed of voxels intersected by the fibers of each of the studied structures. Finally, we have tested the spatial matching agreement between automated and manual methods by kappa values. Figures 5.5 and 5.6 present the results obtained for the DTI-brain atlas and, Figures 5.7 and 5.8, for the controls. In Tables 5.2 and 5.3, the best, worst, and average of the agreement between automated and manual methods over the DTI-brain atlas and subject DTI-data are given, respectively.

In Figures 5.9 and 5.10, visual comparison between the manual and automated methods are shown for the cases with the best and worst agreement. From left to right, we present the manual reconstruction, the VOIs and the reception planes automatically defined, and the automated reconstructions with the best and worst agreement, respectively.

Figure 5.11 plots the computation time required to perform the split-and-merge steps for the different evaluated (planes, seeds) configurations.

5.6 Discussion

We have presented a new approach for automated white matter fiber tracts reconstruction based on information-theory. The basis of our approach is an information-theoretic split-and-merge algorithm where fractional anisotropy FA and fiber orientation are used for automatic VOI definition. These VOIs do not aim at representing the structure

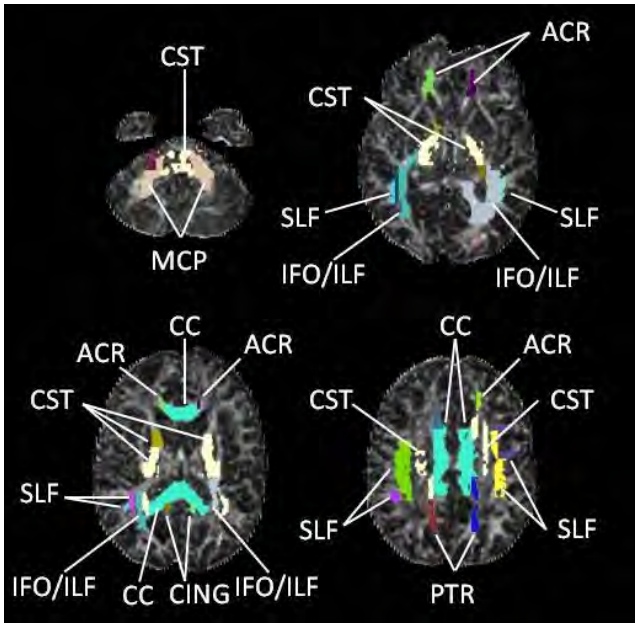

(a)

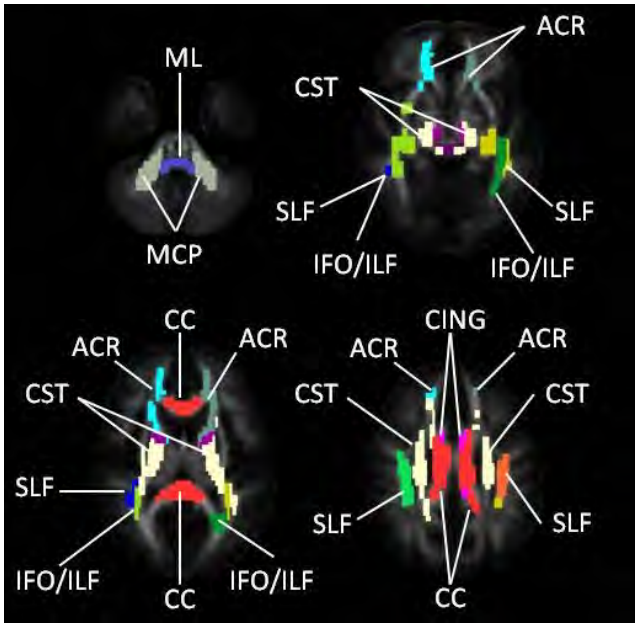

(b)

Figure 5.4: Volumes of interest (VOIs) obtained automatically using the proposed approach with (a) $MIR = 0.4$ for one of the testing data sets and (b) $MIR = 0.5$ for ICBM-DTI-81 atlas. The VOIs are labelled following [117], where ACR: anterior corona radiata, CC: corpus callosum, CING: cingulum, CST: corticospinal tract, IFO: inferior fronto-occipital fasciculus, ILF: inferior longitudinal fasciculus, MCP: middle cerebellar peduncle, ML: medial lemniscus, PTR: posterior thalamic radiation and SLF: superior longitudinal fasciculus.

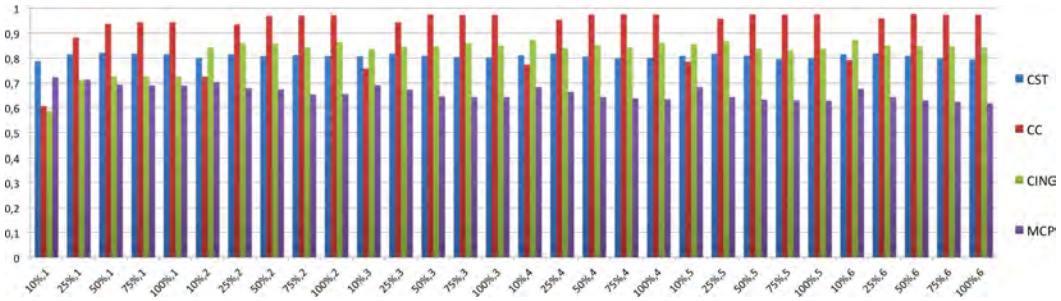

Figure 5.5: Agreement between automated and manual methods for different structures of the DTI-atlas considering different (planes, seeds) configurations. CST: corticospinal tract, CC: corpus callosum, CING: cingulum, MCP: middle cerebellar peduncle.

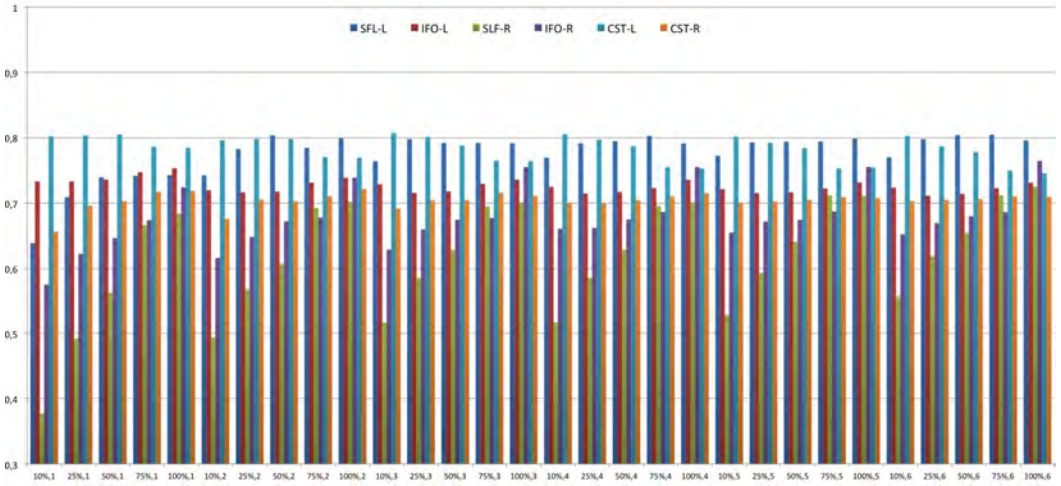

Figure 5.6: Agreement between automated and manual methods for different structures of the DTI-atlas considering different (planes, seeds) configurations. IFO: inferior fronto-occipital fasciculus, SLF: superior longitudinal fasciculus, CST: corticospinal tract.

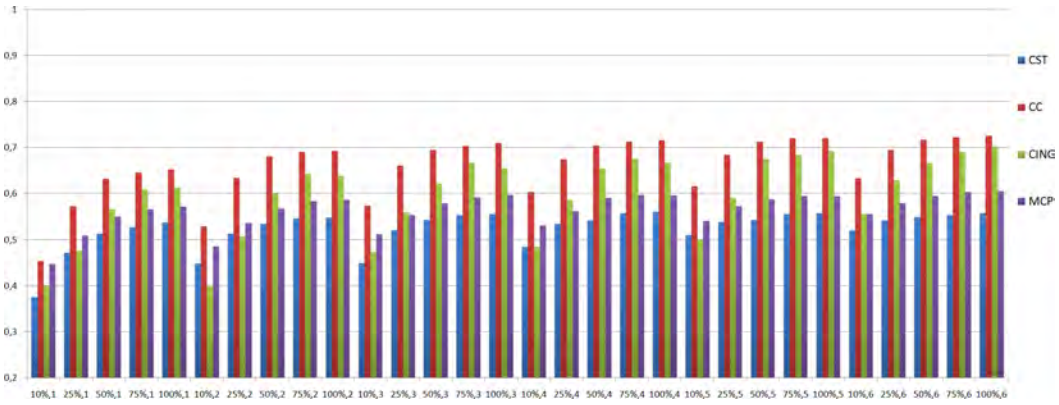

Figure 5.7: Agreement between automated and manual methods for different structures of the DTI-data considering different (planes, seeds) configurations (average of 5 controls). CST: corticospinal tract, CC: corpus callosum, CING: cingulum, MCP: middle cerebellar peduncle.

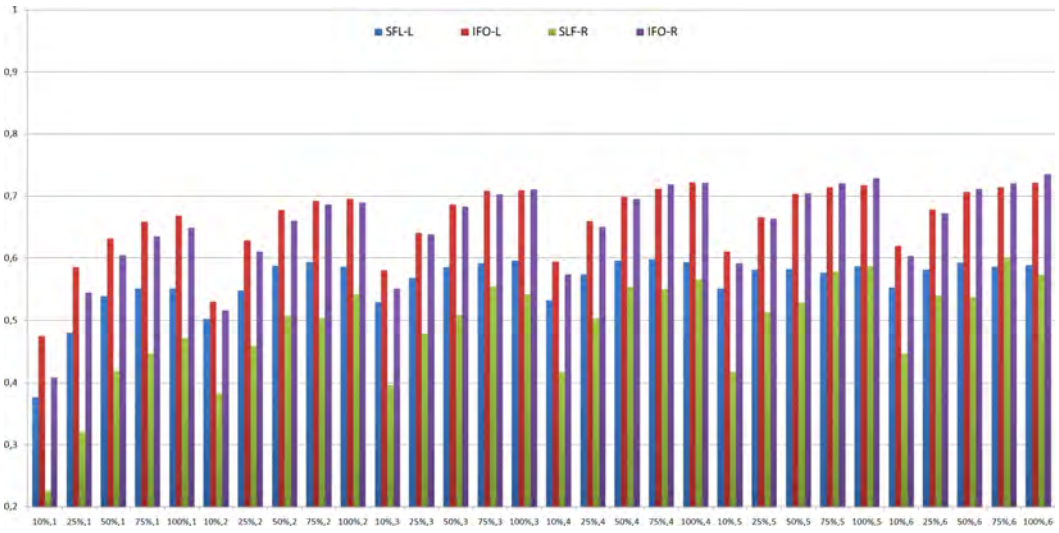

Figure 5.8: Agreement between automated and manual methods for different structures of the DTI-data considering different (planes, seeds) configurations (average of 5 controls). IFO: inferior fronto-occipital fasciculus, SLF: superior longitudinal fasciculus.

	Best Kappa	Worst Kappa	Average
CST-L	0.807 (10%,3)	0.745 (100%,6)	0.787 ± 0.019
CST-R	0.721 (100%,2)	0.656 (10%,1)	0.705 ± 0.013
CST	0.821 (50%,1)	0.787 (10%,1)	0.808 ± 0.008
CC	0.977 (50%,6)	0.606 (10%,1)	0.964 ± 0.096
CING	0.873 (10%,4)	0.585 (10%,1)	0.846 ± 0.064
IFO-L	0.753 (100%,1)	0.711 (25%,6)	0.723 ± 0.010
IFO-R	0.764 (100%,6)	0.575 (10%,1)	0.674 ± 0.044
SLF-L	0.805 (75%,6)	0.638 (10%,1)	0.792 ± 0.035
SLF-R	0.725 (100%,6)	0.377 (10%,1)	0.628 ± 0.085
MCP	0.722 (10%,1)	0.618 (100%,6)	0.654 ± 0.029

Table 5.2: Best, worst and average of the agreement between automated and manual methods over the DTI-brain atlas for the ten evaluated tracts (average of 30 seeding possibilities corresponding to the evaluated (planes, seeds) configuration). The best and the worst result is accompanied by its corresponding configurations given as (planes, seeds). CST: corticospinal tract, CC: corpus callosum, CING: cingulum, IFO: inferior fronto-occipital fasciculus, SLF: superior longitudinal fasciculus, MCP: middle cerebellar peduncle.

	Best Kappa	Worst Kappa	Average
CST	0.562 (100%,4)	0.375 (10%,1)	0.541 ± 0.041
CC	0.725 (100%,6)	0.453 (10%,1)	0.687 ± 0.065
CING	0.702 (100%,6)	0.399 (10%,2)	0.617 ± 0.086
IFO-L	0.722 (100%,4)	0.475 (10%,1)	0.678 ± 0.061
IFO-R	0.735 (100%,6)	0.408 (10%,1)	0.668 ± 0.075
SLF-L	0.598 (75%,4)	0.377 (10%,1)	0.581 ± 0.045
SLF-R	0.600 (75%,6)	0.226 (10%,1)	0.509 ± 0.085
MCP	0.605 (100%,6)	0.448 (10%,1)	0.575 ± 0.037

Table 5.3: Best, worst and average of the agreement between automated and manual methods over the five controls for the eight selected tracts (average of 30 seeding possibilities corresponding to the evaluated (planes, seeds) configuration). The best and the worst result is accompanied by its corresponding seeding configurations given as (planes, seeds). CST: corticospinal tract, CC: corpus callosum, CING: cingulum, IFO: inferior fronto-occipital fasciculus, SLF: superior longitudinal fasciculus, MCP: middle cerebellar peduncle.

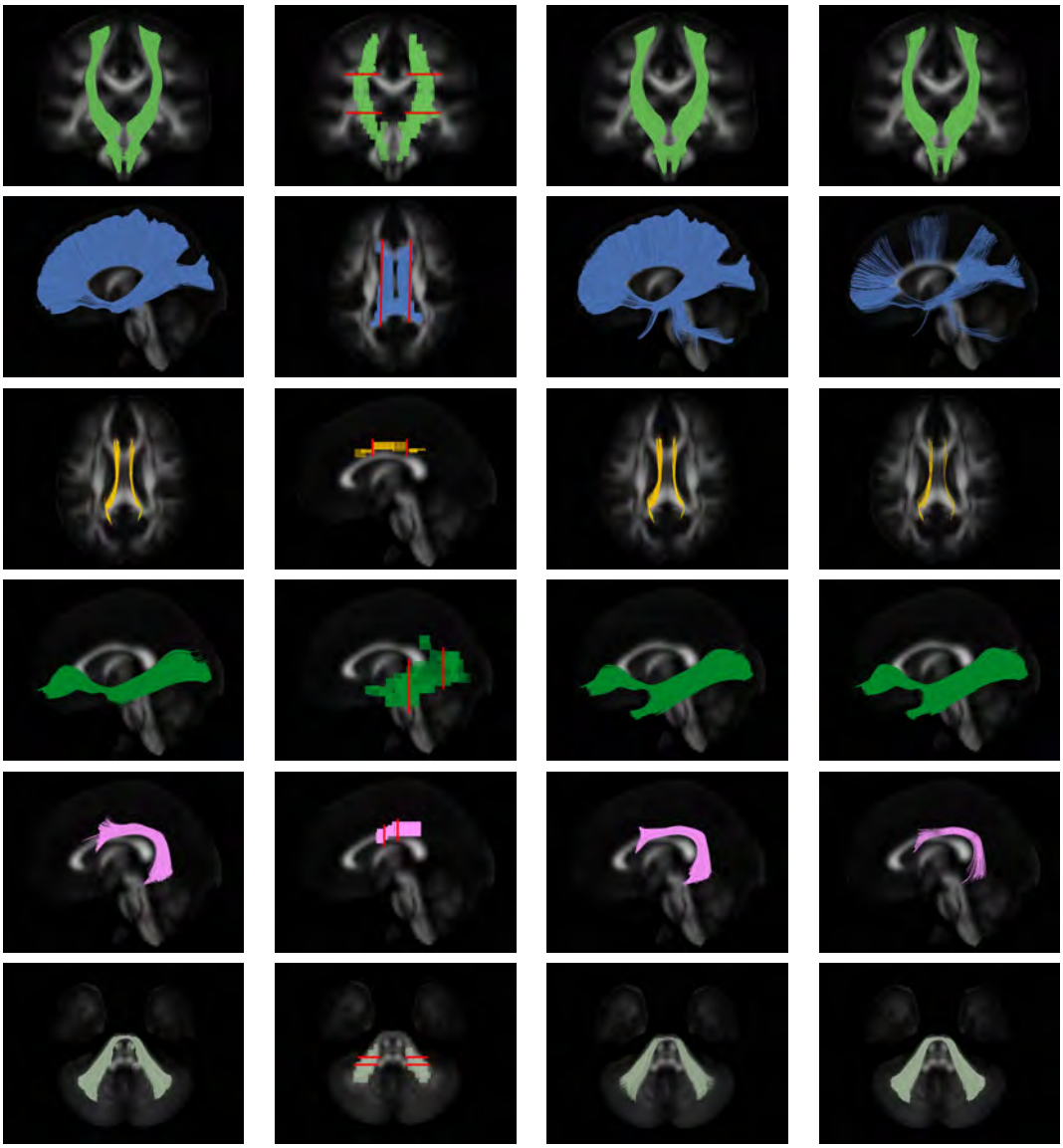

Figure 5.9: From left to right, we present, for the DTI-brain atlas, the manual reconstruction, the VOIs and the reception planes automatically defined with $MIR = 0.5$, and the automated reconstructions with the best and worst agreement, respectively. The evaluated structures are the corticospinal tract, the corpus callosum, the cingulum, the inferior fronto-occipital fasciculus, the superior longitudinal fasciculus, and the middle cerebellar peduncle.

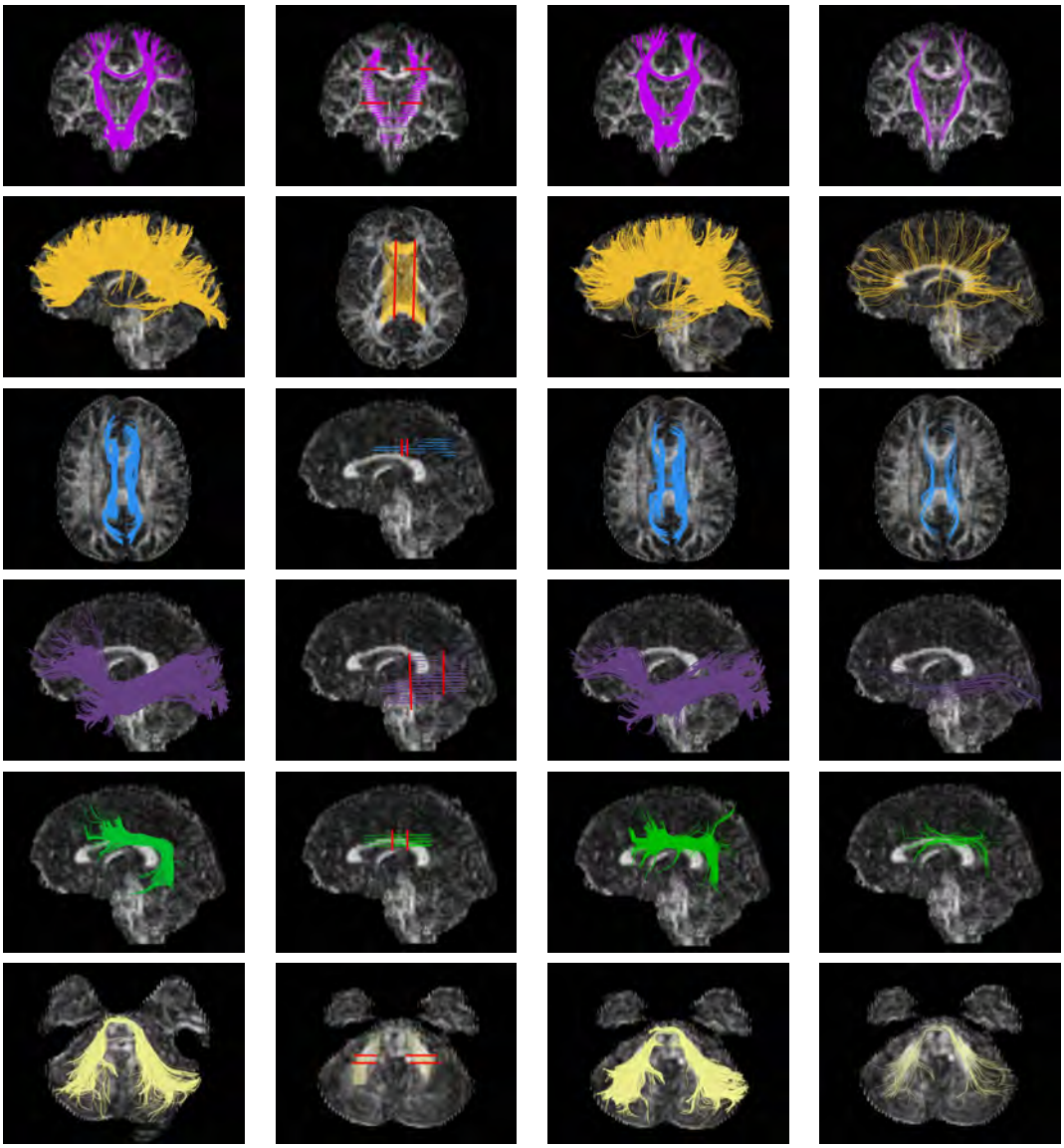

Figure 5.10: From left to right, we present, for the real DTI-data, the manual reconstruction, the VOIs and the reception planes automatically defined with $MIR = 0.4$, and the automated reconstructions with the best and worst agreement, respectively. The evaluated structures are the corticospinal tract, the corpus callosum, the cingulum, the inferior fronto-occipital fasciculus, the superior longitudinal fasciculus, and the middle cerebellar peduncle.

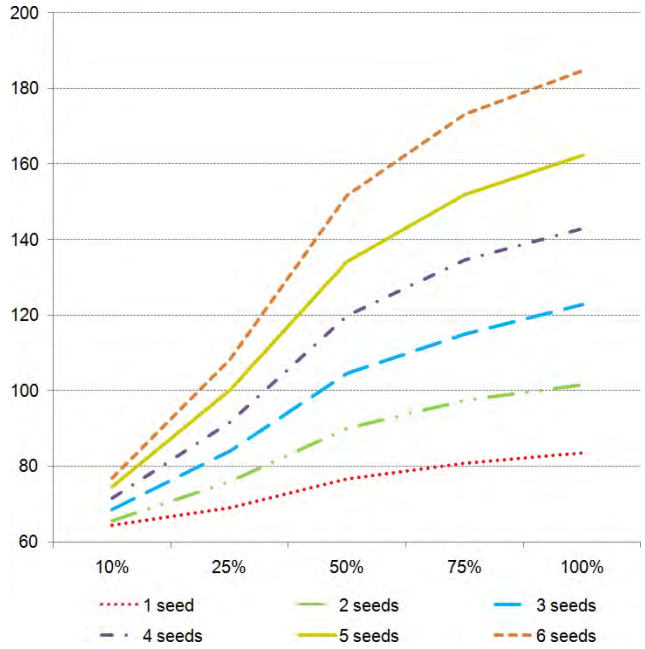

Figure 5.11: Computation time in seconds for creating the fiber tracks with the split and merge steps, considering different number of planes, and seeds, and taking into account the VOIs calculation time (average of 5 subjects)

of interest but define a region to place seeds in order to reconstruct the bundle of fibers corresponding to the structure. The defined VOIs are used to place seeds and we avoid seeding all the brain. This method is completely automatic and only requires the definition of some input parameters required by the split-and-merge process. This is an important feature of the approach since it ensures the reproducibility of the white matter reconstructions. We want to emphasize that the whole process requires less than a minute and hence reduces considerably the time spent with manual approaches. A limitation of the approach is the determination of the level of accuracy of the merging step. Although we can observe on-line the VOIs obtained by this step, the final selection depends on the user. In the case of the splitting phase, we have been able to propose a set of optimal values taking into account the gain of information and the computation time.

The approach has been tested on a DTI-brain atlas and real DTI data. The matching between the manual and automated approaches achieves the best results with the DTI-brain atlas. In this case, for all the structures, the best kappa is > 0.7 leading to a substantial and almost perfect agreement in some cases. For the structures that achieve an almost perfect agreement, the (planes, seeds) configuration is not the maximal one. This demonstrates that the proposed approach is capable of reproducing these structures with minimal user interaction. The worst results are achieved when the lowest (planes,seeds) configuration is applied. In this case, the kappa value is moderate. The results obtained with real DTI-data are not as satisfactory as the previous ones.

Matching is substantial for all the evaluated structures except for the corticospinal and the superior longitudinal fasciculus, which is moderate. If we compare the number of planes and seeds with the ones used for the DT-brain atlas, we observe that more seeds are needed. The worst results are achieved with the lowest seeding configuration (10%,1). The results obtained with real DTI-data would probably be improved with the pre-processing of input data [84] or the aplication of a regularization process [65, 173, 66].

Our approach considers *FA* and fiber direction to define the VOIs. The fact of considering direction, in some cases, leads to the definition of more than one VOI (i.e., superior longitudinal fasciculus or middle cerebellar peduncle) or a VOI containing only a part of the structure (i.e., inferior fronto-occipital fasciculus or corpus callosum). However, when planes and seeds are automatically placed, the structure is correctly created. This may be a limitation at the beginning since it will be difficult for the user to know if boolean operations have to be applied or not, or if the current VOI decomposition is the best one. However, this knowledge can be acquired by using the environment.

5.7 Conclusions

We have presented an automated approach for DTI tract reconstruction based on information-theoretic split-and-merge algorithm, that considers fractional anisotropy and fiber orientation information to automatically define volumes of interest (VOIs). For each VOI, a number of planes and seeds is automatically placed and, then, fiber bundles corresponding to the VOIs are created. Different experiments have been defined for setting, in a optimal way, the algorithms parameters required: MIR, for controlling the splitting phase, *the number of regions* that the phase has to return, and *the seeding rate* needed to reconstruct fiber bundles.

We have used a validation framework with atlas-based and real DTI data for testing the accuracy of obtained fiber bundles. For the DTI-atlas, a high level of agreement was found between the manual and automated approaches. In an ideal model, like a DTI-atlas, we have demonstrated that the proposed approach is capable of reproducing the majority of structures with minimal user interaction. We have also observed that the tracts found are almost perfect (kappa$>$ 0.8) and substantial (kappa$>$ 0.6). The results obtained with real DTI-data are not so satisfactory because only substantial agreement is achieved in most of the cases. However, these could be improved using a pre-processing step or a regularization method.

As a future work we will do a further study with real DTI-data considering more controls and also pre-processing techniques to improve the results. In addition, we aim to study the possibility of defining automatically the number of planes and seeds of each VOI by using information-theoretic measures.

CHAPTER 6

Software: DTIWeb

The development of software platforms and environments that can support medical image processing and visualization has become a wide work field. In this context, internet-based applications have opened a big range of opportunities in software development allowing developers and users to work together in a unique platform. However, despite the advantages provided by internet applications, in general, the tendency of medical image research laboratories is to implement its own software which is often only made available internally or to scientific collaborators. This situation is still more extreme when the software is designed to process a new image modality such as diffusion tensor imaging (DTI). In this chapter, we present DTIWeb, a robust, portable, and extensible Java application for visualizing and processing DTI data. The proposed framework is based on the Java3D programming platform that provides an object-oriented programming model and independence of both computer hardware configuration and operating system. The platform is designed to work through the world wide web and only requires a web browser.

6.1 Introduction

Although DTI is a valuable tool for diagnosis, the novelty and complexity of this image modality hinders its application in clinical practice. A good strategy to exploit DTI capabilities is the development of software in which engineers and practitioners combine their knowledge. Motivated by a common interest, the medical imaging group of our university and medical researchers from the Hospital Josep Trueta of Girona created a working group. We aimed to develop a tool that integrates the operations and tools required to diagnose from DTI data and also a tool that provides an environment where different visualization, processing, and evaluation techniques can be tested and compared. With this aim, DTIWeb has been designed.

The criteria used in the design of DTIWeb are the following:

- Portability: it facilitates the efficient creation of computational tools for DTI processing and visualization, independent of the operating systems.
- Reusability: the object toolkit design should follow the object-oriented principle, so that the object classes are self-encapsulated, with high cohesion and minimum coupling.
- Flexibility: the platform integrates object classes with reusability features.
- Extensibility: new modules could easily be incorporated into the platform.
- Usability: the platform needs a GUI interface, easy and clear to use.

To develop DTIWeb, we use the Java programming language. The motivation behind the choice of this language is that it supports multiple platforms and enables easy customization of them. Java also provides some packages that are very helpful in the development of image processing and visualization functions. The Java Virtual Machine (JVM) is a platform-specific program that interprets platform-independent Java software and allows Java code to run on different platforms without being recompiled. Java supports a rapid development and an easy customization of software with features such as automatic memory management, object oriented syntax, strong type checking and a protected runtime environment [58]. The Java3D [48] component provides a set of higher-level APIs compared to most graphic packages which many developers are still using, such as OpenGL [149]. In our case, this feature is of great interest in order to generate 3D visualizations.

This chapter has been structured as follows. Section 6.2 describes related work. Section 6.3 presents design decisions and implementation details. Finally, Section 6.4 presents the conclusions.

6.2 Related Work

In this section we review some of the most representative DTI data processing and visualization packages.

There are several medical imaging toolkits developed using Java, such us ImageJ [142], NeatVision [175], BIL-kit [71], BrainImageJ [183] and Camino [41]. There are also different medical imaging packages that support DTI data processing and visualization [68]. However, there are few Java toolkits for DTI data evaluation [120]. We briefly review some of the free fiber tractography and visualization software packages that have been proposed:

- 3DMRI [1], developed at the Laboratory of Brain Anatomical Imaging Johns Hopkins University, is a C++ application built on top of the Visualization Toolkit (VTK) to visualize fiber tracts. Fiber tracts are visualized inside an iso-surface of human brain generated from brain MRI scan. Users can change the transparency of the iso-surface and can assign colors and thickness to fiber tracks. Users can also choose to project the fibers to the brain cortex to estimate possible contact areas.

- *FiberViewer* and *FiberTracking* [57] are open source tools based on ITK [125], VTK, and SOViewer toolkits. The tools are designed to provide several interconnected modules to perform quantitative analysis of DTI data based on fiber tracts generated from tractography. Both are complemented by *DTIChecker* [52, 53], that is a tool to check and correct DTI data. Slice artifacts and motion artifacts between shots can be checked. It also creates the best average of different shots.

- *DoDTI* [92] is a software toolkit developed for the analysis and quantification of diffusion tensor imaging. It is implemented in Matlab.

- *dTV* [108], or *diffusion tensor visualizer*, is an extension of a program developed for the volume data view program VOLUME-ONE. dTV performs analysis of DTI data and transfers results to VOLUME-ONE for display.

- *DTIStudio* [78] is a program developed using C++ and OpenGL on a Windows platform. The software allows users to perform user DTI related calculations, fiber tracking and editing, and ROI analysis with 3D visualization.

- *DSIStudio* [181] is a software in C++ that includes reconstruction (DTI, QBI, DSI, and GQI), deterministic fiber tracking, and 3D visualization. It has a window-based interface and operates on Microsoft Windows system.

- *DipY* [75] is a free and open source software project for DTI analysis. It depends on a few standard libraries based on Python. With this software, user tractographies can be warped into another space finding track correspondence between different brains.

- *Teem* [87] is a software written in C. It has a group of low-level functions, that does not include a GUI, and that can be directly called from command-line for getting data in and out.

- *FSL* [176] is a cross-platform comprehensive library of analysis tools for FMRI, MRI and DTI brain imaging data. Most of the tools can be run from both the command line and as GUIs. *FSL* includes *FDT* package, that is a group of diffusion tools, *TBSS* for voxel-based analysis, and *ProbTrack* to perform probabilistic tracking.

- *MedINRIA* [53] is a free collection of software packages implemented in C++, ITK and VTK. It aims at providing to clinicians state-of-the-art algorithms dedicated to medical image processing and visualization, including DTI. Efforts have been made to simplify the user interface, while keeping high-level algorithms. Each application is called a module, and can be loaded dynamically from a single main window. *MedINRIA* is cross-platform.

- *Camino* [41] is a fully-featured toolkit for Diffusion MR processing and reconstruction, including diffusion tensor techniques, tractography and advanced algorithms for resolving non-Gaussian diffusion profiles, the so-called fiber-crossing problem. Camino is an open source object-oriented software package written entirely in Java.

- *Explore DTI* [101] is a non-commercial package that combines many of the key DTI tools: visualization of scalar and vector maps of various diffusion tensor properties, display of principal diffusion vectors, cuboids and ellipsoids with several color-encodings, deterministic and probabilistic fiber tractography, clustering of fiber tracts, data quality assessment tools for HARDI reconstructions (Q-ball and spherical deconvolution imaging), tract-specific measurements, tract-segment analysis, and motion/distortion correction.

- *TrackVis* [166] is a software tool that can visualize and analyze fiber track data from DTI, DSI, HARDI, and Q-Ball tractography. It is cross-platform. *TrackVis* handles large fiber track datasets and also performs intensive 3D rendering interactively, requiring a large system RAM and a high-performance 3D graphics card that are critical to achieving satisfying performance.

- *TracTor* (Tractography with R) [34] is a project that includes R packages for reading, writing and visualizing MRI. It also contains functions specifically designed for working with DTI and tractography, including a standard implementation of the neighborhood tractography approach to white matter tract segmentation.

- *Quantitative DTI* [103] is an independent platform tool programmed in C++ that provide a group of modules for quantitative diffusion analysis with Slicer3. Modules include tools for clustering fiber tracts, summarizing measures over tract clusters and point-by-point mapping of white matter fiber pathways.

- *DTI-TK* [115] is a spatial normalization and atlas construction toolkit, designed from ground up to support the manipulation of DTI with special care taken to respect the tensorial nature of the data. It implements a state-of-the-art registration

algorithm that drives the alignment of white matter (WM) tracts by matching the orientation of the underlying fiber bundle at each voxel. The algorithm has been shown to improve both WM tract alignment and to enhance the power of statistical inference in clinical settings. It has interoperability with other DTI tools: *Camino*, *DTIStudio*, and *FSL*.

- *CATNAP* (Coregistration, Adjustment, and Tensor-solving, a Nicely Automated Program) [94] is an end-to-end data processing pipeline for Philips MRI data files. *CATNAP* performs motion correction for both diffusion and structural images using *FSL FLIRT*, adjusts the diffusion gradient directions for scanner settings (i.e., slice angulation, slice orientation, etc.) and motion correction (i.e., the rotational component of the applied transformation), and computes tensor and derived quantities (*FA*, *MD*, colormaps, eigenvalues, etc.). The results are readily compatible with *DTIStudio*, *FSL*, and other tensor analysis packages.

- *BrainVoyager QX* [139] is a software package for the analysis and visualization of functional and structural MRI data sets. From version 1.9, this software has a DTI module allowing us to analyze diffusion-weighted MRI data including the calculation of *FA* maps, fiber tracking, and *FA* group comparisons. It has been completely programmed in *C++*, *Qt*, and *OpenGL*.

- *Saturn* [31] is built using the ITK image processing libraries, the VTK libraries for 3D visualization, and the Fast Light Toolkit (FLTK) libraries for the graphical user interface objects. *Saturn* is open source and written in C++. The main feature is that it includes a quantification method for DTI data, using an atlas-based method to automatically obtain equivalent anatomical fiber bundles and regions of interest among different DTI data sets.

- *DTI-Query* [4] is written entirely in C++ and is designed to work without any special hardware requirements. The program makes use of the visualization toolkit (VTK) for 3D scene generation and interaction. Specifically, the application allows neuroscientists to place and interactively manipulate box-shaped regions to selectively display pathways that pass through specific anatomical areas.

- *DTI & FiberTools* [91] is implemented under Matlab. This toolbox provides import-filters for several MR file standards, a processing unit to calculate the diffusion tensors, and several GUI-based tools to calculate fiber tracks and to evaluate the DTI dataset. The results can be filed as images with 3D impression or can be logged in formatted ASCII files. The toolbox is available upon request.

- *Slicer-DTMRI* [54] is the DTI module of community platform Slicer, or 3D Slicer. 3D Slicer is a free, open source software package for visualization and image analysis. 3D Slicer is natively designed to be available on multiple platforms.

- *SPM* [114] in the version 8 has a set of two toolboxes for DTI: The *FA-VBS normalization* toolbox is for preparing DTI data for VBM-style voxel-based statistics

(VBS) of *FA* images (FA-VBS). The *ECMOCO* toolbox is for correcting DTI data for motion and eddy current artefacts.

- *Nipype* [55] is an open source platform that helps to unify and replicate the interaction with existing neuroimaging tools.

We can see that the growing importance of DTI has been accompanied by the appearance of multiple software packages that help us to process DTI data. All of them have a visualization and a tracking module, and then we can find some more modules depending on the specialization level of software. Although there are some multiple platform software packages, there is no any software package that works via web. Another shortcoming is their poor usability. This is due to the fact that most of them are designed for research and not for use in daily clinical practice.

6.3 Platform Description

To describe the DTIWeb platform we are going to present the three different layers that compose it. These are represented in Figure 6.1 and described below.

1. The *Input/Output level* integrates all the modules required to read any kind of medical data, such as DICOM, NRRD, and also the modules required to transform the obtained results in different formats, such as JPG, EPS.

2. The *graphical user interface (GUI)* integrates all the modules required for interacting with the user. This layer integrates the functionalities required to show the images and results to the user.

3. The third layer is the *kernel* of the application which consists of different modules, each one designed to support a specific operation, such as visualization, tracking, clustering, seeding, synthetic data, statistical, segmentation, and registration.

The protocol that has to be applied to communicate the different layers depends on the user selected operation. A more detailed description of all these layers is given below.

6.3.1 Medical Data Input/Output Lawyer

One of the main difficulties, when dealing with medical data, is due to the existence of multiple data formats. Although Digital Imaging and Communications in Medicine (DICOM) [46] has become prevalent, there are still differences in file formats depending not only on the image modality but also on the manufacturers. To tackle this problem, we have created the input/output layer. This layer is composed of different modules each one designed to support a specific file format. The module has to read the data file and generates the voxel model that represents the information. In the case

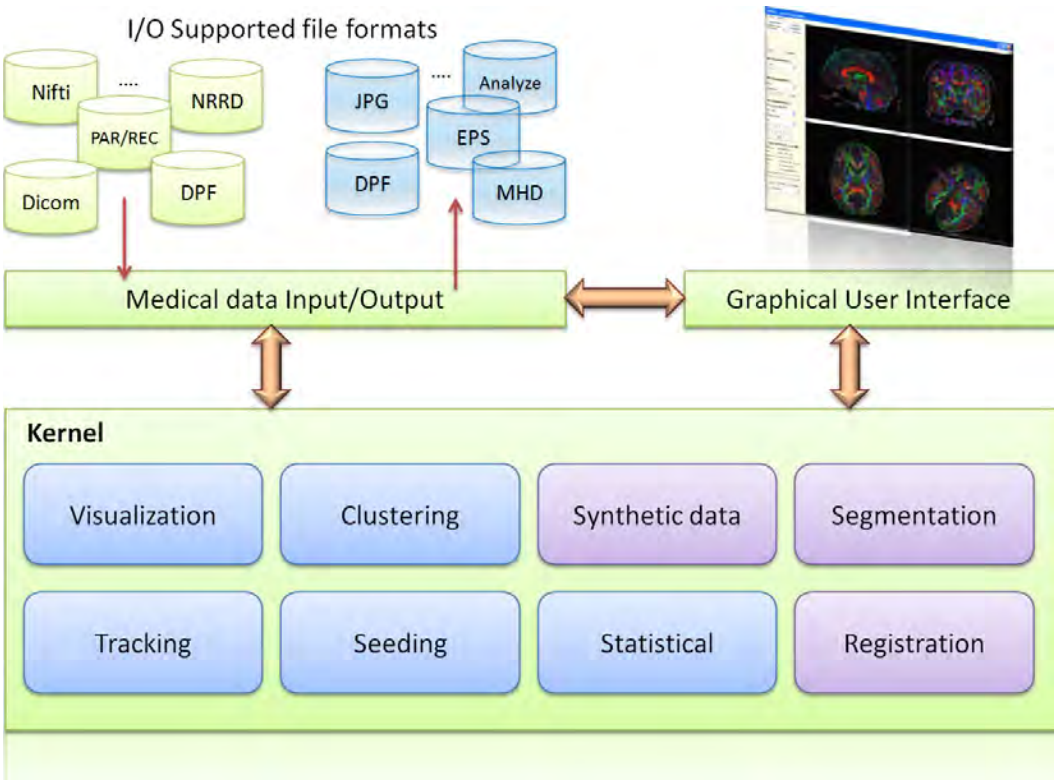

Figure 6.1: Structural design of the DTIWeb.

of DTI-data, this module reads DTI-data and computes the tensor that has to be stored in each voxel. DTIWeb implements the single tensor-based approach, and as a future work, we will incorporate an ODF-based approach. Currently, our system supports different input DTI formats (Philips file format, Bruker file format, DPF [78], NRRD [86], NIFTI [132], raw data and DICOM series) and also different MRI sequences.

DTIWeb also supports creation of output files. To maintain the information obtained from the applied visualization or processing techniques supported by the platform. For example, it can generate images in different formats, maintain the traces generated from a tract, the results obtained from a clustering process, the defined ROIs, etc. It also allows the creation of output files supported by other medical applications such as DPF [78], NRRD [86], MHD, DTI Studio Fiber [78], plain text file, and Analyze.

As shown in Figure 6.1, the medical data input/output layer interacts with the GUI and also with the kernel. The user through the GUI determines the file and the format of input and output files. The voxel model created by the Input/Output module is the main input parameter required by the different techniques integrated in the kernel of the application.

6.3.2 Graphical User Interface

The graphical user interface is composed of a menu bar, a tabbed panel, and a visualization area (see Figure 6.2). The *menu bar* is a list of menus where each menu contains a list of sub-menus. From left to right, the supported operations are *File*, which includes Open, Close, Save, and Snapshot functions; *Scene*, which is used to define regions of interest on the scene or to change the processed model in case more than one model is opened simultaneously; *Tracking*, which includes different configuration parameters and *Help*.

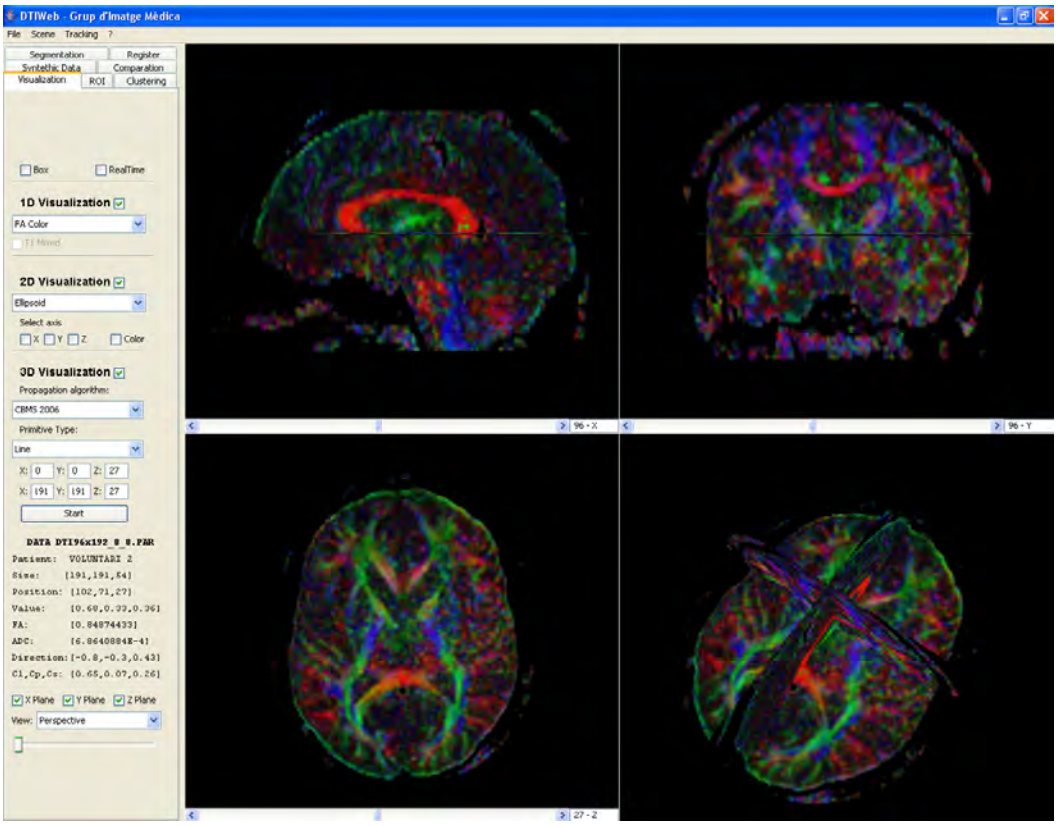

Figure 6.2: Main components of the graphical user interface.

The *tabbed panel*, positioned horizontally on the left, shows the operations that are in the kernel of the application. Each of the kernel modules has a panel, except seeding, to enter the parameters related with the selected operation.

The rest of the interface is the *visualization area* where DTI data is rendered. This area is split in four windows: the axial, coronal, and sagittal views of the model, and a 3D multiplanar view. Each of these windows has a slider that allows us to explore the entire DTI model in the corresponding view. Both orthographic and perspective projections are supported. Zoom and rotation operation can be performed in an independent way on each of the windows. Note that in the bottom of the tabbed panel, the

information of the point where the mouse is placed is collected. In Figure 6.2, we can see some information about the patient, model resolution, or the values of different parameters computed from the tensor, such as FA value, MD value, etc.

6.3.3 Kernel of the Platform

The kernel of the platform is composed of the main modules of the application. These modules are:

- **Visualization module**

  The visualization module integrates the methods and techniques designed to visualize data. Taking into account the state-of-the art on visualization (see Section 2.3) our platform supports:

  (i) 1D Visualization strategies which generate color or grey level scalar maps of a parameter computed from the tensor. The user enters the parameter to be rendered and the colors to be used. In Figures 6.3(a) and 6.3(b), two different scalar maps corresponding to the linear coefficient and fractional anisotropy indices are illustrated.

  (ii) 2D Visualization strategies which represent the information of the tensor by using tensor glyph. The user selects the glyph (cuboid or ellipsoid), the number of slices to be visualized, and the color scale. In Figures 6.3(c) and 6.3(d), two ellipsoid-based visualizations considering a single and three slices are illustrated.

  (iii) 3D Visualization strategies which render the tracts obtained from a tracking algorithm or from a clustering process. In this visualization, the user can select the background image and the color of the fibers. In Figures 6.3(e) and 6.3(f), visualizations of a tracking process with different background scalar maps are shown.

- **Tracking module**

  The tracking supports the main state-of-the art deterministic techniques (see Section 4.2.3). The implementation of the methods takes into account the main steps involved in the tracking process and allows to modify the different parameters. These are:

  (i) *Seeding strategies.* To place the seeds in the voxel we implemented different strategies: *Monte Carlo*, which places the seeds randomly in the voxel; *Traditional*, which places the seeds in the inferior edge of the voxel; *Random*, which is similar to *Monte Carlo*, but generates the same random seeds for each ROI; *Stratified*, which uses a stratified sampling to place seeds; *Systematic*, which uses a systematic sampling with a random offset. The user can choose to locate seeds in all the voxels or to define a ROI or VOI. The ROI

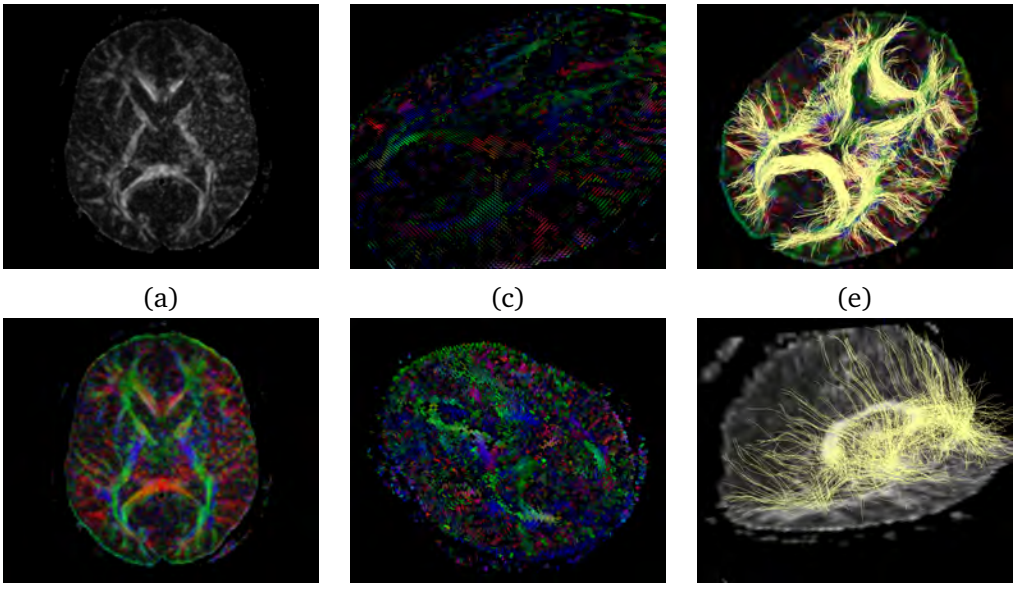

(a) (c) (e)

(b) (d) (f)

Figure 6.3: 1D visualization of (a) linear coefficient and (b) fractional anisotropy indices. 2D visualization using an ellipsoidic glyph considering (a) one slice and (b) three slices. 3D visualizations using as background (a) fractional anisotropy map and (b) fractional direction weighted by main direction color map.

can be defined manually, by drawing it on the image (see Figure 6.4(a)), or semi-automatically by selecting a drawing primitive and then placing the parameters required to define it. The user can also select the color of the ROI or VOI which is then used to draw the fibers. Our system supports boolean operations between different ROIs or VOIs. In Figures 6.4(b) and (c) we illustrate the tracks generated when different ROIs, R_1, R_2, and R_3, are defined and different boolean operations have been applied. The system has also the capability to store the entered ROI configuration in order to be applied in other models.

(ii) *Stop criteria.* The definition of the stopping criteria that determine when a tract finishes. Different parameters can be used for judging continuity, including minimal parameters such as *FA* and local curvature (angle difference between two consecutive vectors).

(iii) *Tracking technique.* Currently, our environment supports all the tracking algorithms presented in Section 4.2.3. To add a new method to this module, the user has to define the integration method, that given a tract point determines how the next one is computed, and the function that calculates the propagation direction at each point.

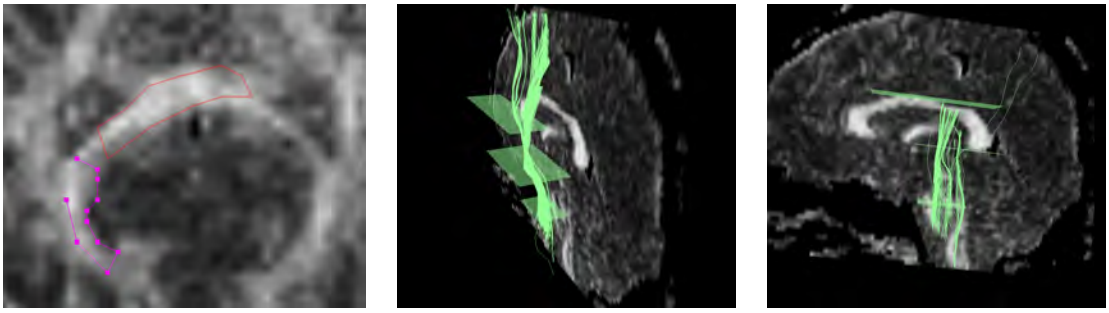

(a) (b) (c)

Figure 6.4: (a) ROI placed manually and tracking generated for different ROIs and different operations (b) (R_1 and R_2 and R_3), and (c) (R_1 and R_2 and (not R_3).

- **Clustering module**

  Despite the advantages of tracking algorithms with respect to 1D and 2D visualizations, its evaluation in clinical practice is quite difficult. The large amount of fibers reconstructed by tracking methods make their interpretation difficult (see Figure 6.5(a)). To overcome this limitation, different approaches have been proposed see Chapter 5. One of these strategies is clustering [73], which is supported by our platform (see Figure 6.5(b)). Fiber clustering methods analyze a collection of paths in 3D, and separate them into bundles, or clusters, that contain paths with similar shape and spatial position. These bundles are expected to contain fiber paths with similar anatomy and function. The clustering requires the definition of a similarity function that measures the distance between points or between fibers, and also the definition of a clustering strategy. We have implemented different distance functions and different clustering strategies in such a way that the user can combine them.

- **Statistical module**

  We have integrated into the platform a statistical module able to compute the main anisotropy indices that are used in medical diagnosis. To show these values, we can use a tabular mode or a graphical representation.

  In Figure 6.6, we show two FA-plots generated from DTI-data of an acute ischemic stroke patient. Images (a) and (c) correspond to data obtained within 12 hours from the onset of symptoms, and (b) and (d) 30 days after initial imaging. In both explorations, fibers of the corticospinal tract were generated bilaterally in order to compare the damaged side (left side) with the healthy one (right side). To start the tracking, we apply the ROIs manually placed in the basilar portion of an axial slice at lower pons, using the anatomical landmarks defined on color maps by Wanaka et al. [165]. A second target ROI was drawn in an upper axial slice near the cortex, specifically in the corona radiata at the level of the pre- and postcentral gyri. Only those trajectories passing through both

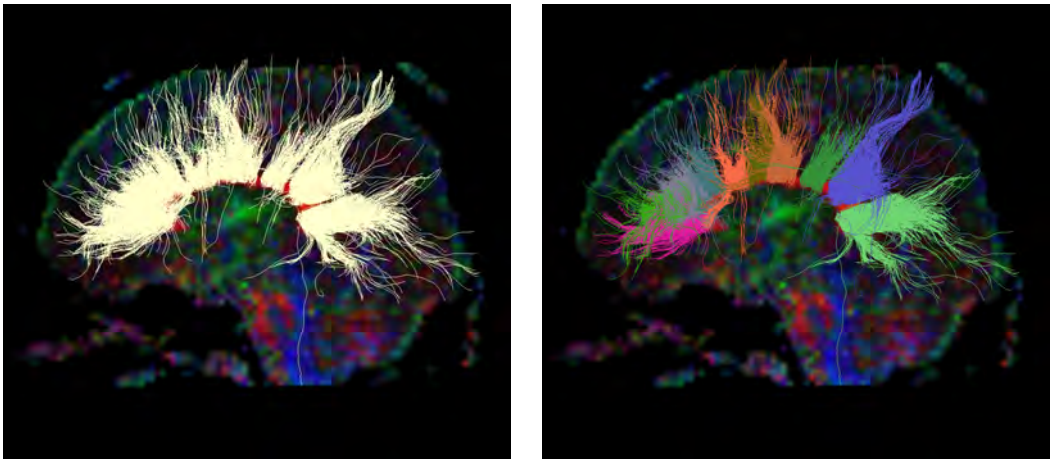

(a) (b)

Figure 6.5: Visualization of tracks (a) before and (b) after applying a clustering strategy.

regions were selected for the analysis. The tracts are terminated when *FA* is less than 0.2 or when the change in the direction is less than 70 degrees. To enhance comprehension, plots are colored with the same color as the fiber bundles.

- **Modules under development**

  Segmentation and registration modules are still in a development phase. We are also developing a synthetic data module to create and evaluate synthetic models.

6.4 Conclusions

We have designed and implemented DTIWeb, a modular framework for DTI data processing and visualization. The environment has been conceived to support different computer hardware configurations and operating systems, and to be accessed via web. The modularity of the platform allows for the integration of new functionalities with minimal effort.

An important part of our research have been the evaluation of DTIWeb in a real clinical environment. This process have been done in collaboration with medical doctors of our research group. We focus our work on acute stroke patients, and we evaluate how the proposed techniques implemented in DTIWeb could be used in the diagnosis of this pathology. This evaluation process has lead to different publications (see Chapter 7).

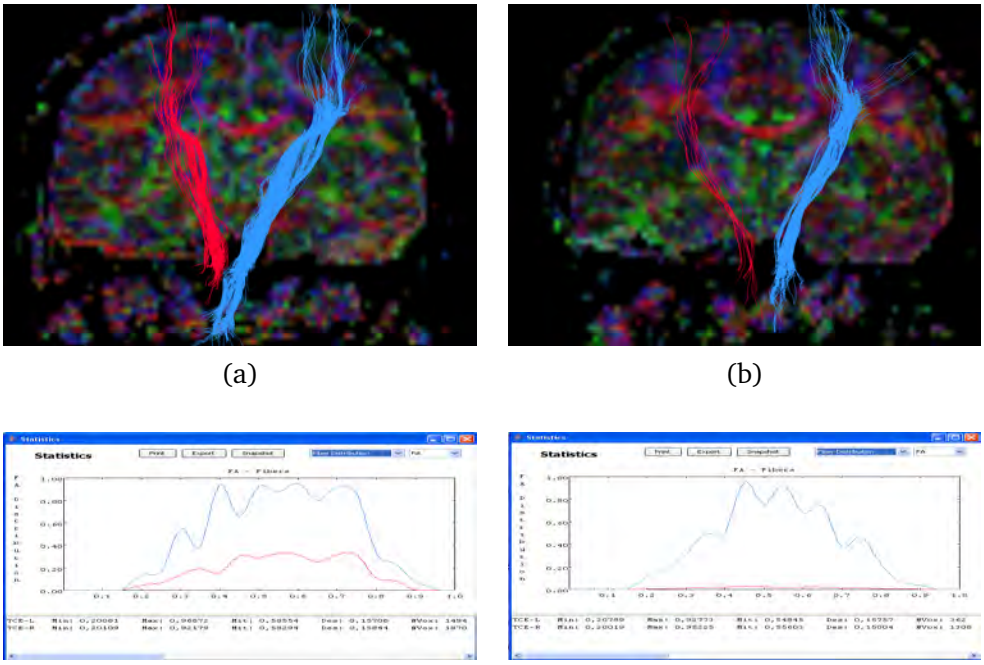

(a) (b)

(c) (d)

Figure 6.6: Corticospinal fiber tracts of an acute ischemic stroke patient. (a) and (c) correspond to data obtained within 12 hours of onset of symptoms, and, (b) and (d) 30 days after initial imaging. The plots represent the evolution of FA parameter along the fiber tracks.

CHAPTER 7

Conclusions

Diffusion tensor imaging (DTI) is an extension of conventional magnetic resonance imaging capable of characterizing the diffusion behavior of water in a tissue. The study of DTI and its visualization has become an emerging focus of research in brain studies since it provides the information required to reconstruct white matter fiber paths. Despite the potential of this new technology, there are still many factors that make its application in daily clinical practice difficult. Continuous progress is made in order to acquire data with more resolution, to reduce image acquisition time, to reduce noise and distortion effects, to improve DTI data visualization, or to validate DTI processing results.

In this thesis, we have focused our interest on techniques that reduce the information acquired by MR devices to a tensor per voxel. Specifically, we have studied how to visualize this tensor data in an effective manner to be applied in a real medical context. We have evaluated 1D visualization techniques with the idea to propose new anisotropy measures that provide new insight into the images. In addition, we have studied 3D visualization techniques. These are based on fiber tracking techniques that generate white matter fiber maps. Our aim has been the development of strategies that automate the generation of the fiber maps and also that make their interpretation easier. Finally, we have integrated all the proposed techniques in a common platform, denoted DTIWeb that has been used in a medical environment in the study of acute stroke pathology.

Below, we give a detailed description of the main contributions of the thesis as well as the publications related to each contribution.

7.1 Contributions

The main goal of this thesis has been the development of new visualization and processing of Diffusion Tensor MRI techniques that support and enhance computer aided diagnosis tools, and the main contributions have been in 1D and 3D visualization. These contributions can be summarized as follows:

- We have studied 1D anisotropy measures and we have proposed new measures derived from Hellinger divergences and from compositional data distances to evaluate diffusion anisotropy. The new anisotropy measures have been compared with classical ones and it has been seen that the proposed Kullback-Leibler Anisotropy (KLA) detects the transitions between white and grey matter more accurately. Moreover, it has been shown that KLA discriminates better in areas

with a greater confluence of fibers. Thus, the measure is a very promising index for different pathologies.

The work titled *Analysis of new diffusion tensor imaging anisotropy measures in the three-phase plot*, has been published in the Journal of Magnetic Resonance Imaging, 31(6):1435–1444, 2010.

- We have studied fiber tracking techniques and we have introduced a new Monte Carlo-based fiber tracking approach to estimate brain connectivity. One of the main characteristics of this line-propagation algorithm has been that all parameters are automatically determined at each point using the entropy of the eigenvalues of the diffusion tensor. The automaticity of the technique makes it suitable for use in medical contexts since it avoids user interaction.

  The work titled *A Monte Carlo-based Fiber Tracking Algorithm using Diffusion Tensor MRI*, has been published in the proceedings of the 19th IEEE Symposium on Computer-Based Medical Systems (CBMS'06), pages 353–358. IEEE, 2006.

- We have analyzed how to enhance fiber maps interpretation by grouping fibers in anatomical bundles. We have proposed a new approach to obtain automatically and rapidly bundles of fibers. This method is based on an information-theoretic split-and-merge algorithm that considers fractional anisotropy and fiber orientation information, to automatically define volumes of interest (VOIs). For each VOI, a number of planes and seeds is automatically placed and, then, fiber bundles corresponding to the VOIs are created.

  The work titled *Information-theoretical approach for automated white matter fiber tracts reconstruction*, has been submitted to the Journal of Neuroinformatics, 2011.

- We have developed DTIWeb, a software platform that integrates the methods and tools required to diagnose from DTI data. The main features of the proposed environment are portability, reusability, flexibility, and extensibility.

  The work titled *DTIWeb: A Web-based Framework for DTI data Visualization and Processing*, has been published in the Lecture Notes in computer science of the International Conference on Computational Science and its Applications (ICCSA 2007), 4706/2007:727–740, 2007. DTIWeb has been the first software application to win the Info-RESO award of the European Society for Magnetic Resonance in Medicine and Biology (ESMRMB), 2008.

- We have evaluated how proposed techniques can be used in a clinical environment in the context of the Hospital Universitari Doctor Josep Trueta of Girona and using DTIWeb. This evaluation process has led to different publications.

  Journal papers

  Diffusion tensor imaging, permanent pyramidal tract damage, and outcome in subcortical stroke. (Correspondence Letter) Journal: Neurology, published May

2011, 76(18) 1606-1607. Authors: S. Pedraza; J. Puig; G. Blasco; F. Prados; A. Thiel.

Acute damage to the posterior limb of the internal capsule on diffusion tensor tractography as an early image predictor of motor outcome after stroke. Journal: American Journal of Neuroradiology, published May 2011, 32(5) 857-863. Authors: J. Puig; S. Pedraza; G. Blasco; J. Daunis-i-Estadella; F. Prados; S. Remollo; A. Prats-Galino; G. Soria; I. Boada; J. Serena.

Wallerian Degeneration in the Corticospinal Tract Evaluated by Diffusion Tensor Imaging Correlates with Motor Deficit 30 Days after Middle Cerebral Artery Ischemic Stroke. Journal: American Journal of Neuroradiology, published March 2010, 31(7) 1324-1330. Authors: J. Puig; S. Pedraza; J. Daunis-i-Estadella; A. Prats-Galino; F. Prados; I. Boada; M. Castellanos; J. Sanchez-Gonzalez; S. Remollo; G. Lagunillo; A. M. Quiles; J. Serena.

Conference proceedings

Validation of FA as a promising imaging biomarker of motor outcome after stroke. Congress: International Stroke Conference 2010. San Antonio (Texas) (USA) 2010. Authors: J. Puig; G. Blasco; J. Daunis-i-Estadella; F. Prados; A. Prats-Galino; I. Boada; J. Sanchez-Gonzalez; M. Castellanos; J. Serena; S. Pedraza.

Wallerian Degeneration Imaging: Conventional MRI and Diffusion Tensor Imaging Findings. Congress: Radiological Society of North America 95th Scientific Assembly and Annual Meeting 2009. Authors: J. Puig; G. Blasco; F. Prados; A. Prats-Galino; I. Boada; S. Pedraza.

Diffusion Tensor Imaging and Fiber Tractography in Stroke: Technique, Imaging Postprocessing, and Clinical Applications. Congress: Radiological Society of North America 95th Scientific Assembly and Annual Meeting 2009. Authors: J. Puig; G. Blasco; F. Prados; A. Prats-Galino; I. Boada; S. Pedraza.

Corticospinal tract damage correlates with clinical motor deficit in the chronic phase of middle cerebral artery ischemic stroke patients. Congress: International Stroke Conference. San Diego, California. 17-20 February 2009. Authors: J. Puig; G. Blasco; J. Daunis-i-Estadella; F. Prados; A. Prats-Galino; I. Boada; J. Sanchez-Gonzalez; M. Castellanos; J. Serena; S. Remollo; G. Laguillo; E. Gomez; A. Quiles; S. Pedraza.

Estudi de la substància blanca cerebral mitjançant tensor de difusió per RM: aspectes tècnics i aplicacions clíniques. Congress: III Congres Nacional de Radiòlegs de Catalunya, Sitges 2009. Authors: J. Puig; G. Blasco; J. Daunis-i-Estadella; F. Prados; A. Prats-Galino; S. Pedraza.

Valoració del dany del tracte corticoespinal mitjançant tensor de difusió en pacients amb infart cerebral. Congress: Cloenda de Ciències Mèdiques de Catalunya, Girona 2009. Authors: J. Puig; G. Blasco; J. Daunis-i-Estadella; F. Prados; I. Boada; A. Prats-Galino; S. Remollo, G. Laguillo, A. Quiles, E. Gómez, M. Castellanos, J. Serena, S. Pedraza.

Tensor de Difusió per RM: Aspectes tècnics i aplicacions clíniques. Congress: Cloenda de Ciències Mèdiques de Catalunya, Girona 2009. Authors: J. Puig; G. Blasco; J. Daunis-i-Estadella; F. Prados; I. Boada; A. Prats-Galino; S. Remollo, G. Laguillo, A. Quiles, E. Gómez, M. Castellanos, J. Serena, S. Pedraza.

Development of a 3D DTI-Based Atlas of Human Brain White Matter. Congress: XXIV Congreso de la SAE, Bilbao 2009. Authors: A. Prats-Galino; M. De Notaris; K. Palma; J. Juanes; J. Puig; G. Blasco; F. Prados; I. Boada; S. Pedraza.

Utilidad clínica de la difusión tensor en la valoración de la evolución clínica de pacientes con infarto cerebral agudo. Congress: XXIX Congreso Nacional de la Sociedad Española de Radiología Médica. Sevilla, 23 - 26 May 2008. Authors: S. Pedraza; J. Puig; G. Blasco; F. Prados; M. Castellanos; A. Prats.

La afectación de la cápsula interna como factor pronóstico de mala evolución funcional motora en pacientes con infarto cerebral agudo. Congress: XXXVII Reunión Anual de la Sociedad Española de Neuroradiología. Oviedo, 30 October - 1 November 2008. Authors: J. Puig; G. Blasco; F. Prados; J. Daunis-i-Estadella; I. Boada; A. Prats-Galino; S. Pedraza.

7.2 Future work

Our future work will be focused on the following research lines:

- Study the application of KLA in other phases of DTI processing. The good performance of KLA measure encourages us to use it in the fiber tracking pipeline, for instance, to define new seeding and stopping criteria. Moreover, we want to study the application of KLA as a new imaging biomarker of motor outcome after strokes, as an alternative or to complement FA.

- Define a complete automatic tracking technique. Our proposed approach automate most of the processes required by tracking techniques, however there are still some parameters that can be tuned by the use, such as the number of seeds per voxel or the number of planes per volume of interest. Our purpose is to extend the method and use information theory tools to define these parameters automatically using measures such as mutual information or entropy.

- Define new clustering techniques based on information theory tools. Information theory tools can be used to compute the similarity between fibers. Different strategies based on the minimization of mutual information loss of the connectivity channel or the use of Jensen-Shannon divergence will be applied to obtain efficient clustering algorithms.

- Study the application of multiresolution and level of detail strategies to optimize the performance of DTI visualization techniques. The idea is to exploit the coherence of the images to simplify the computations required to obtain the fibers.

APPENDIX A

Abbreviations and Notation

δ	Duration of the diffusion
γ	Gyromagnetic ratio
ε_n	Independent standard normal random vector
λ	Eigenvalue
$\langle\lambda\rangle$	Mean diffusivity
μ	Step size
σ	Intensity of artificial noise
AA	Angular anisotropy
ADC	Apparent diffusion coefficient
$AitA$	Aitchison anisotropy
b	Diffusion-weighting factor
CA	Component anisotropic index
Cl	Linear anisotropy coefficient
Cp	Planar anisotropy coefficient
Cs	Spherical anisotropy coefficient
CSF	Cerebrospinal fluid
CT	Computed tomography
$\mathbf{D}$	Diffusion tensor matrix
DICOM	Digital imaging and communications in medicine
DOT	Diffusion orientation transform
DSI	Diffusion spectrum imaging
DTI	Diffusion tensor imaging
DWI	Diffusion weighted imaging
e_i	Eigenvector
FA	Fractional anisotropy
g	Normalized diffusion sensitizing gradient vector
G	Amplitude of the diffusion
$H(x)$	Shannon entropy of a discrete random variable X
HARDI	High angular resolution diffusion imaging
IT	Information Theory
KLA	Kullback-Leibler anisotropy
LA	Logaritmic anisotropy
MA	Matusita anisotropy

MRI	Magnetic resonance image
ODF	Orientation density function
PAS	Persistent angular structure
PDF	Probability distribution function
QBI	Q-ball imaging
RA	Relative anisotropy
RGB	Red - Green - Blue color space
r_n	A random vector uniformly distributed over a unit sphere
S	Observed echo signal intensity
S_E	End points distance
SD	Spherical deconvolution
SPECT	Single photon emission computed tomography
$\vec{v}_{in}$	Incoming vector direction
$\vec{v}_{out}$	Next vector direction
VR	Volume ratio
TR	Repetition time
TE	Echo time

Bibliography

[1] 3DMRI. http://cmrm.med.jhmi.edu/DTIuser/DTIuser.asp, Johns Hopkins University. (Cited on page 103.)

[2] J. Aitchison. *The statistical analysis of compositional data*. Chapman and Hall, London. Reprinted in 2003 by Blackburn Press, 1986. (Cited on pages 36 and 39.)

[3] J. Aitchison, C. Barceló-Vidal, J. Martín-Fernández, and V. Pawlowsky-Glahn. Logratio analysis and compositional distance. *Mathematical Geology*, 32(3): 271–275, 2001. (Cited on pages 36 and 41.)

[4] D. Akers, A. Sherbondy, R. Mackenzie, R. Dougherty, and B. Wandell. Exploration of the brain's white matter pathways with dynamic queries. *IEEE Visualization 2004*, pages 377–384. (Cited on page 105.)

[5] A. L. Alexander. Synthetic twisting helix. http://www.sci.utah.edu/∼ gk/DTI-data/, 2000. (Cited on page 66.)

[6] A. L. Alexander, K. M. Hasan, G. L. Kindlmann, D. L. Parker, and J. S. Tsuruda. A geometric analysis of diffusion tensor measurements of the human brain. *Magnetic Resonance in Medicine*, 44(2):283–291, 2000. (Cited on pages 36, 40, 41, 44, 53 and 86.)

[7] A. L. Alexander, K. M. Hasan, M. Lazar, J. S. Tsuruda, and D. L. Parker. Analysis of partial volume effects in diffusion-tensor MRI. *Magnetic Resonance in Medicine*, 45(5):770–780, 2001. (Cited on pages 23 and 56.)

[8] D. C. Alexander and G. J. Barker. Optimal imaging parameters for fiber-orientation estimation in diffusion MRI. *NeuroImage*, 27(2):357–67, Aug. 2005. (Cited on page 25.)

[9] A. W. Anderson. Theoretical analysis of the effects of noise on diffusion tensor imaging. *Magnetic Resonance*, 46:1174–1188, 2001. (Cited on page 25.)

[10] H. Ardon, S. Sunaert, D. Peuskens, J. Goffin, and J. V. Loon. Correlation between fiber dissection and diffusion tensor imaging of the anterior temporal lobe and the frontotemporal region. Technical report, 2009. 1–4 pp. (Cited on page 66.)

[11] J. Ashburner. SPM5 Manual, 2007. Functional Imaging Laboratory, Wellcome Trust Centre for Neuroimaging. (Cited on pages 46 and 88.)

[12] H.-E. Assemlal, D. Tschumperlé, L. Brun, and K. Siddiqi. Recent advances in diffusion MRI modeling: angular and radial reconstruction. *Medical image analysis*, 15(4):369–96, Aug. 2011. (Cited on pages 12, 14, 16 and 25.)

[13] A. Bardera. *New medical image registration and segmentation techniques using information theory tools*. PhD thesis, University of Girona, Catalonia, Spain, 2008. (Cited on page 2.)

[14] P. J. Basser. Inferring microstructural features and the physiological state of tissues from diffusion-weighted images. *NMR in Biomedicine*, 8(7):333–344, 1995. (Cited on pages 17, 18 and 38.)

[15] P. J. Basser. Relationships between diffusion tensor and q-space MRI. *Magnetic Resonance in Medicine*, 47(2):392–397, 2002. (Cited on page 14.)

[16] P. J. Basser, J. Mattiello, and D. Le Bihan. Estimation of the effective self-diffusion tensor from the NMR spin echo. *Journal of magnetic resonance Series B*, 103(3):247–254, 1994. (Cited on pages 1, 6, 9, 12, 16 and 37.)

[17] P. J. Basser, J. Mattiello, and D. Le Bihan. MR diffusion tensor spectroscopy and imaging. *Biophysical journal*, 66(1):259–67, 1994. (Cited on pages 1, 6, 17, 18 and 38.)

[18] P. J. Basser, S. Pajevic, C. Pierpaoli, J. Duda, and A. Aldroubi. In vivo fiber tractography using DT-MRI data. *Magnetic Resonance in Medicine*, 44(4):625–632, 2000. (Cited on pages 22 and 59.)

[19] P. J. Basser and C. Pierpaoli. Microstructural and physiological features of tissues elucidated by quantitative-diffusion-tensor MRI. *Journal of magnetic resonance Series B*, 111(3):209–219, 1996. (Cited on pages 10, 17, 36, 38 and 41.)

[20] T. E. J. Behrens, H. J. Berg, S. Jbabdi, M. F. S. Rushworth, and M. W. Woolrich. Probabilistic diffusion tractography with multiple fibre orientations: What can we gain? *NeuroImage*, 34(1):144–55, Jan. 2007. (Cited on pages 23 and 60.)

[21] T. E. J. Behrens, H. Johansen-Berg, M. W. Woolrich, S. M. Smith, C. A. M. Wheeler-Kingshott, P. a. Boulby, G. J. Barker, E. L. Sillery, K. Sheehan, O. Ciccarelli, A. Thompson, J. M. Brady, and P. M. Matthews. Non-invasive mapping of connections between human thalamus and cortex using diffusion imaging. *Nature neuroscience*, 6(7):750–7, July 2003. (Cited on page 24.)

[22] T. E. J. Behrens, M. W. Woolrich, M. Jenkinson, H. Johansen-Berg, R. G. Nunes, S. Clare, P. M. Matthews, J. M. Brady, and S. M. Smith. Characterization and propagation of uncertainty in diffusion-weighted MR imaging. *Magnetic Resonance in Medicine*, 50:1077–1088, 2003. (Cited on pages 23 and 60.)

[23] G. Berenschot. Visualization of diffusion tensor imaging, 2003. Master's Thesis - Eindhoven. (Cited on page 26.)

[24] B. Bernal and N. Altman. The connectivity of the superior longitudinal fasciculus: a tractography DTI study. *Magnetic Resonance Imaging*, 28(2):217–25, Feb. 2010. (Cited on pages 70 and 89.)

[25] M. Björnemo, A. Brun, R. Kikinis, and C.-F. Westin. Regularized stochastic white matter tractography using diffusion tensor MRI. In *International Conference on Medical Image Computing and Computer-Assisted Intervention (MICCAI'02)*, pages 435–442, Tokyo, Japan, 2002. (Cited on pages 23, 56, 60, 61 and 64.)

[26] A. Brun, M. Björnemo, R. Kikinis, and C.-F. Westin. Clustering fiber tracts using normalized cuts. In *International Conference on Medical Image Computing and Computer-Assisted Intervention (MICCAI'04)*, Lecture Notes in Computer Science, pages 368–375, Rennes - Saint Malo, France, September 2004. (Cited on pages 24, 26 and 82.)

[27] A. Brun, H.-J. Park, H. Knutsson, and C.-F. Westin. Coloring of DT-MRI fiber traces using laplacian eigenmaps. In *Computer Aided Systems Theory (EUROCAST'03), Lecture Notes in Computer Science 2809*, pages 564–572, Las Palmas de Gran Canaria, Spain, February 24–28 2003. Springer Verlag. (Cited on page 24.)

[28] J. Burbea and C. R. Rao. On the convexity of some divergence measures based on entropy functions. *IEEE Transactions on Information Theory*, 28(3):489–495, May 1982. (Cited on page 31.)

[29] R. L. Burden and J. D. Faires. *Numerical Analysis 6.ed.* Brooks/Cole Publishing, 1997. (Cited on page 58.)

[30] J. S. W. Campbell, P. Savadjiev, K. Siddiqi, and G. B. Pike. Validation and regularization in diffusion MRI tractography. *3rd IEEE International Symposium on Biomedical Imaging: Macro to Nano, 2006.*, pages 351–354, 2006. (Cited on page 66.)

[31] R. Cardenes, E. Munoz-Moreno, A. Tristan-Vega, and M. Martin-Fernandez. Saturn: a software application of tensor utilities for research in neuroimaging. *Computer Methods and Programs in Biomedicine*, 97(3):264–279, 2010. (Cited on page 105.)

[32] M. Catani, R. J. Howard, S. Pajevic, and D. K. Jones. Virtual in vivo interactive dissection of white matter fasciculi in the human brain. *NeuroImage*, 17:77–79, 2002. (Cited on pages 24, 67 and 89.)

[33] H.-W. Chung, M.-C. Chou, and C.-Y. Chen. Principles and limitations of computational algorithms in clinical diffusion Tensor MR tractography. *AJNR. American Journal of Neuroradiology*, pages 3–13, Mar. 2010. (Cited on pages 23, 25, 26 and 66.)

[34] J. Clayden, S. Muñoz Maniega, A. Storkey, M. King, B. M.E., and C. Clark. TractoR: magnetic resonance imaging and tractography with R. *Journal of Statistical Software*, In press. (Cited on page 104.)

[35] J. D. Clayden. *Comparative analysis of connection and disconnection in the human brain using diffusion MRI: new methods and applications*. PhD thesis, University of Edinburgh, 2008. (Cited on pages 23 and 24.)

[36] J. D. Clayden, A. J. Storkey, and M. E. Bastin. A comparison of seeding strategies for group tractography. In *Proceedings 16th Scientific Meeting International Society for Magnetic Resonance in Medicine (2008)*, page 1839, 2008. (Cited on pages 23 and 24.)

[37] J. Cohen-Adad, H. Benali, R. D. Hoge, and S. Rossignol. In vivo DTI of the healthy and injured cat spinal cord at high spatial and angular resolution. *NeuroImage*, 40(2):685–97, Apr. 2008. (Cited on pages 24 and 83.)

[38] L. Concha, D. W. Gross, and C. Beaulieu. Diffusion tensor tractography of the limbic system. *AJNR. American Journal of Neuroradiology*, 26(9):2267–74, Oct. 2005. (Cited on page 72.)

[39] T. E. Conturo, N. F. Lori, T. S. Cull, E. Akbudak, A. Z. Snyder, J. S. Shimony, R. C. Mckinstry, H. Burton, and M. E. Raichle. Tracking neuronal fiber pathways in the living human brain. *Magnetic Resonance in Medicine*, 35:399–412, 1999. (Cited on pages 23, 36, 37, 59, 64 and 89.)

[40] T. E. Conturo, R. C. McKinstry, J. A. Aronovitz, and J. J. Neil. Diffusion MRI: precision, accuracy and flow effects. *NMR in Biomedicine*, 8(7-8):307–332, 1995. (Cited on page 25.)

[41] P. Cook, Y. Bai, and S. Nedjati-Gilani. Camino: Open-source diffusion-MRI reconstruction and processing. In *14th Scientific Meeting of the International Society for Magnetic Resonance in Medicine*, volume 14, page 2759, 2006. (Cited on pages 103 and 104.)

[42] I. Corouge, S. Gouttard, and G. Gerig. Towards a shape model of white matter fiber bundles using diffusion tensor MRI. In *IEEE 2004 International Symposium on Biomedical Imaging (ISBI 2004)*, pages 344–347, 2004. (Cited on pages 24 and 82.)

[43] T. M. Cover and J. A. Thomas. *Elements of Information Theory*. John Wiley and Sons, Inc., 1991. (Cited on pages 2, 26, 30, 31, 63 and 84.)

[44] S. Deoni. Phantom images for simulating tractography errors. http://cubric.psych.cf.ac.uk/commondti/, 2005. (Cited on page 66.)

[45] I. S. Dhillon, S. Mallela, and D. S. Modha. Information-theoretic co-clustering. In *Proceedings of The 9th ACM SIGKDD International Conference on Knowledge Discovery and Data Mining (KDD-2003)*, pages 89–98, New York (NY), USA, 2003. ACM Press. (Cited on page 33.)

[46] DICOM. The Dicom Standard. National Electrical Manufactures Association. http://medical.nema.org. (Cited on page 106.)

[47] Z. Ding, J. Gore, and A. Anderson. Case study: reconstruction, visualization and quantification of neuronal fiber pathways. In *In IEEE Visualization'01, Conf. Proc.*, pages 453—456, 2001. (Cited on page 24.)

[48] D.Selman. *Java3D Programming*. Greenwich CT: Manning Publications Co, 2000. (Cited on page 102.)

[49] T. B. Dyrby, L. V. Sø gaard, G. J. M. Parker, D. C. Alexander, N. M. Lind, W. F. C. Baaré, A. Hay-Schmidt, N. Eriksen, B. Pakkenberg, O. B. Paulson, and J. Jelsing. Validation of in vitro probabilistic tractography. *NeuroImage*, 37(4):1267–77, Oct. 2007. (Cited on page 66.)

[50] B. Ebrahimi, S. P. Nejad Davarani, G. Ding, Q. Jiang, and T. E. Chupp. A microfabricated phantom for diffusion tensor imaging. In *Proceedings SPIE 7626*, volume 7626, pages 76261Q–76261Q–8, 2010. (Cited on page 66.)

[51] L. Ertöz, M. Steinbach, and V. Kumar. Finding clusters of different sizes, shapes, and densities in noisy, high dimensional data. In *Third SIAM International Conference on Data Mining*, 2003. (Cited on page 24.)

[52] P. Fillard and G. Gerig. Analysis tool for diffusion tensor MRI. In *International Conference on Medical Image Computing and Computer Assisted Intervention, (MICCAI'03)*, number 2879 in Lecture Notes in Computer Science, pages 967–968, 2003. (Cited on page 103.)

[53] P. Fillard, N. Toussaint, and X. Pennec. Medinria: DTI-MRI processing and visualization software. In *Similar NoE Tensor Workshop*, pages 1–12, November 2006. (Cited on pages 103 and 104.)

[54] N. A. for Medical Image Computing. DTMRI module for slicer, 2011. http://www.na-mic.org/Wiki/index.php. (Cited on page 105.)

[55] S. Ghosh, C. Burns, D. Clark, K. Gorgolewski, Y. Halchenko, C. Madison, R. Tungaraza, and K. J. Millman. Nipype: opensource platform for unified and replicable interaction with existing neuroimaging tools. In *16th Annual Meeting of the Organization for Human Brain Mapping*, 2010. (Cited on page 106.)

[56] J. Gillard, A. Waldman, and P. Baker. *Clinical MR neuroimaging: diffusion, perfusion and spectroscopy*. Cambridge University Press, Cambridge, UK, 2005. (Cited on page 25.)

[57] C. Goodlett, I. Corouge, M. Jomier, and G. Gerig. A quantitative DTI fiber tract analysis suite. In *Med Image Comput Comput Assist Interv. MICCAI 2005*, pages 1–5, 2005. (Cited on page 103.)

[58] J. Gosling, B. Joy, and G. Steele. *The Java language specification*. Reading Mass Addison Wesley, 1996. (Cited on page 102.)

[59] C. Gössl, L. Fahrmeir, B. Pütz, L. M. Auer, and D. P. Auer. Fiber tracking from DTI using linear state space models: detectability of the pyramidal tract. *NeuroImage*, 16(2):378–88, June 2002. (Cited on page 66.)

[60] M. Guye, G. J. M. Parker, M. Symms, P. Boulby, C. A. M. Wheeler-Kingshott, A. Salek-Haddadi, G. J. Barker, and J. S. Duncan. Combined functional MRI and tractography to demonstrate the connectivity of the human primary motor cortex in vivo. *NeuroImage*, 19(4):1349–1360, July 2003. (Cited on page 67.)

[61] T. A. Hackett, G. Karmos, C. E. Schroeder, I. Ulbert, S. J. Sterbing-D'Angelo, W. R. D'Angelo, Y. Kajikawa, S. Blumell, and L. De La Mothe. Neurosurgical access to cortical areas in the lateral fissure of primates. *Journal of Neuroscience Methods*, 141(1):103–113, 2005. (Cited on page 6.)

[62] P. Hagmann, L. Jonasson, P. Maeder, J.-P. Thiran, V. J. Wedeen, and R. Meuli. Understanding diffusion MR imaging techniques: from scalar diffusion-weighted imaging to diffusion tensor imaging and beyond. *RadioGraphics*, 26:205–223, 2006. (Cited on pages 16 and 23.)

[63] P. Hagmann, J. Thiran, X. Gigandet, L. Cammoun, and R. Meuli. Fast-marching tractography for connection matrix (Fast-TraC). In *Proceedings 16th Scientific Meeting International Society for Magnetic Resonance in Medicine*, page 1848, 2008. (Cited on page 23.)

[64] P. Hagmann, J. P. Thiran, L. Jonasson, P. Vandergheynst, S. Clarke, P. Maeder, and R. Meuli. DTI mapping of human brain connectivity: statistical fibre tracking and virtual dissection. *NeuroImage*, 19(3):545–554, July 2003. (Cited on pages 23, 56, 60, 61 and 64.)

[65] K. Hahn, S. Prigarin, and B. Pütz. Regularization and tracking for diffusion tensor imaging. *NeuroImage*, (6), 2001. (Cited on page 100.)

[66] K. Hahn, S. Prigarin, and B. Pütz. Spatial smoothing for diffusion tensor imaging with low signal to noise ratios, 2003. Discussion Paper 358, SFB 386, 2003, Ludwig-Maximilians-Universität München. (Cited on pages 25 and 100.)

[67] K. Hahn, S. M. Prigarin, S. Heim, and K. M. Hasan. Random noise in diffusion tensor imaging, its destructive impact and some corrections. 459:545–554, 2004. (Cited on page 25.)

[68] K. M. Hasan, I. S. Walimuni, H. Abid, and K. Hahn. A review of diffusion tensor magnetic resonance imaging computational methods and software tools. *Computers in biology and medicine*, pages 1–11, Nov. 2010. (Cited on page 103.)

[69] S. Hofer and J. Frahm. Topography of the human corpus callosum revisited–comprehensive fiber tractography using diffusion tensor magnetic resonance imaging. *NeuroImage*, 32(3):989–94, Sept. 2006. (Cited on page 72.)

[70] A. Holodny, D. M. Gor, R. Watts, P. H. Gutin, and A. M. UluÄŸ. Diffusion-tensor MR tractography of somatotopic organization of corticospinal tracts in the internal capsule: initial anatomic results in contradistinction to prior reports. *Radiology*, 234(3):649–653, 2005. (Cited on page 88.)

[71] S. Hunag, R. Baimouratov, P. Xiao, A.Anantasubramaniam, and W. Novinski. A medical imaging and visualization toolkit in Java. *Journal of Digital Imaging*, 19:17–29, 2006. (Cited on page 103.)

[72] A. K. Jain and R. C. Dubes. *Algorithms for clustering data*. Prentice Hall, 1988. (Cited on page 25.)

[73] A. K. Jain, M. N. Murty, and P. J. Flynn. Data clustering: a review. *ACM Computing Surveys*, 31(3):264–323, 1999. (Cited on pages 25 and 111.)

[74] K. M. Jansons and D. C. Alexander. Persistent angular structure: new insights from diffusion MRI data. *Inverse Problems*, 19:1031–1046, July 2003. (Cited on pages 15, 16 and 23.)

[75] K. Jarrod Millman and M. Brett. Analysis of functional magnetic resonance imaging in Python. *Computing in Science and Engineering*, 9(3):52–55, June 2007. (Cited on page 103.)

[76] S. Jbabdi, P. Bellec, R. Toro, J. Daunizeau, M. Pélégrini-Issac, and H. Benali. Accurate anisotropic fast marching for diffusion-based geodesic tractography. *International Journal of Biomedical Imaging*, 2008:320195, 2008. (Cited on page 23.)

[77] P. Jezzard, A. S. Barnett, and C. Pierpaoli. Characterization of and correction for eddy current artifacts in echo planar diffusion imaging. *Magnetic resonance in medicine*, 39(5):801–12, 1998. (Cited on page 25.)

[78] H. Jiang, P. C. M. van Zijl, J. Kim, G. D. Pearlson, and S. Mori. DTIStudio: Resource program for diffusion tensor computation and fiber bundle tracking. *Computer Methods and Programs in Biomedicine*, 81:106–116, February 2006. (Cited on pages 103 and 107.)

[79] R. Jianu, C. Demiralp, and D. H. Laidlaw. Exploring 3D DTI fiber tracts with linked 2D representations. *IEEE transactions on visualization and computer graphics*, 15(6):1449–56, 2009. (Cited on page 82.)

[80] B. Jobard and W. Lefer. Creating evenly spaced streamlines of arbitrary density. In *Eurographics Workshop in Boulogne-sur-Mer (Visualization in Scientific Computing '97*, 1997. (Cited on page 83.)

[81] H. Johansen-Berg and T. E. J. Behrens. *Diffusion MRI: from quantitative measurement to in-vivo neuroanatomy*. Academic Press, 2009. (Cited on pages 15 and 16.)

[82] H. Johansen-Berg, T. E. J. Behrens, E. Sillery, O. Ciccarelli, A. J. Thompson, S. M. Smith, and P. M. Matthews. Functional-anatomical validation and individual variation of diffusion tractography-based segmentation of the human thalamus. *Cerebral cortex*, 15(1):31–39, Jan. 2005. (Cited on page 67.)

[83] L. Jonasson, P. Hagmann, J.-P. Thiran, and V. J. Wedeen. Fiber tracts of high angular resolution diffusion MRI are easily segmented with spectral clustering. *International Society for Magnetic Resonance in Medicine*, 24(9):1127–1137, 2005. (Cited on page 82.)

[84] D. K. Jones and M. Cercignani. Twenty-five pitfalls in the analysis of diffusion MRI data. *NMR in Biomedicine*, 23(7):803–820, 2010. (Cited on pages 25 and 100.)

[85] R. A. Kanaan, S. S. Shergill, G. J. Barker, M. Catani, V. W. Ng, R. J. Howard, P. K. McGuire, and D. K. Jones. Tract-specific anisotropy measurements in diffusion tensor imaging. *Psychiatry Research*, 146(1):73–82, 2006. (Cited on page 24.)

[86] G. Kindlmann. Nearly raw raster data. http://teem.sourceforge.net/nrrd/, 2008. (Cited on page 107.)

[87] G. Kindlmann. Teem 1.10. http://teem.sourceforge.net, 2008. (Cited on page 103.)

[88] G. L. Kindlmann. Superquadric tensor glyphs. In *Proceedings of IEEE TVCG/EG symposium on visualization*, volume 2004, pages 147–154, 2004. (Cited on page 21.)

[89] G. L. Kindlmann and C.-F. Westin. Diffusion tensor visualization with glyph packing. *IEEE transactions on visualization and computer graphics*, 12(5):1329–35, 2006. (Cited on page 21.)

[90] M. A. Koch, D. G. Norris, and M. Hund-Georgiadis. An investigation of functional and anatomical connectivity using magnetic resonance imaging. *NeuroImage*, 16(1):241–250, May 2002. (Cited on pages 23 and 60.)

[91] B. W. Kreher, J. Hennig, and K. A. Il. DTI & FiberTools: a complete toolbox for DTI calculation, fiber tracking, and combined evaluation. In *ISMRM*, volume 265, page 2758, 2006. (Cited on page 105.)

[92] Laboratory of Molecular Neuroimaging Technology. DoDTI - automated analysis of diffusion tensor MRI toolbox. http://neuroimage.yonsei.ac.kr/dodti/. (Cited on page 103.)

[93] J. R. Landis and G. G. Koch. The measurement of observer agreement for categorical data. *Biometrics*, 33(1):pp. 159–174, 1977. (Cited on page 90.)

[94] B. Landman, J. Farrell, and S. Mori. On the coregistration of diffusion weighted images. In *International Society for Magnetic Resonance in Medicine*, pages 684–684, 2006. (Cited on page 105.)

[95] I. N. C. Lawes, T. R. Barrick, V. Murugam, N. Spierings, D. R. Evans, M. Song, and C. Clark. Atlas-based segmentation of white matter tracts of the human brain using diffusion tensor tractography and comparison with classical dissection. *NeuroImage*, 39(1):62–79, Jan. 2008. (Cited on page 66.)

[96] M. Lazar. *White matter tractography: an error analysis and human brain fiber tract reconstruction study*. PhD thesis, University of Utah, 2003. (Cited on pages 23, 25, 56, 60, 63, 64 and 70.)

[97] M. Lazar and A. L. Alexander. White matter tractography using random vector (RAVE) perturbation. 2002. (Cited on pages 23, 56, 60 and 64.)

[98] M. Lazar and A. L. Alexander. An error analysis of white matter tractography methods: synthetic diffusion tensor field simulations. *NeuroImage*, 20(2):1140–53, Oct. 2003. (Cited on pages 64 and 66.)

[99] M. Lazar, D. M. Weinstein, J. S. Tsuruda, K. M. Hasan, K. Arfanakis, M. E. Meyerand, B. Badie, H. a. Rowley, V. Haughton, A. Field, and A. L. Alexander. White matter tractography using diffusion tensor deflection. *Human Brain Mapping*, 18(4):306–321, 2003. (Cited on pages 23, 56, 60, 62, 64, 85, 89 and 92.)

[100] D. Le Bihan. Looking into the functional architecture of the brain with diffusion MRI. *Nature Reviews Neuroscience*, 4(6):469–480, 2003. (Cited on page 6.)

[101] A. Leemans, B. Jeurissen, and J. Sijbers. ExploreDTI: a graphical toolbox for processing, analyzing, and visualizing diffusion MR data. In *17th Scientific Meeting of the International Society for Magnetic Resonance in Medicine*, volume 245, page 3537, 2009. (Cited on page 104.)

[102] H. Li, Z. Xue, L. Guo, T. Liu, J. Hunter, and S. T. C. Wong. A hybrid approach to automatic clustering of white matter fibers. *NeuroImage*, 49(2):1249–58, Jan. 2010. (Cited on pages 25 and 83.)

[103] M. Maddah, W. E. L. Grimson, S. K. Warfield, and W. M. Wells. A unified framework for clustering and quantitative analysis of white matter fiber tracts. *Medical Image Analysis*, 12(2):191–202, 2008. (Cited on pages 26 and 104.)

[104] M. Maddah, A. Mewes, S. Haker, W. E. L. Grimson, and S. Warfield. Automated atlas-based clustering of white matter fiber tracts from DTMRI. In *International Conference on Medical Image Computing and Computer Assisted Intervention, (MICCAI'05)*, Lecture Notes in Computer Science, page 188, 2005. (Cited on page 82.)

[105] M. Mart. Regularization of diffusion tensor maps using a non-gaussian markov random field approach. *Tensor*, pages 92–100, 2003. (Cited on page 25.)

[106] J. Martino, P. C. De Witt Hamer, F. Vergani, C. Brogna, E. M. de Lucas, A. Vázquez-Barquero, J. a. García-Porrero, and H. Duffau. Cortex-sparing fiber dissection: an improved method for the study of white matter anatomy in the human brain. *Journal of anatomy*, (June), July 2011. (Cited on pages 6 and 66.)

[107] J. Martín-Fernández, M. Bren, C. Barceló-Vidal, and V. Pawlowsky-Glahn. A measure of difference for compositional data based on measures of divergence. In *Fifth Annual Conference of the International Association for Mathematical Geology*, Ed. S.J. Lippard et al. Trondheim (Norway), Vol. 1, pages 211–215, 1999. (Cited on pages 36 and 41.)

[108] Y. Masutani. Diffusion tensor visualizer. http://www.ut-radiology.umin.jp/people/masutani/dTV/dTVdownload-e.htm. (Cited on page 103.)

[109] Y. Masutani, S. Aoki, O. Abe, and K. Ohtomo. Model-based tractography based on statistical atlas of MR-DTI. *3rd IEEE International Symposium on Biomedical Imaging: Macro to Nano, 2006.*, pages 89–92, 2006. (Cited on pages 25 and 82.)

[110] T. McGraw, B. C. Vemuri, Y. Chen, M. Rao, and T. H. Mareci. DT-MRI denoising and neuronal fiber tracking. *Medical image analysis*, 8(2):95–111, June 2004. (Cited on pages 23, 58, 64 and 70.)

[111] A. Mebarki, P. Alliez, and O. Devillers. Farthest point seeding for efficient placement of streamlines. In *IEEE Conf. Visualization*, pages 479–486, 2005. (Cited on page 83.)

[112] B. Moberts. Hierarchical visualization using fiber clustering, June 2005. Master's Thesis - Eindhoven. (Cited on page 26.)

[113] B. Moberts, A. Vilanova, and J. J. van Wijk. Evaluation of fiber clustering methods for diffusion tensor imaging. In *VIS 05. IEEE Visualization, 2005.*, pages 65–72. IEEE, 2005. ISBN 0-7803-9462-3. (Cited on page 25.)

[114] S. Mohammadi, V. Glauche, and M. Deppe. SPM normalization toolbox for voxel-based statistics on fractional anisotropy images. *NeuroImage*, 47 (Supplement 1):S122, S122, 2009. (Cited on page 105.)

[115] G. Morgan and H. Zhang. DTI ToolKit (DTI-TK). http://software.incf.org/software/dti-toolkit-dti-tk, 2011. (Cited on page 104.)

[116] S. Mori, B. Crain, V. Chacko, and P. C. M. van Zijl. Three dimensional tracking of axonal projections in the brain by magnetic resonance imaging. *Ann Neurol*, 45:265–269, 1999. (Cited on pages 59 and 64.)

[117] S. Mori, S. Wakana, L. M. Nagae-Poetscher, and P. C. M. V. Zijl. MRI atlas of human white matter. *Elseiver*, 2004. (Cited on pages 24, 26, 88, 89 and 93.)

[118] S. Mori and P. C. M. V. Zijl. Fiber tracking: principles and strategies - a technical review. *NMR in Biomedicine*, 15(7-8):468–480, 2002. (Cited on pages 22, 23, 26, 59, 83 and 86.)

[119] S. Nedjati-Gilani, D. C. Alexander, and G. J. M. Parker. Regularized super-resolution for diffusion MRI. In *Biomedical Imaging: From Nano to Macro, 2008. ISBI 2008. 5th IEEE International Symposium on*, volume 1, pages 875–878. IEEE, 2008. (Cited on page 25.)

[120] J. Nielsen. A modular framework for development and interlaboratory sharing and validation diffusion tensor tractography algorithms. *Journal of Digital Imaging*, 19(2):112–117, 2006. (Cited on page 103.)

[121] P. G. P. Nucifora, R. Verma, S.-k. Lee, and E. R. Melhem. Diffusion-tensor MR imaging and tractography: Exploring brain microstructure and connectivity. *Radiology*, 245(2):367–384, 2007. (Cited on pages 24 and 83.)

[122] L. J. O'Donnell. *Cerebral white matter analysis using diffusion imaging*. PhD thesis, MIT, 2006. (Cited on pages 25 and 82.)

[123] L. J. O'Donnell and C.-F. Westin. Automatic tractography segmentation using a highdimensional white matter atlas. *IEEE Trans. Medical Imaging*, 11(26): 1562–1575, 2007. (Cited on pages 3, 25 and 82.)

[124] L. J. O'Donnell, C.-F. Westin, and A. J. Golby. Tract-based morphometry for white matter group analysis. *Neuroimage*, 3(45):832–844, 2009. (Cited on page 82.)

[125] N. L. of Medicine NLM. ITK-Insight Toolkit, http://www.itk.org. (Cited on page 103.)

[126] E. Özarslan and T. H. Mareci. Generalized diffusion tensor imaging and analytical relationships between diffusion tensor imaging and high angular resolution imaging. *Magnetic Resonance in Medicine*, 50(5):955–965, 2003. (Cited on pages 15 and 16.)

[127] E. Özarslan, T. M. Shepherd, B. C. Vemuri, S. J. Blackband, and T. H. Mareci. Resolution of complex tissue microarchitecture using the diffusion orientation transform (DOT). *NeuroImage*, 31(3):1086–103, July 2006. (Cited on pages 15 and 16.)

[128] J. Palarea-Albaladejo, J. Martín-Fernández, and J. Soto-Espinosa. Magnetic resonance imaging shows orientation and asymmetry of white matter fiber tracts. *Brain Research*, 780:27–33, 1998. (Cited on page 36.)

[129] G. J. M. Parker and D. C. Alexander. Probabilistic Monte Carlo based mapping of cerebral connections utilizing whole-brain crossing fibre information. *Information processing in medical imaging*, 18:684–95, July 2003. (Cited on pages 13, 16, 23 and 60.)

[130] G. J. M. Parker, H. a. Haroon, D. M. Morris, M. Lambon-Ralph, and K. Embleton. Integration of fMRI and probabilistic tractography for cerebral network analysis. In *Biomedical Imaging: Nano to Macro, 2006. 3rd IEEE International Symposium on*, pages 359–362. IEEE, 2006. (Cited on page 67.)

[131] S. C. Partridge, P. Mukherjee, R. G. Henry, S. P. Miller, J. I. Berman, H. Jin, Y. Lu, O. a. Glenn, D. M. Ferriero, a. J. Barkovich, and D. B. Vigneron. Diffusion tensor imaging: serial quantification of white matter tract maturity in premature newborns. *NeuroImage*, 22(3):1302–14, July 2004. (Cited on pages 24 and 83.)

[132] V. Patel, I. D. Dinov, J. D. Van Horn, P. M. Thompson, and A. W. Toga. LONI MiND: metadata in NIfTI for DWI. *NeuroImage*, 51(2):665–76, June 2010. (Cited on page 107.)

[133] M. Perrin, C. Poupon, B. Rieul, P. Leroux, A. Constantinesco, J.-F. Mangin, and D. Lebihan. Validation of q-ball imaging with a diffusion fibre-crossing phantom on a clinical scanner. *Philosophical transactions of the Royal Society of London. Series B, Biological sciences*, 360(1457):881–91, May 2005. (Cited on page 66.)

[134] C. Pierpaoli and P. J. Basser. Toward a quantitative assessment of diffusion. *Magnetic Resonance in Medicine*, 36(6):893–906, 1996. (Cited on pages 25 and 37.)

[135] C. Poupon, B. Rieul, I. Kezele, M. Perrin, F. Poupon, and J. F. Mangin. New Diffusion phantoms dedicated to the study and validation of HARDI models. *Magnetic Resonance in Medicine*, 60(6):1276–1283, 2008. (Cited on page 66.)

[136] F. Prados, I. Boada, A. Prats-Galino, J. A. Martín-Fernández, M. Feixas, G. Blasco, J. Puig, and S. Pedraza. Analysis of new diffusion tensor imaging anisotropy measures in the three-phase plot. *Journal of Magnetic Resonance Imaging*, 31 (6):1435–1444, 2010. (Cited on page 86.)

[137] W. H. Press, S. A. Teukolsky, W. T. Vetterling, and B. P. Flannery. *Numerical recipes in C*. Cambridge University Press, 1992. 994 pp. (Cited on page 58.)

[138] S. M. Prigarin and K. Hahn. Stochastic algorithms for white matter fiber tracking and the inference of brain connectivity from MR diffusion tensor data, December 2004. Personal Communication - Statistical Analysis of Discrete Structures (SFB386). (Cited on pages 23, 56, 60, 62 and 64.)

[139] G. Rainer. BrainVoyager QX. http://www.brainvoyager.com, 2011. (Cited on page 105.)

[140] P. Rakic. Experimental manipulation of cerebral cortical areas in primates. *Philosophical Transactions of the Royal Society of London - Series B: Biological Sciences*, 331(1261):291–294, 1991. (Cited on page 6.)

[141] C. R. Rao. Diversity and dissimilarity coefficients: a unified approach. *Theoretical Population Biology*, 21:24–43, 1982. (Cited on page 41.)

[142] W. Rasband. ImageJ introduction. (Cited on page 103.)

[143] M. Reisert, I. Mader, and V. Kiselev. Tracking a physical phantom by global fibre reconstruction. In *Workshop Diffusion Modelling and Fiber Cup at MICCAI*, pages 1–4. Citeseer, 2009. (Cited on page 23.)

[144] J. Rigau, M. Feixas, and M. Sbert. An information theoretic framework for image segmentation. In *IEEE International Conference on Image Processing*, pages 1193–1196, 2004. (Cited on pages 84 and 86.)

[145] P. Scifo, F. Dell'Acqua, G. Rizzo, M. Gilardi, and F. F. A dedicated phantom for diffusion tensor imaging studies. In *ISMRM*, 2004. (Cited on page 66.)

[146] C. E. Shannon. A mathematical theory of communication. *The Bell System Technical Journal*, 27:379–423, 623–656, July, October 1948. (Cited on pages 2, 26 and 28.)

[147] J. S. Shimony, A. Z. Snyder, N. Lori, and T. E. Conturo. Automated fuzzy clustering of neuronal pathways in diffusion tensor tracking. In *Conf. Proc. Soc. Mag. Reson. Med.*, May 2002. (Cited on pages 24 and 26.)

[148] H. Shinohara, S. Yasutaka, Y. Taniguchi, R. Kominami, and S. Kawamata. Fiber dissection technique for demonstrating the lateral lemniscus of the human brain. *Okajimas folia anatomica Japonica*, 80(5-6):115–8, Mar. 2004. (Cited on page 6.)

[149] D. Shreiner, M. Woo, J. Neider, and T. Davis. *OpenGL Programming Guide: The Official Guide to Learning OpenGL*. Reading, MA: Addison-Wesley, 1999. (Cited on page 102.)

[150] N. Slonim and N. Tishby. Agglomerative information bottleneck. In *Proceedings of NIPS-12 (Neural Information Processing Systems)*, pages 617–623. MIT Press, 2000. (Cited on page 32.)

[151] N. Slonim and N. Tishby. Document clustering using word clusters via the information bottleneck method. In *Proceedings of the 23rd Annual International ACM SIGIR Conference on Research and Development in Information Retrieval*, pages 208–215. ACM Press, 2000. Held in Athens, Greece. (Cited on page 31.)

[152] P. Staempfli, C. Reischauer, T. Jaermann, a. Valavanis, S. Kollias, and P. Boesiger. Combining fMRI and DTI: a framework for exploring the limits of fMRI-guided

DTI fiber tracking and for verifying DTI-based fiber tractography results. *NeuroImage*, 39(1):119–26, Jan. 2008. (Cited on page 67.)

[153] E. O. Stejskal and J. E. Tanner. Spin diffusion measurements: spin echoes in the presence of a time-dependent field gradient. *The Journal of Chemical Physics*, 42(1):288–292, 1965. (Cited on page 7.)

[154] Y. T, Weldeselassie, G. Hamarneh, and D. Weiskopf. Tensor dissimilarity based adaptive seeding algorithm for DT-MRI visualization with streamtubes. In *Proc. of SPIE*, 2007. (Cited on page 83.)

[155] Template Graphics Software Inc. Amira 3.1, 2002. Mercury Computer Systems. (Cited on pages 46 and 88.)

[156] N. Tishby, F. C. Pereira, and W. Bialek. The information bottleneck method. In *Proceedings of the 37th Annual Allerton Conference on Communication, Control and Computing*, pages 368–377, 1999. (Cited on page 32.)

[157] J.-D. Tournier, F. Calamante, D. G. Gadian, and A. Connelly. Direct estimation of the fiber orientation density function from diffusion-weighted MRI data using spherical deconvolution. *NeuroImage*, 23(3):1176–85, Nov. 2004. (Cited on pages 15 and 16.)

[158] D. S. Tuch. Q-ball imaging. *Magnetic resonance in medicine*, 52(6):1358–72, Dec. 2004. (Cited on pages 14 and 16.)

[159] D. S. Tuch, T. G. Reese, M. R. Wiegell, N. Makris, J. W. Belliveau, and V. J. Wedeen. High angular resolution diffusion imaging reveals intravoxel white matter fiber heterogeneity. *Magnetic Resonance in Medicine*, 48(4):577–582, 2002. (Cited on pages 13, 16, 23, 26 and 56.)

[160] U. Türe, M. G. Yasargil, a. H. Friedman, and O. Al-Mefty. Fiber dissection technique: lateral aspect of the brain. *Neurosurgery*, 47(2):417–26, Aug. 2000. (Cited on page 6.)

[161] G. Turk and D. Banks. Image-guided streamline placement. In *Computer Graphics and Interactive Techniques (SIGGRAPH '96)*, pages 453–460, 1996. (Cited on page 83.)

[162] A. M. Ulug and P. C. van Zijl. Orientation-independent diffusion imaging without tensor diagonalization: Anisotropy definitions based on physical attributes of the diffusion ellipsoid. *Magnetic Resonance Imaging*, 9(6):804–813, 1999. (Cited on page 37.)

[163] A. Vilanova, G. Berenschot, and C. Van Pul. DTI visualization with streamsurfaces and evenly-spaced volume seeding. In *VisSym'04 Joint EG–IEEE TCVG Symposium on Visualization, Conf. Proc*, pages 173–182, 2004. (Cited on page 60.)

[164] A. Vilanova, S. Zhang, G. L. Kindlmann, and D. H. Laidlaw. *An Introduction to Visualization of Diffusion Tensor Imaging and Its Applications*, pages 121–153. Springer, 2006. (Cited on pages 17 and 83.)

[165] S. Wakana, H. Jiang, L. M. Nagae-Poetscher, P. C. M. V. Zijl, and S. Mori. Fiber tract-based atlas of human white matter anatomy. *Radiology*, 1(230):77–87, 2004. (Cited on pages 26, 72, 89 and 111.)

[166] R. Wang, T. Benner, A. G. Sorensen, and V. J. Wedeen. Diffusion toolkit: A software package for diffusion imaging data processing and tractography. In *Intl Soc Mag Reson Med 15*, page 3720. International Society for Magnetic Resonance in Medicine, 2007. (Cited on page 104.)

[167] D. F. Watson and G. Philip. Measures of variability for geological data. *Mathematical Geology*, 21(2):233–254, 1989. (Cited on page 41.)

[168] V. J. Wedeen, P. Hagmann, W.-Y. I. Tseng, T. G. Reese, and R. M. Weisskoff. Mapping complex tissue architecture with diffusion spectrum magnetic resonance imaging. *Magnetic Resonance in Medicine*, 54(6):1377–1386, 2005. (Cited on pages 14 and 16.)

[169] V. J. Wedeen, T. G. Reese, D. S. Tuch, M. R. Weigel, J. Dou, R. M. Weiskoff, and D. Chessler. Mapping fiber orientation spectra in cerebral white matter with Fourier-transform diffusion MRI. In *International Society in Magnetic Resonance in Medicine*, volume 8, page 82, 2000. (Cited on pages 14, 16 and 23.)

[170] D. M. Weinstein, G. L. Kindlmann, and E. Lundberg. Tensorlines: advection-diffusion based propagation through diffusion tensor fields. In *Visualization '99*, pages 249–530, 1999. (Cited on pages 23, 26, 59, 60 and 64.)

[171] C.-F. Westin. *A tensor framework for multidimensional signal processing*. PhD thesis, Linköping University, Sweden, S-581 83 Linköping, Sweden, 1994. Dissertation No 348, ISBN 91-7871-421-4. (Cited on page 37.)

[172] C.-F. Westin, S. E. Maier, B. Khidhir, P. Everett, F. A. Jolesz, and R. Kikinis. Image processing for diffusion tensor magnetic resonance imaging. In *International Conference on Medical Image Computing and Computer Assisted Intervention, (MICCAI'99)*, Lecture Notes in Computer Science, pages 441–452, September 19–22 1999. (Cited on page 60.)

[173] C.-F. Westin, S. E. Maier, H. Mamata, A. Nabavi, F. A. Jolesz, and R. Kikinis. Processing and visualization of diffusion tensor MRI. *Medical Image Analysis*, 6 (2):93–108, 2002. (Cited on pages 18, 38, 56 and 100.)

[174] C.-F. Westin, S. Peled, H. Gudbjartsson, R. Kikinis, and F. A. Jolesz. Geometrical diffusion measures for MRI from tensor basis analysis. In *ISMRM '97*, page 1742, Vancouver Canada, April 1997. (Cited on pages 18, 36 and 37.)

[175] P. Whelan, R. J. T. Sadleir, and O. Ghita. NeatVision: visual programming for computer-aided diagnostic applications. *Radiographics*, 24(1779Y1789), 2004. (Cited on page 103.)

[176] M. W. Woolrich, S. Jbabdi, B. Patenaude, M. Chappell, S. Makni, T. Behrens, C. Beckmann, M. Jenkinson, and S. M. Smith. Bayesian analysis of neuroimaging data in FSL. *NeuroImage*, 45(1 Suppl):S173–S186, 2009. (Cited on page 104.)

[177] X. Wu, Q. Xu, L. Xu, J. Zhou, A. W. Anderson, and Z. Ding. Genetic white matter fiber tractography with global optimization. *Journal of neuroscience methods*, 184(2):375–9, Nov. 2009. (Cited on page 23.)

[178] Y. Xia, U. Turken, S. L. Whitfield-Gabrieli, and J. D. Gabrieli. Knowledge-based classification of neuronal fibers in entire brain. In *International Conference on Medical Image Computing and Computer Assisted Intervention, (MICCAI'05)*, pages 205–212, 2005. (Cited on page 82.)

[179] D. Xu, S. Mori, M. Solaiyappan, P. C. M. van Zijl, and C. Davatzikos. A framework for callosal fiber distribution analysis. *NeuroImage*, 17:1131–1143, 2002. (Cited on page 89.)

[180] X. Ye, D. Kao, and A. Pang. Strategy for seeding three-dimensional streamlines. In *IEEE Visualization 2005*, pages 471–478, 2005. (Cited on page 83.)

[181] F.-C. Yeh. DSI Studio. http://dsi-studio.labsolver.org/, 2011. (Cited on page 103.)

[182] R. W. Yeung. *A First Course in Information Theory*. Springer, 2002. ISBN 0306467917. (Cited on page 26.)

[183] N. Yi-Ren, S. Shiffman, T. Brosnan, J.M.Links, L. Beach, N. Judge, , Y. Xu, U. Kelkar, and A. Reiss. BrainImageJ: A Java-based framework for interoperability in neuroscience, with specific applications to neuroimaging. *Journal of the American Medical Informatics Association*, 8:431–441, September 2000. (Cited on page 103.)

[184] S. Zhang, c. Demiralp, and D. H. Laidlaw. Visualizing diffusion tensor MR images using streamtubes and streamsurfaces. *IEEE Transactions on Visualization and Computer Graphics*, 4(9):454–462, 2003. (Cited on pages 23, 60 and 83.)

[185] S. Zhang and D. H. Laidlaw. Hierarchical clustering of streamtubes. Technical Report CS-02-18, Brown University Computer Science Department, August 2002. (Cited on pages 24, 26 and 82.)

[186] S. Zhang and D. H. Laidlaw. DTI fiber clustering in the whole brain. In *IEEE Visualization 2004 Poster Compendium*, 2004. (Cited on pages 24 and 26.)

[187] S. Zhang and D. H. Laidlaw. DTI fiber clustering and cross-subject cluster analysis. In *Proceedings of ISMRM*, 2005. (Cited on pages 24 and 26.)

[188] W. Zhang, A. Olivi, S. J. Hertig, P. van Zijl, and S. Mori. Automated fiber tracking of human brain white matter using diffusion tensor imaging. *NeuroImage*, 42 (2):771–777, Aug. 2008. (Cited on pages 25 and 83.)

[189] Y. Zhang, J. Zhang, K. Oishi, A. V. Faria, H. Jiang, X. Li, K. Akhter, P. Rosa-Neto, G. B. Pike, A. Evans, A. W. Toga, R. Woods, J. C. Mazziotta, M. I. Miller, P. C. M. van Zijl, and S. Mori. Atlas-guided tract reconstruction for automated and comprehensive examination of the white matter anatomy. *NeuroImage*, 52 (4):1289–1301, May 2010. (Cited on pages 25, 26 and 83.)

[190] T. Zhu, X. Liu, M. D. Gaugh, P. R. Connelly, H. Ni, S. Ekholm, G. Schifitto, and J. Zhong. Evaluation of measurement uncertainties in human diffusion tensor imaging (DTI)-derived parameters and optimization of clinical DTI protocols with a wild bootstrap analysis. *Journal of magnetic resonance imaging: JMRI*, 29 (2):422–35, Feb. 2009. (Cited on page 25.)